Fall 2023

Evaluation of the Dynamic Response of Gravelly Soil Under Different Drainage Conditions

Pressley Margaret Perry

EVALUATION OF THE DYNAMIC RESPONSE OF GRAVELLY SOIL UNDER DIFFERENT DRAINAGE CONDITIONS

by

Pressley M. Perry

Bachelor of Science
University of South Carolina, 2022

Submitted in Partial Fulfillment of the Requirements

For the Degree of Master of Science in

Civil Engineering

College of Engineering and Computing

University of South Carolina

2023

Accepted by:

Inthuorn Sasanakul, Director of Thesis

Charles Pierce, Reader

Sarah Gassman, Reader

Ann Vail, Dean of the Graduate School

ACKNOWLEDGEMENTS

I am incredibly grateful to the Lord for providing me with the opportunity to pursue further education and grow both academically and personally. I cannot begin to express my thanks to all the educators I have had the privilege to learn from at the University of South Carolina. I am deeply appreciative of all the time they have dedicated to teaching and challenging me academically.

I could not have completed this thesis without the mentorship and help of my fellow students and advisor, Dr. Sasanakul. Firstly, I express my deepest gratitude to Dr. Sasanakul for the countless time she spent teaching and helping me prepare this document. Thank you for the invaluable constructive feedback and for constantly pushing me to produce the best work I am capable of. I want to express much appreciation to Pitak Ruttithivaphanich for the countless hours and patience spent training me in the triaxial and centrifuge equipment as well as data analysis. I also could not have completed the tests without the help of undergraduate student Valerie Sims, who consistently worked hard assisting in the lab. Many thanks to Siwadol Dejphumee and Nampol Chaowalittrakul for their constant encouragement and assistance.

Lastly, I want to express much gratitude to my friends and family who have encouraged me throughout this process. I am blessed to have parents who taught me the importance of working hard to complete something to the best of your ability.

ABSTRACT

Throughout history in the field of geotechnical earthquake engineering, there have been numerous experimental investigations on the dynamic behavior of soils. Many of these efforts have been focused on sand and silty sand material due to their susceptibility to liquefaction phenomena. However, gravelly soil material (i.e., soil in which gradation contains primarily gravel and sand) has exhibited this phenomenon in response to earthquake loading in many case histories. Therefore, it is important to extend the experimental assessment of gravelly soil material to develop a better understanding of the cyclic response and to support the development of numerical models. This study evaluates the impact of drainage conditions on the dynamic response of gravelly soils through a series of undrained and drained load-controlled cyclic triaxial element tests and centrifuge physical modeling tests. The material was saturated mine waste rock classified as gravelly soil composed of gravel, sand, and fines and was tested in loose to very dense conditions. Undrained and drained triaxial element tests aimed to evaluate liquefaction characteristics and develop an empirical model for excess pore water pressure and cyclic-induced volumetric strain. The effect of sample size of cyclic triaxial drained test was investigated for 6- and 4-inch diameter samples. The results of volumetric strain between the two sample sizes were observed to agree well. This provides an opportunity to further research on gravelly soils without the requirement of large-scale triaxial devices. Axial strain was used to correlate pore water pressure and volumetric strain from the undrained and drained triaxial tests, respectively. The correlated relationship suggests that to obtain

the same amount of volumetric strain, there must be greater pore pressure generation in dense soil. This correlation developed by ideal drainage conditions in element tests was compared to the partial drainage condition in centrifuge models. Two centrifuge models in dense and loose condition aimed to simulate an approximately 6 m soil profile with a vertical effective stress of 140 kPa located at the middle of the model. Settlement measurements were analyzed in the upper and lower half of the soil model. Greater settlement was observed in the upper half of both models. In contrast, maximum excess pore pressure manifested in the lower half of the models. Shear modulus and damping were reported for both density conditions. In general, both models had a reduction in shear modulus in the initial loading cycles followed by an increasing trend for the remainder of shaking. At the end of shaking, the loose model ultimately gained stiffness. Damping decreased with increasing loading cycle for both density conditions. The impacts of different drainage conditions for the two laboratory methods were discussed. Triaxial tests resulted in conservative values of excess pore water pressure due to the undrained condition. Partial drainage in centrifuge models resulted in larger volumetric strains at lower values of R_u in comparison to triaxial element tests. Findings from this study indicate that greater volumetric strain or settlement can be expected at lower R_u under field conditions than predicted by triaxial testing.

TABLE OF CONTENTS

LIST OF TABLES

LIST OF FIGURES

LIST OF SYMBOLS

D_R	Relative density
C_u	Coefficient of uniformity
C_c	Coefficient of curvature
D_{50}	Particle size diameter at 50% of material
G_s	Specific gravity
N	Number of cycle
N_L	Number of cycle at liquefaction
R_u	Pore water pressure ratio
$\Delta\varepsilon_c$	Change in cyclic axial strain
ε_c	Cyclic axial strain
$\boldsymbol{\varepsilon}_{com}$	Compressive axial strain
$\boldsymbol{\varepsilon}_{ext}$	Extensive axial strain
ε_V	Volumetric strain

LIST OF ABBREVIATIONS

ASTM ..... American Society for Testing and Materials

CRR..... Cyclic Resistance Ratio

CSR.....Cyclic Stress Ratio

CHAPTER 1

INTRODUCTION

1.1 Background and Motivation

Dynamic behaviors of soil have been widely studied in the field of soil dynamics and geotechnical earthquake engineering to provide understanding of soil response to dynamic events such as earthquakes and vibration. In history, much of this research has been dedicated to sands and sandy soils due to their susceptibility to the phenomena known as soil liquefaction. Soil liquefaction typically results in a loss of strength and stiffness leading to the collapse of soil structure. Gravelly soils are less susceptible to liquefaction in comparison to sandy soils, however, liquefaction has been observed in these soils in many case histories (Cao et al. 2011, 2013). Salvatore et al. (2022) reports that from 1891 to 2020, there have been 27 historical cases totaling 109 sites of gravel liquefaction due to earthquakes. Recent observations of gravel liquefaction were found in both the 2017 Pohang Earthquake and the 2020 Petrinja, Croatia earthquakes (Baize et al., 2022; Naik et al., 2019). In general, the dynamic behaviors of gravelly soils are not as well understood and well quantified in literature. The term “gravelly soil” has a wide range of grain size distribution for both natural and manmade deposits. Gravelly soil is used in the construction of geo-structures including dams, railroad embankment, foundations, and many others. In addition, gravelly soils are found in a product of mining operations namely waste rock. The material is classified as gravelly soil when the

gradation is reduced to contain mostly gravel and sand. Waste rock is stored in piles and may be reused as inclusions to improve the stability and drainage of the tailings and mine waste facilities. Recent failure of tailings impoundments has triggered more effort to investigate liquefaction susceptibility of waste rocks and tailings (e.g., Ferdosi et al. 2015; James et al., 2017; Kaseng et al.; Kossoff et al., 2014; Pepin et al. 2012; Ruttithivapanich et al., 2022).

Within the past approximately 30 years, the topic of gravel and gravelly soils has increasingly become of interest in the field of geotechnical engineering (Evans & Zhou, 1995; Evans & Rollins, 1999). However, this has been met with challenges due to sampling difficulties, requirement of large-scale equipment, membrane compliance, and more (Evans & Rollins, 1999). Considering the lack of laboratory testing for gravelly soils, limited studies on cyclic behaviors of gravelly soils are available. There is great significance in developing a correlation between pore-water pressure and volumetric strain due to cyclic loading, particularly in support of numerical modeling validation. To establish this correlation, extensive cyclic load testing must be done for both drained and undrained conditions. Therefore, the aim of this study was to investigate the cyclic behaviors of gravelly soil under different drainage conditions through advanced laboratory and centrifuge model testing. The objective is threefold; (i) to investigate cyclic response and behaviors under fully undrained, fully drained, and field condition simulated by a centrifuge model, (ii) to assess impact of initial relative densities on cyclic behavior and liquefaction potential, and (iii) to generate empirical models for pore water pressure generation and cyclic-induced volume change for the material.

A series of cyclic triaxial tests were conducted under fully undrained and fully drained conditions. In the undrained condition, a liquefaction assessment is performed to evaluate cyclic stress ratio and the evolution of pore water pressure with number of cycles. In the drained condition, an increase in volumetric strain is evaluated with number of cycles for the same cyclic stress ratio as in the undrained condition. Using an axial strain-based approach, the data compiled from both types of tests are used to estimate a relationship between pore water pressure ratio and volumetric strain. The results from cyclic triaxial tests are then compared to the cyclic response observed in centrifuge model tests where the drainage resembles a field condition. Compared to the cyclic triaxial test, the centrifuge modeling test provides more realistic field stress, loading, and drainage conditions. In addition, a centrifuge model simulates a large-scale soil column instead of a soil element. In this study, two centrifuge tests were performed on gravelly soil models with two different relative densities. During shaking, the development of excess pore water pressure and a corresponding volumetric strain is investigated. Shear modulus and damping are evaluated with effects on confinement, shaking amplitude, and relative density.

This research contributes data for the design of mine waste facilities. Experimental results generated in this study are considered useful for numerical modeling studies.

1.2 Literature Review

Cyclic induced liquefaction in sands and silts has been extensively studied in laboratories. These include cyclic tests to evaluate cyclic strength and stiffness, development of excess pore-water pressure, and its dependency on volumetric strain.

Numerous empirical relationships have been developed to describe the relationships between the excess pore water pressure and number of cycle (e.g., Banzibaganye et al., 2022; Chen et al., 2019; Polito et al., 2008). Volume change or settlement is of interest in sands during both the drained condition and post liquefaction. In sandy soils, Wichtmann et al. (2005) performed extensive drained triaxial compression tests with thousands of cycles to develop a more useful and accurate prediction of the accumulation of strain due to cyclic loading. Due to pore water dissipation, prediction of the expected volumetric strain in sands post liquefaction has long been explored in geotechnical engineering (Stamatopoulos et al., 2004; Tokimatsu & Seed, 1987; Ishihara & Yoshimine, 1992). Stamatopoulos et al. (2004) assessed volume change after liquefaction occurred in saturated sand samples performed in constant volume cyclic direct shear device. Recently, Chen et al (2019) developed a relationship between the excess pore water pressure and volumetric stains applicable for various sands based on strain-controlled cyclic triaxial tests. They developed a semi-empirical relationship to predict the excess pore water pressure ratio from the volumetric strain. Banzibaganye et al. (2022) developed a similar relationship for saturated sand rubber chips mixtures.

Recently, efforts have been made to increase research on drained and undrained cyclic testing on gravelly soils (e.g., Flora et al., 2012; Guoxing et al., 2021; Hubler et al., 2023; Xu et al., 2019). Flora et al. (2012) performed large undrained cyclic triaxial tests on undisturbed samples of gravelly soil to assess the ability of the state parameter to analyze liquefaction susceptibility. They found that the resistance to soil liquefaction increased with the state parameter and that anisotropic consolidated triaxial tests may produce non-conservative results. Guoxing et al. (2021) conducted undrained cyclic

triaxial tests on sand-gravel mixtures and rather proposed a sand-gravel skeleton void ratio to assess liquefaction susceptibility. Xu et al. (2019) conducted large scale cyclic simple shear tests on sand gravel mixtures to develop a relationship between the normalized damping ratio and the normalized secant shear modulus. They found that the cyclic response of sand gravel mixtures can be categorized as sand like, transitional, and gravel like based upon the percentage of gravel composition. Additionally, an increase in the gravel content resulted in greater negative shear strain. Most recently, Hubler et al. (2023) conducted cyclic simple shear test to investigate pore pressure response of gravel and gravel-sand mixtures. It was found that the coefficient of uniformity, C_u, has a major impact on the pore pressure generation of gravelly soils. While undrained cyclic triaxial test results provide good understanding of pore pressure development, it is important to evaluate volume change behavior when gravelly soils experience high excess pore water pressure. In addition to soil element tests, centrifuge modeling tests have been performed on very loose gravelly soils composed of gravel, sand, and fines to investigate soil liquefaction behaviors (e.g., Ruttithivapanich & Sasanakul, 2022, 2023). Due to the nature of cyclic loading, dynamic centrifuge tests are considered undrained loading condition, however the model is allowed to freely drain at the surface during shaking. Ruttithivapanich & Sasanakul (2023) findings include dilative behaviors of gravelly soils under dynamic loading, observation of fines migration to the surface of the centrifuge model, and settlement (volumetric strains) observed for different compositions.

1.3 Organization of Document

This chapter includes an introduction to the topic and an overview of relevant literature. Chapters 2 and 3 present the study of cyclic triaxial element testing and centrifuge model testing, respectively. Each chapter contains an introduction, test methodology, data results and analysis. Chapter 3 also includes discussion on the comparison of results for the cyclic triaxial tests and centrifuge modelling tests. Chapter 4 follows with conclusions on the findings of each laboratory method, a summary of comparisons, and recommendations for future research.

CHAPTER 2

CYCLIC TRIAXIAL ELEMENT TESTS

2.1 Introduction

This chapter focuses on the cyclic triaxial element tests performed on gravelly soils and presents the material properties of the soil used in this study for both element and model tests. Section 2.2 begins with material properties and the procedure of sample preparation. Section 2.3 follows with an outline of the testing program and method of both undrained and drained triaxial tests. General cyclic triaxial results and analysis are presented in Section 2.4. This includes post consolidation information and the undrained and drained cyclic response. The undrained cyclic response includes discussion on liquefaction definition, assesses pore pressure generation, and presents the relationship of cyclic resistance ratio and number of cycles to reach liquefaction. The drained cyclic response presents the results of volumetric strain for different cyclic stress ratios. Section 2.5 contains correlations of axial strain with subsequent pore water pressure and volumetric strain. The extraction of data and methodology to create these correlations is described. Additionally, a relationship of pore water pressure and volumetric strain is presented for the data produced in this study and compared to previous correlations in literature. Lastly, post-test observations and photos are found in Section 2.6.

2.2 Material Properties and Methodology

The material in this study is classified as GW-GC, well-graded gravel with sand and low plasticity clay. The various index properties are shown in Table 2.1. The maximum and minimum void ratio were determined in accordance with ASTM D4253-16el and assumed specific gravity (G_s) of 2.7 based on previous research with similar material (Ruttithivaphanich, 2022). The grain size distribution is shown in Figure 2.1. In this study, the maximum particle size is approximately 19-25.4 mm (~ 0.75-1 inch). Particles of this size correspond to about 6.4% by weight of the samples. It is noted that some of these particles are oblong and can be 25.4 mm long in one orientation and much smaller (10 mm or less) in another orientation. A photograph showing the soil particles is in Figure 2.2, the material is grey in color and the gravel and sand particles are angular.

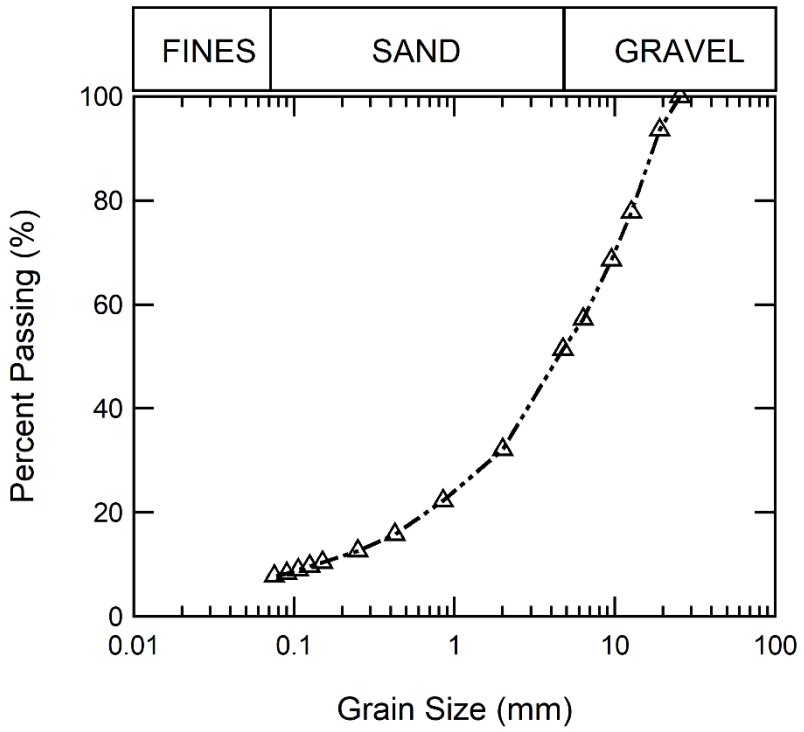

Figure 2.1 Grain size distribution of gravelly soil material.

Figure 2.2 Visual display of material.

Table 2.1 Index properties

Property	Value
Max Void Ratio*	0.42
Min Void Ratio*	0.18
Relative Density of Dense Samples, (%)**	94.2
Relative Density of Medium Dense Samples, (%)**	30.6
Water content, (%)**	5
C_u	46.7
C_c	2.9
D_{50} (mm)	4.5
% Gravel (by weight) > No. 4 Sieve (maximum particle size ~ 0.75”-1”)	49%
% Coarse Sand (by weight) > No. 40 Sieve	35%
% Fine Sand (by weight) < No. 40 Sieve	8%
% Fines (by weight) < No. 200 Sieve	8%

*Void ratios calculated by assumed G_s of 2.7
**Initial value used to prepare sample

The method of sample preparation follows the procedure in accordance with ASTM D5311. Each specimen was constructed with 5 layers. Each of the layers were prepared with the same percentages of gravel, sand, fines, and water as detailed in Table 2.1. The procedure for setting up a sample for the cyclic triaxial device is presented as follows.

Each material for the 5 layers was thoroughly mixed prior to the sample preparation. To begin setting up the cyclic triaxial machine, water was flushed through the base to ensure no soil was caught within the machine. Vacuum grease was used to surround the base, top cap, and soil membrane. A porous stone with filter paper was placed on the base. A membrane was then placed around the base and surrounded with the mold used for construction of the soil specimen. The bottom of the soil specimen to the top was measured to obtain details for soil layer heights to ensure the same density was maintained throughout the specimen. This is an extremely important step in the ASTM standard due to the influence density has on the cyclic triaxial test (ASTM D5311,

2013). The first soil layer was poured in and pushed to the edges to ensure there were no large gaps between the soil and the membrane. The moist tamping method described in the ASTM standard was used to compact the soil and the height was checked with pre-calculations. The surface was then scratched to ensure interlocking between soil layers. This was done for all 5 soil layers. Filter paper and a porous stone were placed on top, and the construction mold was removed. Due to the application of high confinement, another membrane was placed. This is not required by the ASTM standard but was done due to complications with previous experience testing with high confinement for gravely soil. The sample was first flushed with CO_2 for 10 minutes which is a common method to aid in the saturation of dense soils in particular. An cell pressure 30 kPa larger than the CO_2 pressure was applied to ensure the soil would remain in its initial condition. Flushing with water followed this process and was left for at least 12 hours until 10 liters of water was obtained. The process of saturation began by applying back pressure to remove all air voids from specimen. The B-value check was performed several times to determine the completion of saturation. The B-value is calculated by the ratio of change in the pore water pressure by the change in chamber pressure and is required to be at least 0.95 before saturation is complete. Once the B-value reached 0.95, the consolidation process began. Following consolidation, a new cross-sectional area was calculated to determine the magnitude of load to be applied to the sample for load-controlled cyclic testing.

A series of load-controlled cyclic triaxial tests were performed in both undrained and drained conditions. The lack of research on gravelly soils is attributed to the requirement of more specialized large test equipment to comply with the ASTM standard of which the specimen diameter must be at least 6 times greater than the largest particle

size (ASTM D5311, 2013). With this material containing these larger particle sizes, it was therefore of interest to investigate the impact of sample size. In this study, two drained tests were completed in the specialized cyclic triaxial equipment that can accommodate testing of a sample with 6 inches in diameter and 12 inches in height. The remaining tests were performed in the second cyclic triaxial equipment that can accommodate a sample with 4 inches in diameter and 8 inches in height. Pictures of the sample preparation process and post-test observations for the 4-inch and 6-inch diameter samples are displayed in Figure 2.3 and Figure 2.4, respectively.

Figure 2.3 Pictures of sample preparation process and post-test observations for 4” sample diameter.

Figure 2.4 Pictures of sample preparation process and post-test observation for 6" sample diameter.

2.3 Testing Programs and Procedure

All the specimens were isotopically consolidated to reach the target initial effective stress of either 350 or 400 kPa. This high confinement was chosen to simulate stress conditions of mine waste facility. The difference in effective stress among these samples was due to the limitation in cell and back pressure available in the laboratory in some tests. Nevertheless, these stresses are relatively close and are normalized in the analysis, thus results are comparable. A series of undrained and drained cyclic triaxial tests were conducted with varying the cyclic stress ratio, CSR (ratio of the applied deviator stress to the effective confining pressure during cyclic loading) on specimens with two different relative densities. The testing program of undrained tests is presented in Table 2.2. The Test ID includes relative density condition denoted by "DU" (dense

undrained) or “MDU” (medium dense undrained) and is followed by the CSR applied to the sample. All undrained soil specimens were subjected to uniform sinusoidal cyclic loading with a frequency of 0.5 Hz for at least 25 cycles or until the pore water pressure ratio (defined as excess pore water divided by initial effective stress) reached 0.95. The cycle at which this criterion was reached for each sample is provided in Table 2.2. With this criterion, the number of loading cycles applied ranges from 25 to 580. The maximum loading cycles of 580 was applied to Sample DU_0.19 of very dense condition subjected to low CSR.

Table 2.2 Undrained Cyclic Triaxial Testing Program

Test ID*	Post Consolidation Relative Density (%)	Post Consolidation Relative Density (%)	CSR	Effective Confinement Pressure (kPa)	N at R_u 0.95
DU_0.19	100	114	0.19	400	562
DU_0.24		106	0.24		76
DU_0.28		105	0.28		36
DU_0.38		104	0.38		38
MDU_0.19	50 - 54	50	0.19	400	62
MDU_0.28		51	0.28		8
MDU_0.32		54	0.32		4

*All tests were performed on 4 inches sample size.

The testing program of drained tests is presented in Table 2.3. Test ID’s are defined as; “DD” dense drained, “DDL” dense drained large-scale triaxial, and “MDD” medium dense drained. To create truly drained condition of which no excess pore water pressure was developed, water was allowed to drain freely from the specimen and cyclic loading was applied very slowly. The volume drained water was measured continuously during the applied cyclic loading at a loading rate of 10% – 15% of the maximum load (approximately 17-19 kPa/minute depending on the CSR applied). The entire cyclic test

required 7 to 15 hours to complete for 15 number of cycles. Dynamic loads in the triaxial equipment could not be applied at the required low loading frequencies (< 0.0006 Hz). Therefore, monotonic loading sequences were used to apply triangular cyclic loading as shown in Figure 2.5. It is noted that a full cycle of triangular load was created from four monotonic loading stages.

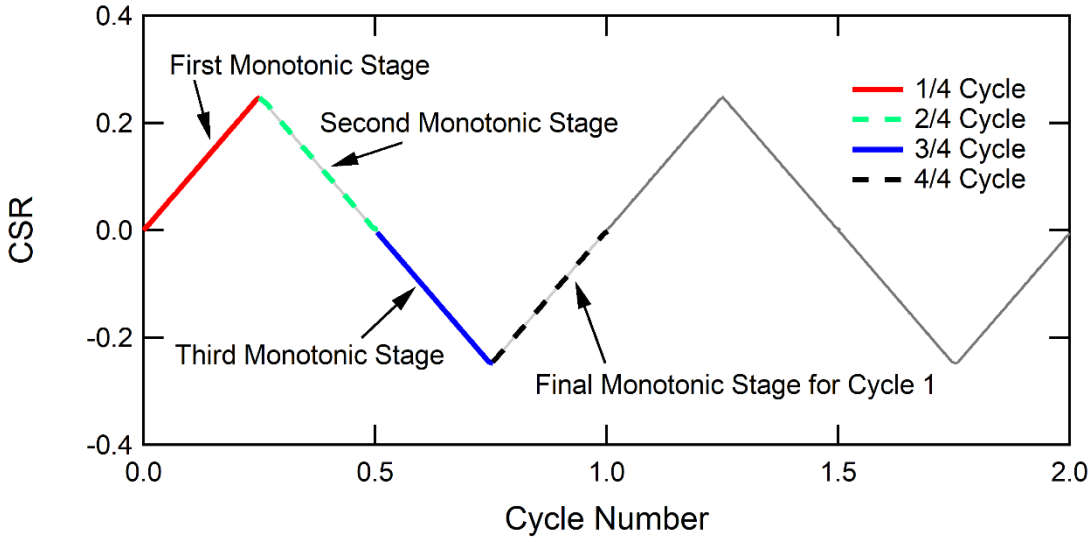

Figure 2.5 Schematic of drained cyclic loading used in this study.

Table 2.3 Drained Cyclic Triaxial Testing Program.

Test ID	Post Consolidation Relative Density (%)	Sample Size (inches)	CSR	Confinement Pressure (kPa)
DD_0.19	112	4”	0.19	400
DD_0.25	104		0.25	350
DD_0.28	102		0.28	400
DD_0.38	102		0.38	400
DDL_0.19	99	6”	0.19	350
DDL_0.38	101		0.38	350
MDD_0.19	53	4”	0.19	400
MDD_0.24	50		0.24	
MDD_0.28	53		0.28	

2.4 Results and Analysis

2.4.1 Post-consolidation

This section presents general observations for both undrained and drained cyclic triaxial tests. After each sample was saturated, isotropic consolidation was conducted and completed in a relatively short time (i.e., average 3 min for 4 inches, 10 min for 6 inches) due to the high permeability of the gravelly soils. The Terzaghi consolidation theory was used to calculate the time required for primary consolidation. The new sample volume was calculated using the known measured volume of water drained during consolidation. This was then used to calculate the change in relative density (D_R) of the specimen which is reported in Table 2.2 and Table 2.3. For the medium dense specimen, there is an increase in D_R from 30% to 50-53%. For the dense samples, an increase in D_R from 94% to slightly greater than 100% was observed. The value of D_R greater than 100% is theoretically impossible, therefore it is likely due to slight error in the determination of the maximum and minimum density from the laboratory test of the soil. It is expected that, due to the large consolidation pressure (400 kPa) the D_R appears to be "greater than" 100%. This is therefore understood as the soils densest possible state.

Post-test sieve analysis with sieve No. 4, 40, and 200 were performed for each sample to determine the occurrence of particle breakage. Figure 2.6 displays the post-cyclic grain size distributions of dense samples for sieve No. 4 and 200 to display particle breakage of gravel or sand that may have occurred due to the high density. There was a 3% decrease in gravel material and 1.5% increase in fine material. The results show that there was minimal particle breakage in the cyclic triaxial tests performed as there is slightly greater sand and fine material.

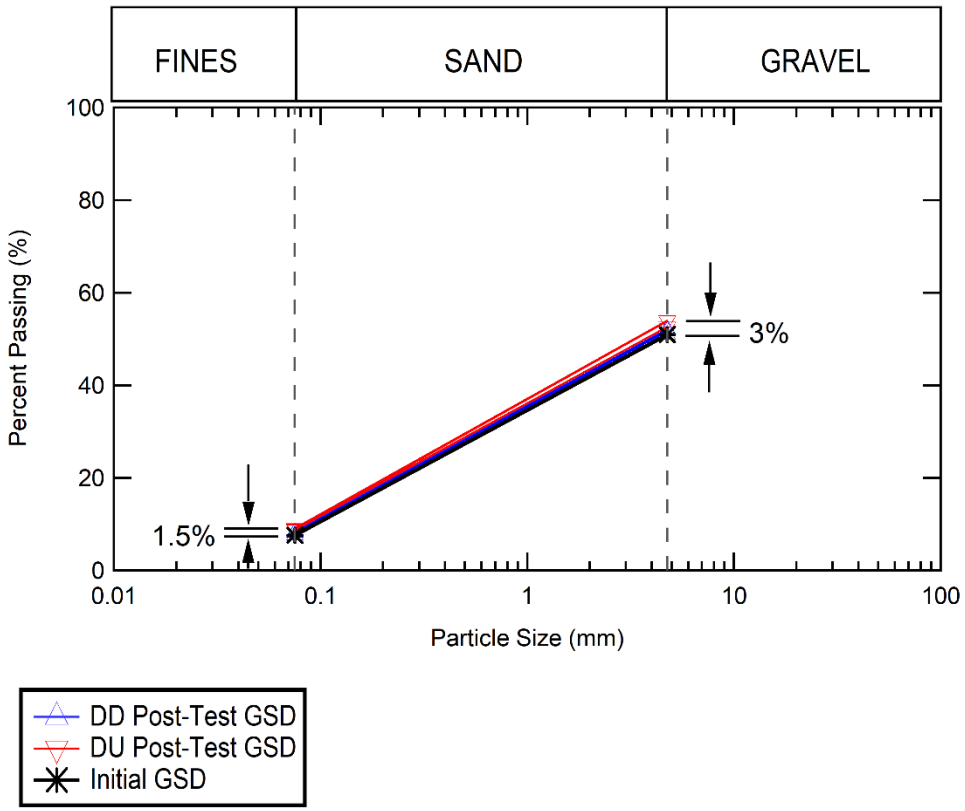

Figure 2.6 Pre and post-cyclic grain size distribution curves of dense samples to ensure minimal particle breakage.

2.4.2 Cyclic response of undrained samples

During undrained cyclic loading, water is not permitted to drain from the sample. This inhibits the ability of the soil to contract or dilate in response to the application of load, which induces excess pore water pressures. The excess pore water pressure changes the effective stress of the soil, which impacts the strength of the soil. As excess pore water pressures increase, the strength and stiffness of soil decrease which can lead to excessive axial strain or soil liquefaction. Soil liquefaction is a complicated phenomenon and has been extensively studied in sandy soils. Liquefaction behaviors of gravelly soils is discussed more in depth later in the section.

Figure 2.7 shows results of the undrained cyclic triaxial testing comparing between two samples subjected to CSR of 0.28. These results were chosen to display because the number of cycles to liquefaction were within a reasonable range to clearly evaluate the impact of relative density. In general, both samples demonstrate a similar trend for axial strain accumulating in the direction of extension (represented by negative axial strain in Figure 2.7). This development of axial strain was gradual at the start of cyclic loading and increased more rapidly as R_u approached 0.80. Once R_u reached a peak value the load decreased drastically, while the axial strain increased very little with each increasing cycle. This axial strain response once peak pore pressure has been reached, is consistent with previous studies of gravelly soil, as there was not a catastrophic development in strain that is typical of sand (Evans et al., 1995).

As R_u exceeded 0.8, the soil began to lose its strength as seen in Figure 2.7 where the CSR decreases as the soil cannot take this constant cyclic loading any longer. This reduction of CSR is greatest in extension, which corresponds to the observed accumulation of axial strain in the direction of extension. The medium dense (Sample MDU_0.28) soil had a higher rate of increase of R_u in the early cycles compared to the dense sample (Sample DU_0.28). Once the MDU sample reached R_u 0.80, the rate of increase of R_u was much higher compared to the DU sample. At this point, the MDU sample reached R_u of 0.95 within 3 cycles while the DU sample is subjected to more loading cycles. Also noticed is the ability of the DU sample to reduce the R_u within a cycle more than the MDU sample as shown on Figure 2.7 (a) and (b) for the cycle at which R_u reaches 0.90. Within this cycle, DU_0.28 was able to reduce the pore water pressure to 0.44, compared to 0.69 in MDU_0.28. This reduction in R_u corresponds to

dilation of the sample. This implies that dense gravelly soil has a greater ability to reduce excess pore water pressure during cyclic loading compared to medium dense gravelly soil. There is also a clear effect of relative density on the samples ability to withstand load. The dense sample can withstand some load while the medium dense sample appears to collapse and loses stiffness rapidly as observed from reduction of CSR in Figure 2.7.

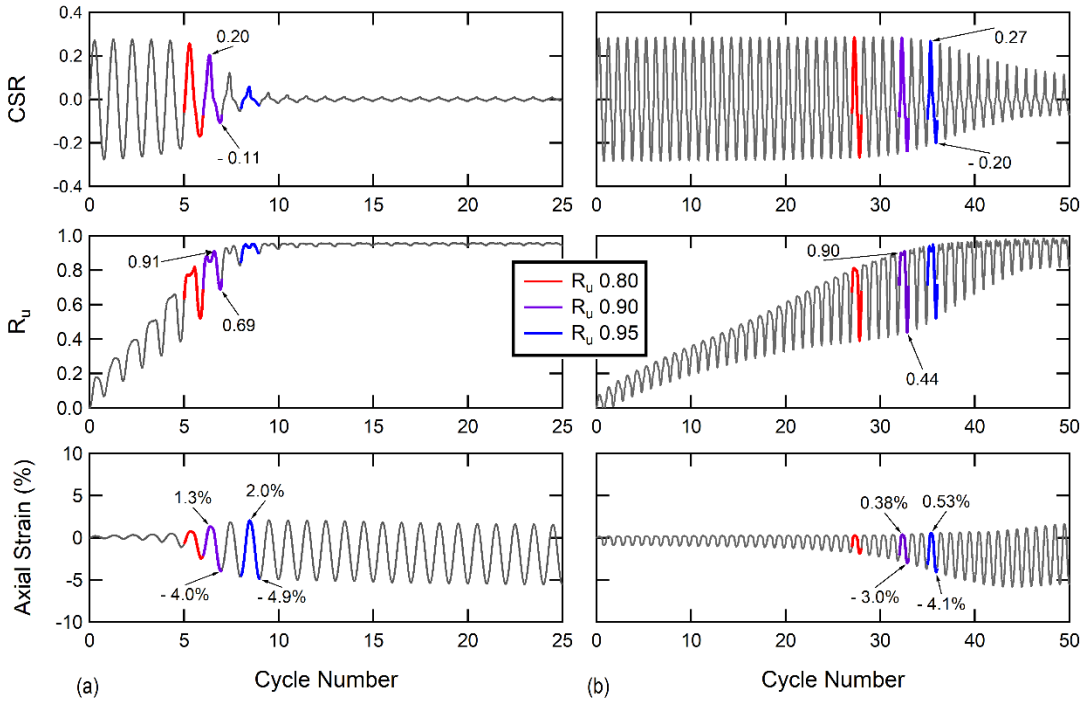

Figure 2.7 General results of undrained cyclic loading of CSR 0.28 for: (a) D_R = 53 %, and (b) D_R = 100 %.

Figure 2.8 below shows the pore water pressure buildup with the change in cyclic axial strain with increasing cyclic loading for the dense samples. Change in cyclic axial strain, ($\Delta\varepsilon_c$), describes the magnitude of increase in the cyclic axial strain from one cycle to the next. In other words, $\Delta\varepsilon_c$ describes the rate of accumulation in axial strain between cycles. The response of $\Delta\varepsilon_c$ as cyclic loading increased was of interest to consider its impact on R_u. At the beginning of cyclic loading, there is minimal accumulation in cyclic

axial strain as pore water pressures increase quickly. Figure 2.8 displays this clearly as in general, R_u reaches 0.6 before $\Delta\varepsilon_c$ surpasses 0.03 % (except Sample DU_0.38). As cyclic loading continues and R_u increases from roughly 0.6 to 0.9, $\Delta\varepsilon_c$ increases for each subsequent cycle. This phenomenon of increasing $\Delta\varepsilon_c$ begins at lower values of R_u as CSR increases. In other words, as greater cyclic stress is applied to the sample, the increase in the rate of accumulation of cyclic axial strain occurs at lower excess pore pressure generation in comparison to samples subjected to lower cyclic stress. For example, at $\Delta\varepsilon_c$ 0.1%, DU_0.24 had obtained R_u 0.87 while only 0.68 for DU_0.38. This implies that to obtain the same excess pore pressure in samples subjected to two different CSR, the sample undergoing higher CSR must suffer greater changes in cyclic axial strain. It is noted that the medium dense samples (not displayed) began to increase in $\Delta\varepsilon_c$ at lower values of R_u in comparison to the dense samples.

At some point in the cyclic loading, the $\Delta\varepsilon_c$ reaches a maximum value and begins to decrease approaching zero. This describes the behavior of cyclic axial strain gradually becoming more uniform. As the value of CSR applied to the sample increases, the magnitude of maximum $\Delta\varepsilon_c$ observed during cyclic loading increases. Additionally, for each CSR, the maximum $\Delta\varepsilon_c$ is greater for the medium dense samples compared to the dense. Identified in Figure 2.8, maximum $\Delta\varepsilon_c$ closely corresponds to R_u 0.90. This means that once R_u reached approximately 0.90, the cyclic axial strain with increasing loading cycles approached a relatively constant value hence there is no further accumulation of axial strain with number of cycles. As previously mentioned, this gradual rather than catastrophic accumulation in axial strain is characteristic of gravelly soil once failure has

occurred. Therefore, the observed behavior led to the liquefaction criteria defined for gravelly soils tested in this study, discussed in the following paragraph.

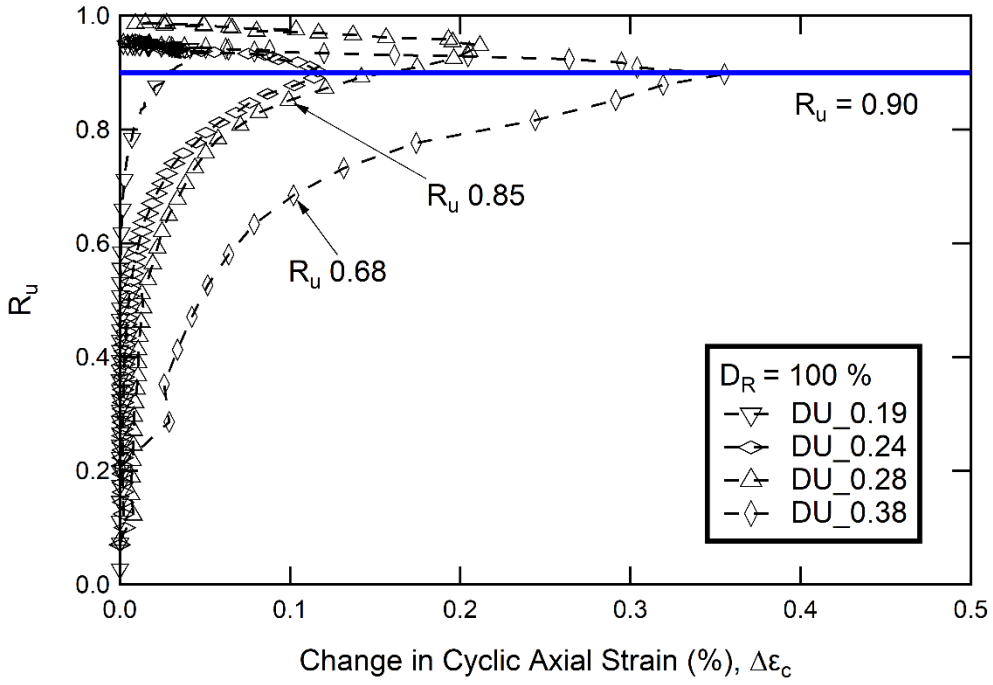

Figure 2.8 Variation of R_u with the change in cyclic axial strain.

Pore pressure generation

Soil liquefaction is defined as the subsequent loss in soil stiffness and effective stress due to excess pore pressure induced by an applied load (Boulanger and Idriss, 2004). Typically, there are three criteria that liquefaction can be based upon; pore water pressure, strength, or strain (Jiaer et al. 2004). In laboratory testing, this is often determined by the pore water pressure ratio, R_u, defined as the ratio of excess pore water pressure to effective confinement stress. However, there is great discussion on the ratio magnitude of R_u that should be used to define initial liquefaction. In literature, this is often taken as R_u value of 0.95 or double amplitude axial strain 2.5%. However, some soils may stop building up pore water pressure at R_u 0.90 (Jiar et al. 2004). Definitions of onset liquefaction for gravelly soils in literature vary from R_u 0.80 to R_u 1 (Banzibaganye

et al., 2022; Evans et al., 1995; Flora et al., 2012; Hubler et al., 2023,). These lower Ru values often are those that correspond to the cycle of triggering liquefaction defined by strain-based criterion. For example, Hubler et al. (2023) defined onset liquefaction as achievement of single shear strain amplitude 3.75% for gravel-sand mixtures performed in a cyclic simple shear device. It was reported that for this shear strain criterion, R_u values ranged from 0.8 to 1.0. The liquefaction criterion of 5% single amplitude shear strain and R_u 0.95 was also explored by Hubler et al. (2023) and was found to not have a significant effect on the pore water pressure generation. Flora et al. (2012) assessed liquefaction definition by comparison of the cycle corresponding to liquefaction triggering defined by double amplitude axial strain and R_u. It was found that the criterion 0.90 R_u agreed well with double amplitude 2.5% axial strain, and therefore both criteria were used to evaluate liquefaction.

Due to these varying definitions of liquefaction triggering found in literature, the criteria of R_u of 0.95 and 0.90 was investigated in this study through the assessment of excess pore pressure generation. Excess pore pressure generation is the relationship between the pore water pressure ratio, R_u and the normalized cyclic number, N/N_L. N_L is the cycle number at which initial liquefaction occurred based upon the criteria R_u 0.95 or 0.90. Figure 2.9 presents a comparison between these criteria for all the dense soil tests. For both criteria, DU_0.19 results as the lower bound while DU_0.38 as the upper bound. DU_0.19 tends to have a sharp increase in the rate of R_u for N/N_L 0.8 to 1. Contrarily, DU_0.38 has a decrease in the rate of R_u for N/N_L 0.8 to 1. Therefore, as the sample approaches liquefaction (N/N_L ranging from 0.8 to 1), the rate of excess pore pressure generation is higher for lower CSR. In Figure 2.9 (a), samples DU_0.24 and DU_0.38

nearly reach R_u 0.95 long before N/N_L reaches 1 as the relationship begins to flatten at N/N_L 0.7 and 0.5, respectively. Very small increases in the pore water pressure were observed after R_u reached a peak value. Hence, the onset liquefaction likely occurred before R_u 0.95. In addition, the R_u and N/NL relationships for R_u of 0.90 fall in narrower band than that of R_u of 0.95, and therefore presents less variability in pore pressure generation of gravelly soils. Furthermore, this band better represents the more consistent trend with the CSR. For example, as the CSR increases from 0.24 to 0.28, it would be expected that there would be an overall faster rate of R_u in the sample undergoing more load (CSR 0.28). However, in Figure 2.9 (a) in which N_L is defined as R_u 0.95, DU_0.24 has a much faster rate of R_u compared to DU_0.28. Jiar et al. 2004 found that when evaluating R_u at liquefaction defined by strain-based criteria, dense samples had lower R_u values than looser samples. It was found that at the strain-based defined cycle triggering liquefaction, corresponding values of R_u were as low as 0.8. This implies that a stiffer material may require a lower R_u threshold to be used for a pore pressure-based liquefaction criterion. This provides a possible explanation for the liquefaction criteria of R_u 0.90 to better define liquefaction for this gravelly soil than R_u 0.95 that is typically used for sands.

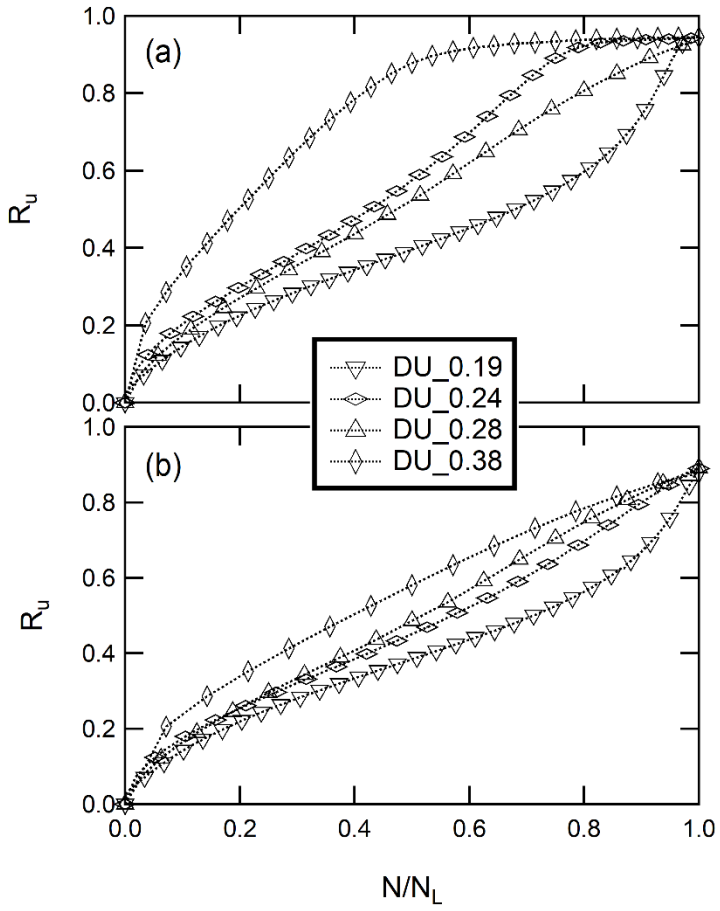

Figure 2.9 Pore pressure generation with N/N_L for N_L defined as: (a) R_u 0.95, and (b) R_u 0.90.

Hubler et al. (2022) explored the pore pressure generation model for gravel, sand, and gravel-sand mixtures and found that the coefficient of uniformity, C_u, has significant influence on the excess pore water pressure generation. They compared pore pressure generation relationships of well-graded and uniform gravelly soils and found that the well-graded soils had a faster rate of pore pressure buildup at the initial cycles of loading ($N/N_L = 0.2$). Hubler et al. (2022) found a linear increase in R_u for all normalized cycles of N/N_L as C_u increases. This relationship included results of gravel-sand mixtures from their study as well as literature. They also found that with an increase in relative density, there was an increase in R_u in the earlier cycles of cyclic loading. Both findings by Hubler

et al. (2022) can be supported by the results of this study in Figure 2.10. At N/N_L of 0.2, MDU_0.19 has a R_u of 0.15 while DU_0.19 has a R_u of 0.22. This difference in R_u between the medium dense and dense samples of comparable CSRs is similar but slightly decreases with increasing CSR. As displayed on Figure 2.10, for N/NL 0.2, DU_0.28 reaches a R_u only 0.03 greater than MDU_0.28. As N/N_L increases, this trend becomes less significant for the higher CSR values. For example, at N/N_L 0.80 DU_0.28 and MDU_0.28 both reach R_u 0.76. This implies that a dense well graded gravelly soil is more susceptible to high pore water pressures in the early cycles of loading. Also, the impact of density on normalized excess pore water pressure generation is greater for samples subjected to lower CSR.

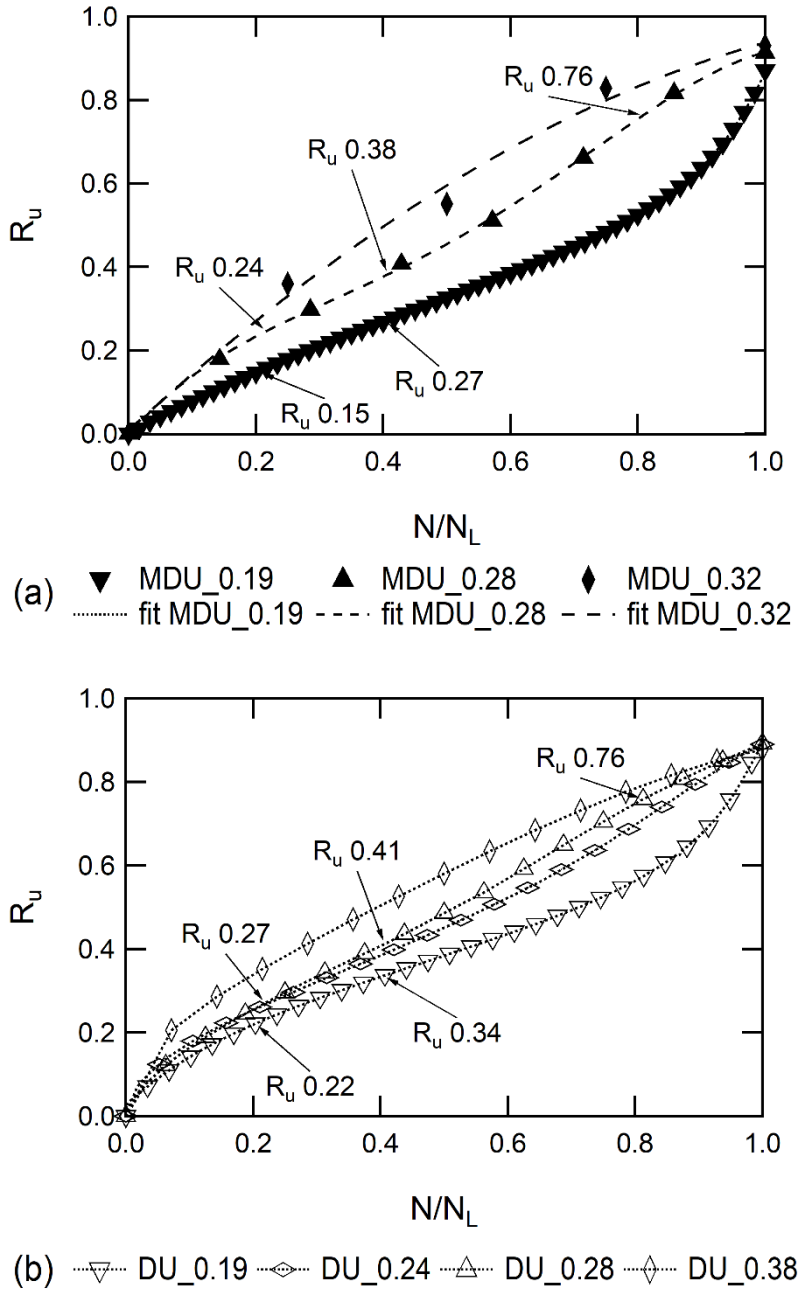

Figure 2.10 Excess pore water pressure generation versus N/N_L with N_L defined as Ru 0.90 for: (a) D_R 53 %, and (b) D_R 100 %.

Cyclic Resistance Ratio

The CSR needed to attain liquefaction in a particular number of cycles is known as the cyclic resistance ratio (CRR). The relationship of CRR with number of cycle is represented by:

$$CRR = a(N^{-b})$$

Eq. 2.1

where the parameters *a* and *b* can be determined by regression (Boulanger et al. 2004).

Figure 2.11 presents the relationship of cyclic resistance ratio (CRR) and the number of cycles to cause initial liquefaction (N_L) for the medium dense and dense samples. For the same CRR, the MDU samples reached the cycle of liquefaction (N_L) at much lower number of cycle than the DU samples. $CRR_{7.5}$ corresponds to an CSR adjusted for earthquake magnitude M_w = 7.5, defined as 15 cycles of cyclic loading. $CRR_{7.5}$ in this case must be corrected for field conditions as cyclic triaxial samples are subjected to isotropic consolidation (K_0 = 1). Field conditions were assumed K_0 = 0.5. $CRR_{7.5}$ for MDU samples reduced from 0.24 (Triaxial Test) to 0.14 (Field), and 0.35 (Triaxial Test) to 0.21 (Field) for DU samples. Therefore, the CRR obtained from triaxial test is conservative. The general trend of the relationship for both densities of soil is similar, presented as an exponential decay in N_L as CRR increases. Typically, *b* is 0.34 for sands and 0.14 for clays (Boulanger et al., 2004). The values of *b* defined in Figure 2.11 are intermediate of these (0.21 and 0.17). El Takch et al. (2016) investigated CRR for silt and sandy silt materials. They also found intermediate results of *b* and compare their average to that of a fine-grained tailings material, 0.19. As discussed in material properties, the material in this study is mine waste rock containing 8% fines. This

provides a possible explanation for the similarity in parameter *b* and suggests that fine content has an impact on *b*. El Takch et al. (2006) also noticed a decrease in *b* with increase in D_R. This is contrary to this study, as Figure 2.11 shows the values of both *a* and *b* are larger for the dense relationship in comparison to the medium dense.

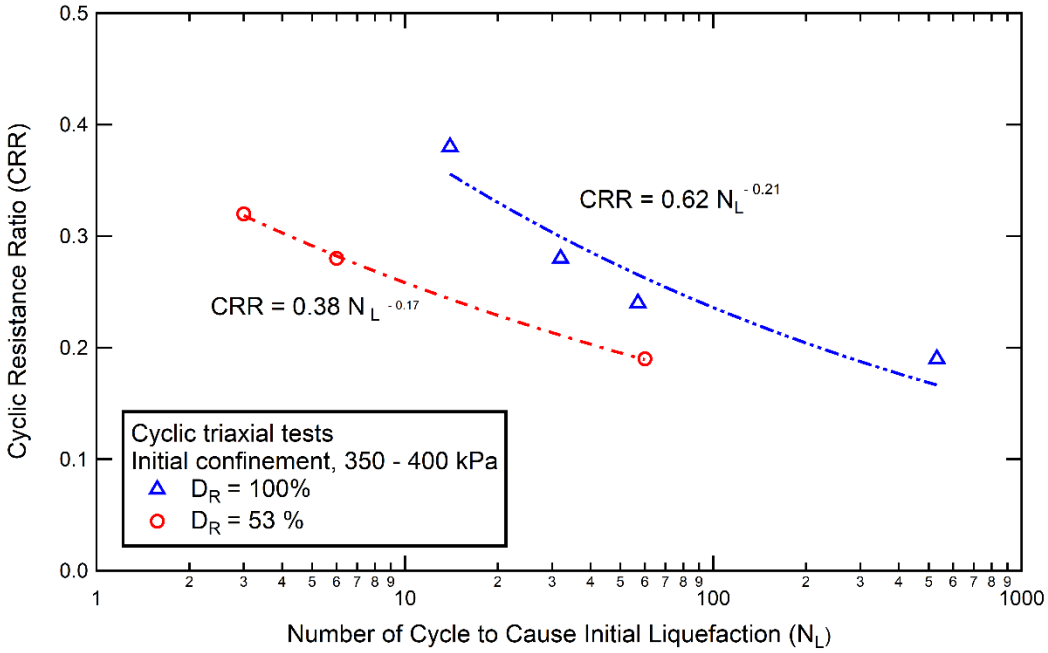

Figure 2.11 Cyclic Resistance Ratio (CRR) for initial liquefaction (R_u = 0.90) performed in cyclic triaxial tests.

2.4.3 Cyclic response of drained samples

Figure 2.12 presents CSR, R_u, axial strain, and volumetric strain results for DD_0.25 and MDD_0.24. These two tests were chosen because they have similar CSR value, therefore provide a relevant comparison between the samples with two different densities. The drained cyclic triaxial test is performed in such a way that there is no excess pore pressure development in the soil as shown in Figure 2.12. Consequently, the sample develops cyclic axial strain which coincides with the CSR. Amplitude of cyclic axial strain appears to be constant throughout the test in exception to the axial strain at

the first cycle of MDD_0.24. The initial axial strain is high at the first cycle due to the initial densification of the soil but the cyclic axial strain for the rest of cycles remains relatively constant. The accumulated axial strain is in compression for both samples but the total amount of axial strain in MDD_0.24 sample is twice the axial strain of DD_0.25. It is noted that this observation is contrary to the undrained tests, which accumulated axial strain in the extension direction. At each loading cycle, the volume of drained water from the sample was measured to determine the accumulated volumetric strain calculated by the change in volume divided by the volume prior to cyclic loading. Cyclic characteristics of volume change were observed for both samples and the accumulated volume increased as the number of cycle increased. Similar to the axial strain, the volumetric strain of MDD_0.24 is about twice the volumetric strain of DD_0.25.

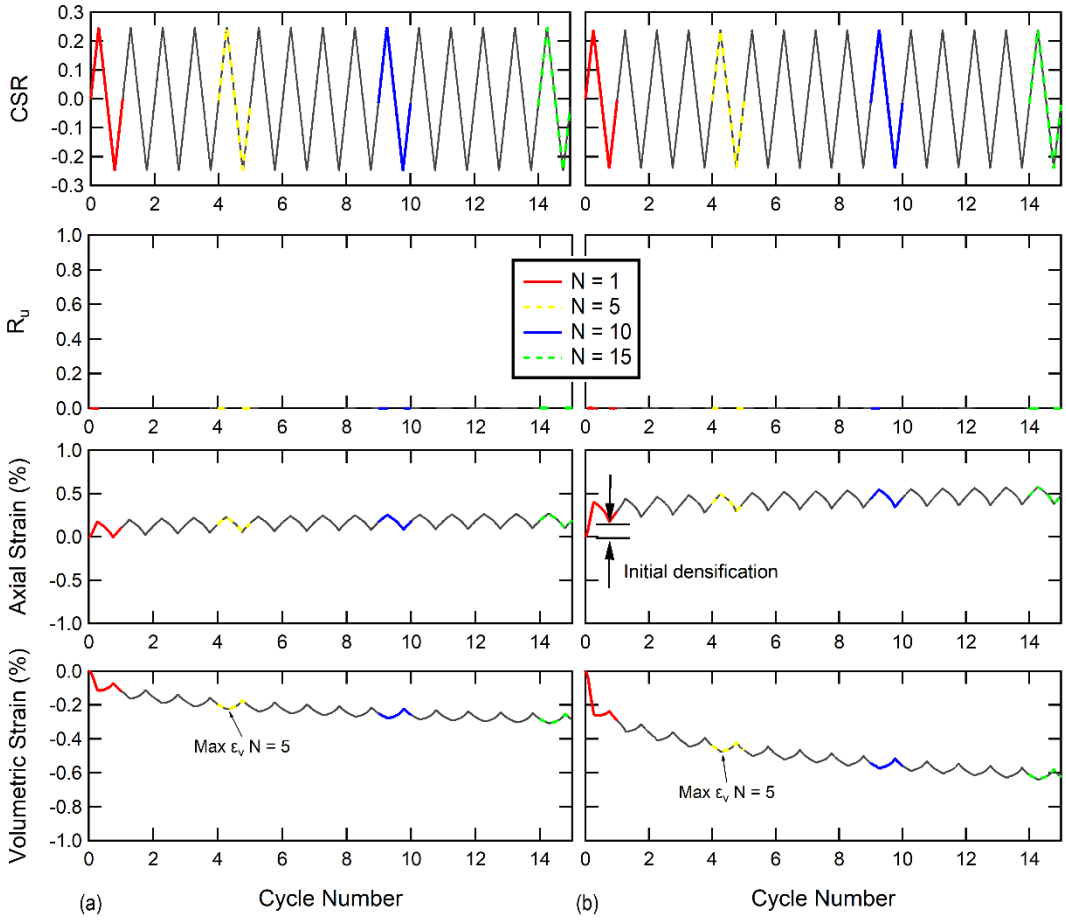

Figure 2.12 Drained cyclic triaxial results of CSR, Ru, axial strain (%), and volumetric strain (%) for samples: (a) DD_0.25, and (b) MDD_0.24.

The results of accumulated volumetric strain at the end of 15 cycles of cyclic loading for various values of CSR are shown in Figure 2.13. It is clearly seen that increasing volumetric strain is a consequence of increasing CSR. This consequence is less for the dense sample. There is a greater exponential increase in volumetric strain for the medium dense sample subjected to CSR greater than about 0.25. As previously mentioned, the effect of sample size was of interest in this study due to the large particle size in the sample. As shown in the figure, the volumetric strains of the 4-inch and 6-inch sample sizes agreed considerably well. This implies that the influence of larger particle size of about 6% by weight is minimal, therefore the 4-inch sample can be used. This

finding could have great implications for research on gravelly soils as currently research is hindered by the rarity of large scale triaxial equipment.

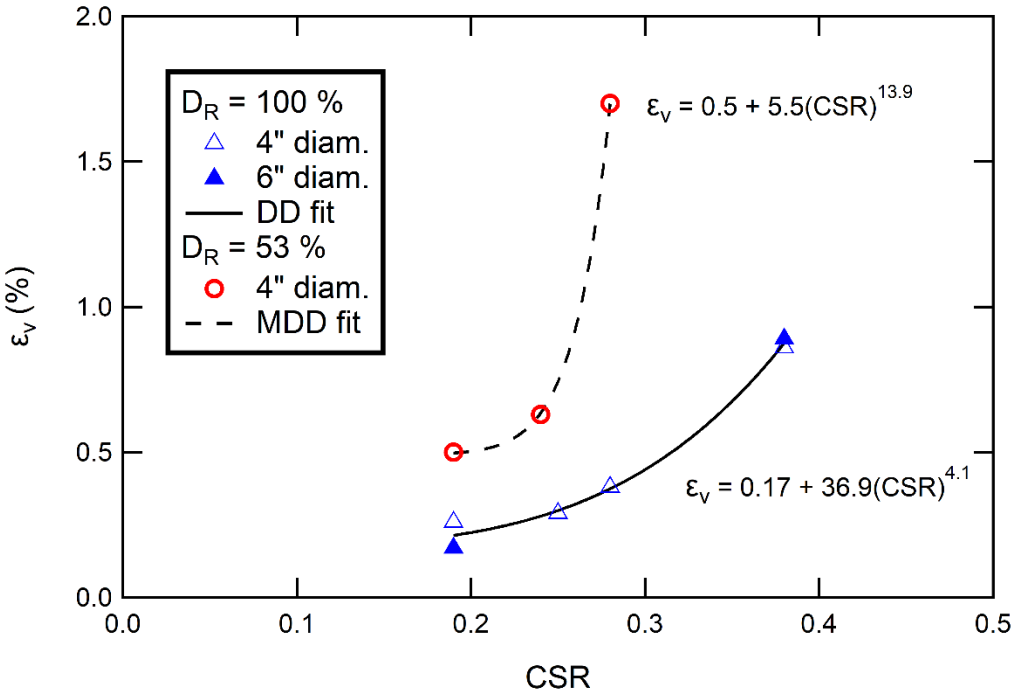

Figure 2.13 Consequence of volumetric strain (%) with varying applied CSR to medium dense and dense gravelly soil.

2.5 Undrained and Drained CTX Correlations

This section describes the process of extracting data from the undrained and drained cyclic triaxial tests for the purpose of assessing correlations. A correlation of volumetric strain and excess pore water pressure is of interest to relate the consequences of the undrained and drained conditions. As mentioned, settlement in sands due to pore pressure dissipation post-liquefaction has been widely studied (Ishihara & Yoshimine, 1992; Stamatopoulos & Stamatopoulos, 2004; Tokimatsu & Seed, 1987). This experimental assessment is commonly done with the constant volume cyclic direct shear device. Excess pore pressures build as the soil is subjected to cyclic loading, and afterwards the volume change can be measured. This requires the assumption that volume

change occurs after excess pore pressure has developed rather than simultaneously with cyclic loading. In the cyclic triaxial test, the ability to measure volume change after undrained loading is not available. Therefore, the excess pore water pressure and volumetric strain with number of cycle must be measured in two separate tests (i.e., undrained, and drained, respectively) and later correlated. This correlation requires the assumption that at a given cyclic axial strain, the amount of excess pore water measured in the undrained test would cause the volume change measured in the drained test. Therefore, in this study, a correlation is developed for both drainage conditions with increasing cyclic axial strain. Following this process, a correlation of volumetric strain and R_u was developed by relating the two consequences based upon the corresponding cyclic axial strain. This required extraction of cyclic axial strain, volume change for the drained tests, and excess pore pressures for the undrained tests. The drained tests result in data represented by coordinates ($\boldsymbol{\varepsilon}_c$, $\boldsymbol{\varepsilon}_V$) while the undrained tests result in data represented by ($\boldsymbol{\varepsilon}_c$, R_u). The relation ($\boldsymbol{\varepsilon}_V$, R_u) is then developed based on these two original correlations with $\boldsymbol{\varepsilon}_c$. The process is provided in detail in the following sections.

2.5.1 Undrained data extraction process for cyclic axial strain correlation

The following section describes the extraction of ($\boldsymbol{\varepsilon}_c$, R_u) from the undrained tests. Additionally, the analysis process of undrained data used to develop the correlation with cyclic axial strain is described.

Data extraction

In each undrained triaxial test, a $R_{u,MAX}$ was defined for every cycle. This represents the maximum R_u reached over that entire cycle, shown in Figure 2.14 as an example of Cycle 5. To calculate the cyclic axial strain, the maximum compressive axial

strain ($\boldsymbol{\varepsilon}_{com}$) and maximum extensive axial strain ($\boldsymbol{\varepsilon}_{ext}$) were defined for each cycle. The cyclic axial strain was found by taking the average of these two values for each cycle number:

$$\varepsilon_c = \frac{\boldsymbol{\varepsilon_{com}} - \boldsymbol{\varepsilon_{ext}}}{\mathbf{2}}$$

Eq. 2.2

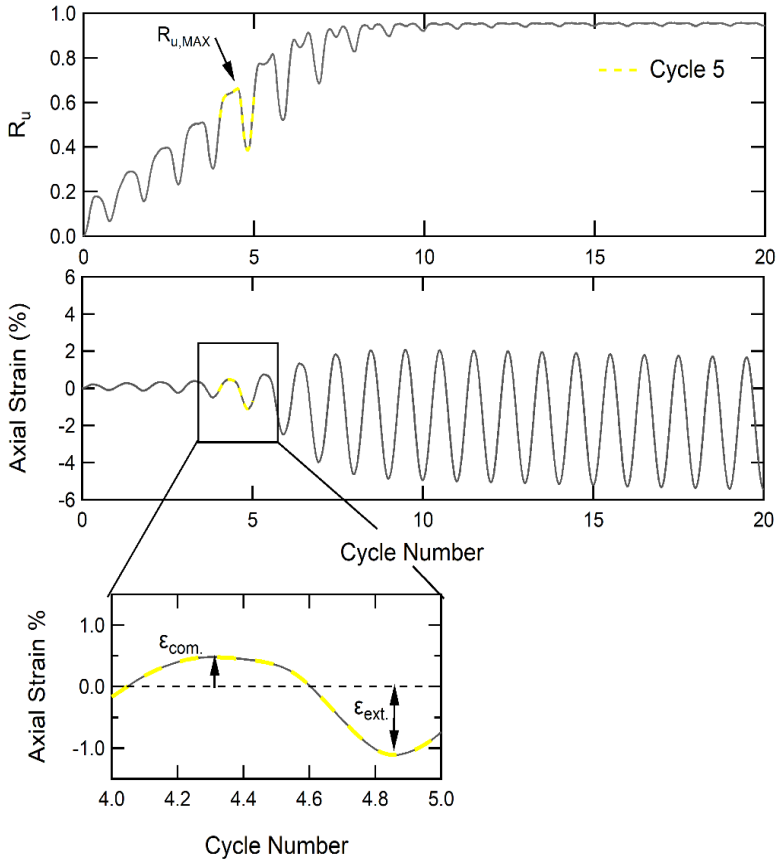

Figure 2.14 Definition of $R_{u,MAX}$ and $\boldsymbol{\varepsilon}_{com}$ and ε_{ext} for undrained tests.

After examining the axial strain data for all undrained testing results, it was noticed that during the first cycle there was an initial axial strain that did not represent true soil response. This is displayed in Figure 2.15 (a) and Figure 2.16 (a), as R_u of zero does not correspond to zero $\boldsymbol{\varepsilon}_c$. This is believed to be due to a gap between the loading

plate and the soil specimen prior to cyclic loading. This gap could result from; an unlevel surface due to the variability of large particle sizes, or a lack of full suction of the top cap of the soil specimen to the loading plate. The offset $\boldsymbol{\varepsilon}_c$ was then adjusted by removing the axial strain at the first cycle ($\varepsilon_{c,N=1}$). This Adjusted Cyclic Axial Strain was calculated as follows:

$$\varepsilon_{adjusted\ cyclic} = \varepsilon_c - \varepsilon_{c,N=1}$$

Eq. 2.3

The relationship between R_u and Adjusted Cyclic Axial Strain are shown in Figure 2.15 (b) and Figure 2.16 (b) for both the dense and medium dense samples. The R_u increases as the axial strain increases and the rate of increasing for this relationship depends on the CSR. At lower CSR, the sample undergoes more cycles at small axial strain as R_u increases at a faster rate compared to the axial strain. At higher CSR, the magnitude of axial strain increases more rapidly than the R_u. Therefore, the R_u reaches a maximum value at different axial strains depending upon the CSR.

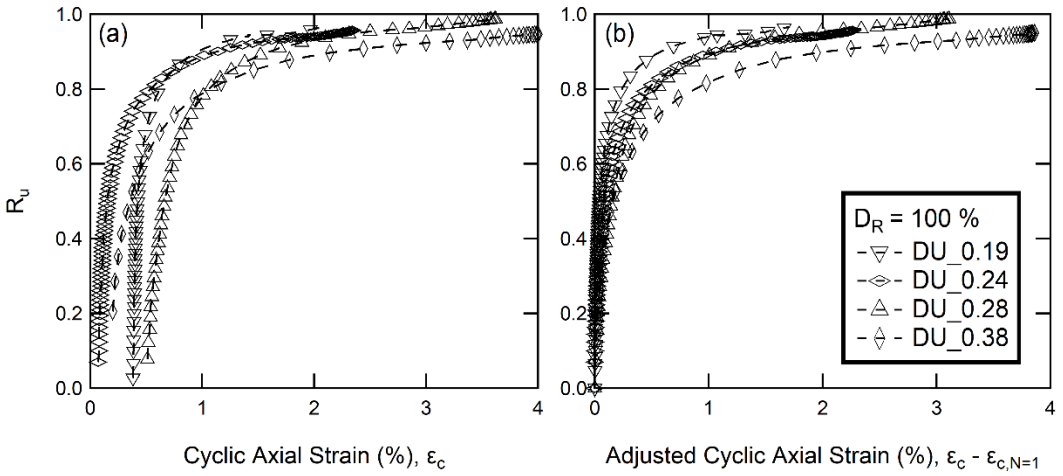

Figure 2.15 Dense Undrained CTX pore water pressure response with increasing: (a) Cyclic Axial Strain (%), and (b) Adjusted Cyclic Axial Strain (%).

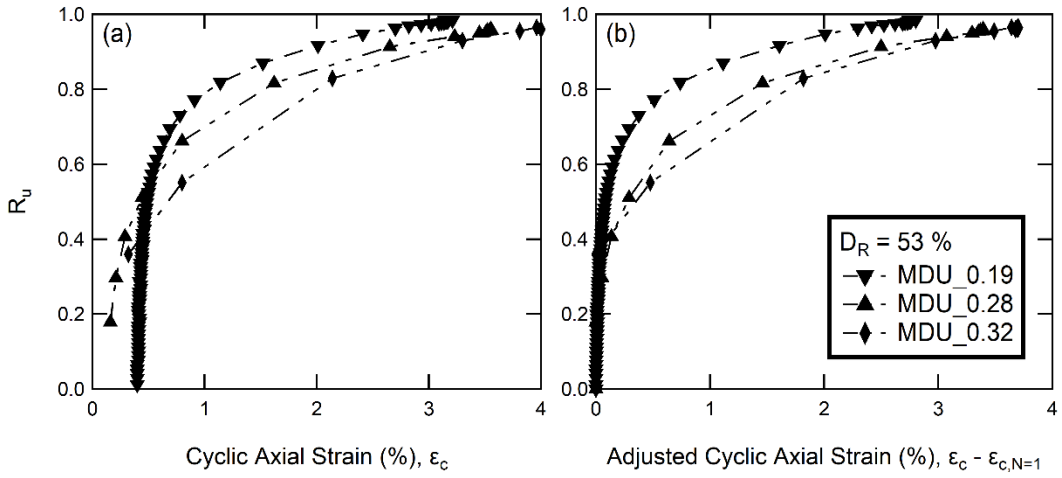

Figure 2.16 Medium Dense Undrained CTX pore pressure response with increasing: (a) Cyclic Axial Strain (%), and (b) Adjusted Cyclic Axial Strain (%).

R_u and cyclic axial strain curve fitting and correlation, (ε_c , R_u)

This section describes the relationship defined for the undrained tests with data points ($\boldsymbol{\varepsilon}_c$, R_u). The consequential R_u corresponding to $\boldsymbol{\varepsilon}_c$ is then used to relate to ($\boldsymbol{\varepsilon}_c$, $\boldsymbol{\varepsilon}_V$) obtained from the drained tests. The data from 7 undrained tests of this study are shown in Figure 2.17. The relationship between R_u and cyclic axial strain is best fitted by a log normal relationship as shown in Figure 2.17. This curve fit was chosen because it best represented the complete data set of varying CSR. Chi-square is a tool to assess the best values for the coefficients within a fitting equation. A minimum Chi-square represents the best values for a data set. Chi-square is calculated by:

$$\sum_i \left(\frac{y - y_i}{\sigma_i}\right)^2$$

Eq. 2.4

The medium dense relationship of R_u and cyclic axial strain (Chi-square of 0.18) can be approximated by:

$$R_u = \frac{1.1}{1 + (\frac{0.14}{\varepsilon_c})^{0.60}}$$

Eq. 2.5

The dense relationship is approximated by Eq. 26 below with a Chi-square of 2.0, displayed in Figure 2.17 (b). The fitting curve is a good fit of the data set for very low strain (~ 0.1 %) and higher strains (~ > 1 %) but is an upper bound of dataset for strains in the range of ~ 0.1 to 1 %. Even so, after an exploration of several functions, this function best represents dense samples in this testing program. Therefore, the dense correlation of R_u and cyclic axial strain is as follows:

$$R_u = \frac{1.0}{1 + (\frac{0.05}{\varepsilon_c})^{0.75}}$$

Eq. 2.6

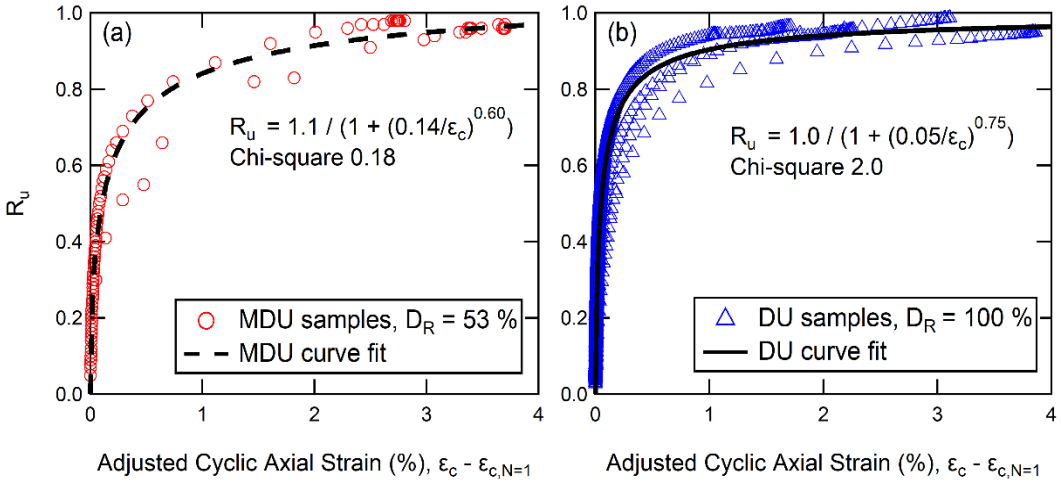

Figure 2.17 Data and correlations of relationship of R_u and increasing cyclic axial strain (%) for: (a) medium dense, and (b) dense samples.

Figure 2.17 shows that the dense samples develop R_u with cyclic strain at a faster rate compared to the medium dense samples. This is contrary to the relationship of R_u

with number of cycle as mentioned previously in Section 2.4.2, Figure 2.7. It was discussed that considering the development of R_u with number of cycles, the medium dense samples have a faster rate of excess pore pressure compared to the dense. However, since less strain is produced at each number of cycle for the dense samples, the rate of R_u with cyclic axial strain is faster. This is likely due to the lower permeability for the denser state, in turn producing more excess pore water at lower cyclic axial strain. Furthermore, assessment of the excess pore pressure generation relationship presented in Section 2.4.2, Figure 2.10, resulted in the same finding as the relationship of R_u and cyclic strain. As discussed, this similar observation was observed in the relationship of R_u and N/N_L by Hubler et al., 2022, in which denser soils had greater pore water pressure generation in earlier cycles. This trend also applies to Figure 2.17, as the dense samples had higher pore water pressure generation corresponding to the initial cyclic axial strain. This implies that behavior in the development of R_u with the normalized cycle number (N/N_L) is more closely related to that with cyclic strain than number of cycle. Figure 2.17 shows that the relationship for the dense soil results in R_u of 0.90 at a cyclic axial strain of 1%. As the cyclic axial strain increases past 1%, the R_u remains between 0.90 to 0.95. Comparatively, the medium dense sample approaches R_u 0.90 at the cyclic axial strain 2.5%. As the cyclic axial strain increases further, R_u continues to increase approaching 0.95 to 1.0. This implies that dense gravelly soil has a rapid onset increase in R_u at small cyclic strains and is not as susceptible to large increases in R_u as cyclic strains increase past 1%. Medium dense soils have a slower rate of R_u development at small cyclic strains and R_u continues to increase as cyclic strain increases.

2.5.2 Drained data extraction process for cyclic axial strain correlation

The following section describes the extraction of (ε_c , ε_V) from the drained tests and presents a correlation between volumetric strain and cyclic axial strain. All drained tests as previously mentioned were cyclically loaded for 15 cycles with very low frequency to ensure no development of pore water pressure.

Data extraction

Figure 2.18 describes the process used to obtain the cyclic axial strain and volumetric strain for the drained tests of medium dense sample. This process is very similar to undrained tests. The cyclic axial strain was calculated as an average of the maximum extensive and compressive axial strain for each cycle. The volumetric strain was taken as the maximum during each cycle.

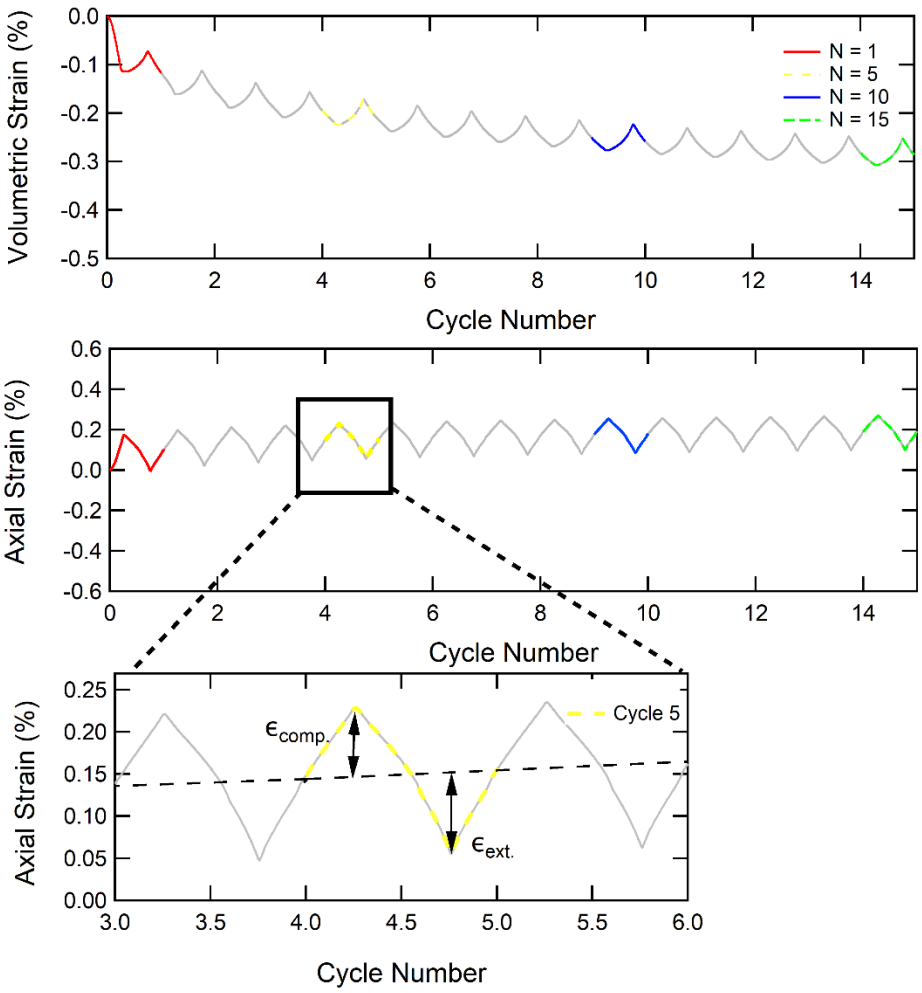

Figure 2.18 Sample data of volumetric strain and definitions of $\varepsilon_{com.}$ and $\varepsilon_{ext.}$ for drained CTX tests.

It is noted that an issue with the equipment was noticed when applying extension to several dense samples (DD_019, DD_038, DD_028, DD_025). It was determined that this issue was occurring due to slippage of the loading stem, producing extensive axial strain data not representative of soil behavior. This is shown in Figure 2.19 below. Since the extension data does not represent true soil response, the axial compressive strain was used to make correlations as opposed to an average. This compressive strain agrees well with the compressive strain of samples tested after the equipment causing this issue was addressed.

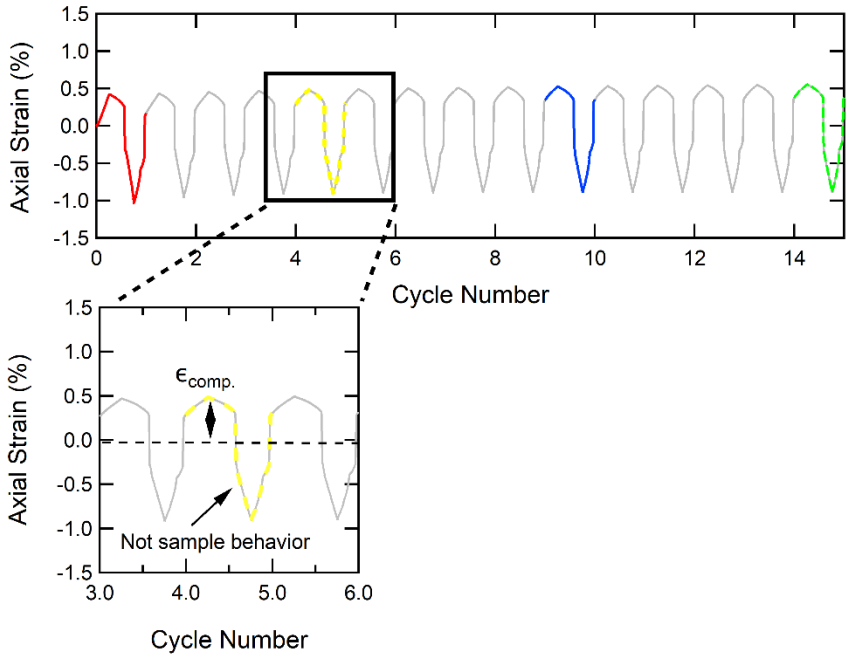

Figure 2.19 Display of CTX equipment issue producing cyclic axial extensive strain not representative of true soil behavior.

Volumetric strain and cyclic axial strain curve fitting and correlation, (ε_c , ε_V)

The following section presents the results of volumetric strain progression as cyclic axial strain increases in both dense and medium dense samples. The consequential $\boldsymbol{\varepsilon}_V$ corresponding to $\boldsymbol{\varepsilon}_c$ was used to relate to ($\boldsymbol{\varepsilon}_c$, R_u) of the undrained tests. The data from the 8 drained tests (4-inch diameter sample size) of this study are combined as shown in Figure 2.20. Generally, the dense samples produced less volumetric strain for the same cyclic axial strain compared with the medium dense samples. This is to be expected as the medium dense samples have higher void ratio and would be more susceptible to higher volumetric strain when undergoing cyclic loading.

Figure 2.20 presents the correlations of volumetric strain and cyclic axial strain for the medium dense and dense samples, represented by a power function. The dashed line is used to represent an uncertainty in the correlation as there is no data available in

this range of cyclic strain. However, it is likely that data within this range would agree with the correlation. It is important to note that due to the limited data of cyclic axial strain below 0.1%, the approximated curve fitting for cyclic axial strains below 0.1% is uncertain. However, the two correlations suggest that the relative density at these low cyclic axial strains does not greatly impact the volumetric strain response. More data would be needed to investigate the volumetric strain at low cyclic strain.

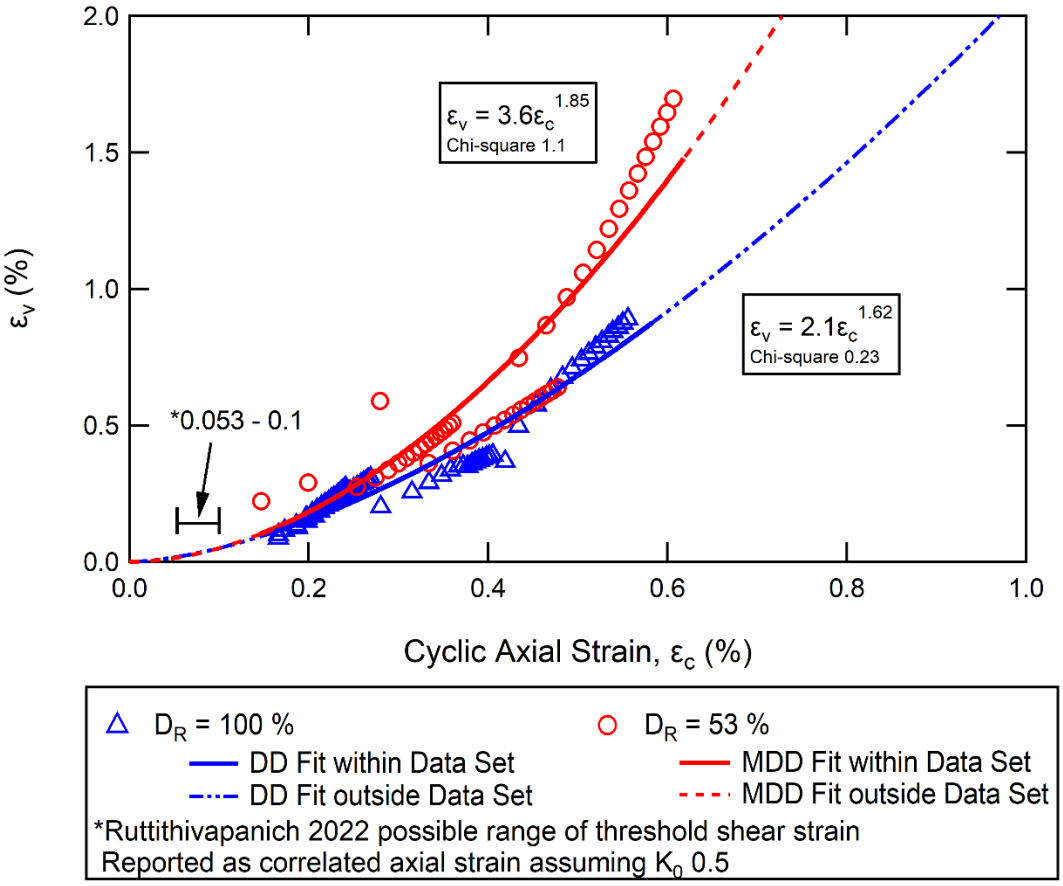

Figure 2.20 Data and correlations of relationship of volumetric strain and cyclic axial strain for medium dense and dense samples.

The development of volumetric strain at low cyclic axial strains (<0.2%) are very similar for medium dense and dense samples. As cyclic strain increases, the rate of volumetric strain development in the medium dense sample becomes increasingly faster

compared to the dense sample. Particularly, after about 0.25% cyclic axial strain, there is a sharp increase in the development of volumetric strain observed for the medium dense samples compared to the dense samples. This can be understood by the curve fit power equations as well (medium dense is raised to a power of 1.85 while dense is 1.62). At this point the dense samples require more cyclic axial strain to obtain further volumetric strain. This implies that density has more of an impact at higher axial strains (greater than 0.25%), as the low strain data produces approximately the same volumetric strain of medium dense and dense samples.

Shown in Figure 2.20, the curve fitting functions start at the origin and suggest that the volume change increases concurrently with cyclic strain. However, numerous research studies evaluate the volumetric cyclic threshold shear strain, defined as the cyclic shear strain at which "significant permanent changes of soil microstructure" occur (Vucetic, 1994). Vucetic (1994) summarizes typical values of volumetric cyclic threshold shear strain for sands found in past studies, ranging ~ 0.01 to 0.02 %. Due to lack of data available at very low strain levels from cyclic triaxial tests, it is not possible to report the cyclic threshold strain for gravelly soils tested in this study. Research by Ruttithivapanich (2022) on gravelly soil material similar to this study found that the possible threshold shear strain for pore pressure development ranged 0.08 to 0.15 %. Assuming a K_0 value of 0.5, the corresponding range for cyclic axial strain is 0.053 to 0.1%. This possible range of threshold shear strain is labeled in Figure 2.20 as correlated axial strain.

2.5.3 Correlation of R_u and volumetric strain

This section combines the correlations extracted from the undrained and drained tests to obtain a prediction of R_u with volumetric strain. Equations 5-6 and the power

functions in Figure 2.20 were used to correlate the pore water pressure and volumetric strain at corresponding values of cyclic axial strain. This method was used to obtain coordinates ($\boldsymbol{\varepsilon}_V$, R_u) and plotted in Figure 2.21. Since the behavior at low strains is not clearly observed, Figure 2.21 (b) shows the same data as Figure 2.21 (a) but with a semi-log scale. It appears that the R_u - $\boldsymbol{\varepsilon}_V$ relationships for dense and medium dense soil are similar for volumetric strains less than 0.001%. The initial buildup of pore water pressure in both samples occurs in association with very little volumetric strain. The volumetric strains begin to increase when R_u surpasses about 0.6. With this volumetric strain increase, the medium dense sample continues to build excess pore pressure but more slowly, as there is a sudden rapid increase in volumetric strain. In the dense samples the pore water pressure reaches a higher ratio (about 0.85) before there is this rapid increase in volumetric strain. This implies that the excess pore water pressure must increase more in dense soil to obtain the same amount of volumetric strain as medium dense soil. This impact of relative density on the behavior of the relationship between excess pore pressures and volumetric strain is logical.

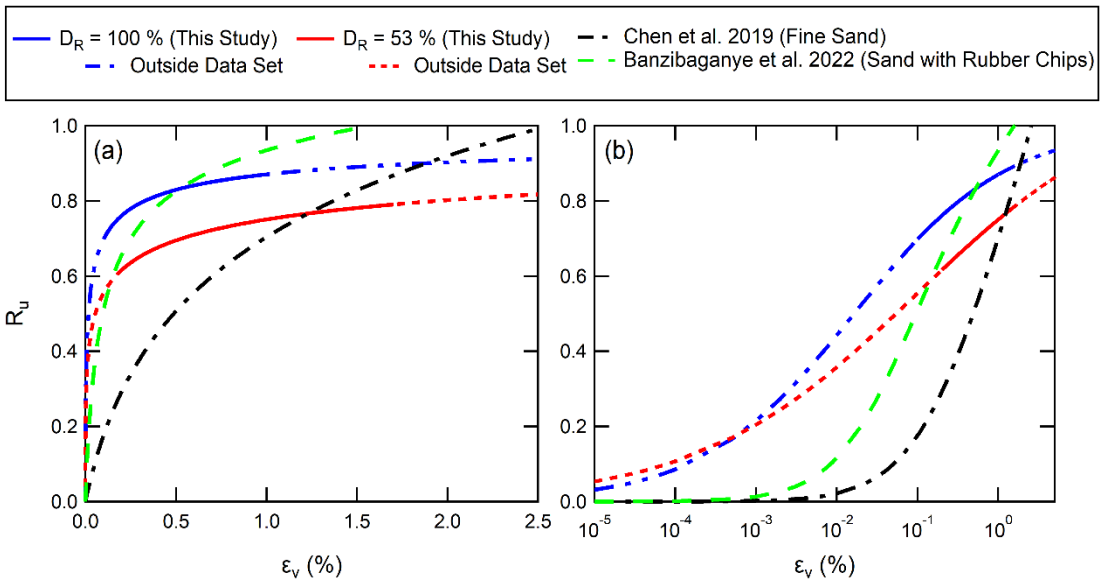

Figure 2.21 Correlation of R_u and volumetric strain displayed on: (a) linear scale, and (b) semi-log scale.

Comparisons of the (ε_V, R_u) in this study with two other studies available in literature are presented in Figure 2.21. Chen et al. (2019) correlated the excess pore water pressure with volumetric strain from a series of undrained and drained multistage and single stage strain controlled cyclic triaxial tests performed on fully saturated fine sand samples by the following equation:

$$r_u = m(nln + 1)$$

Eq. 2.7

where*: m* and *n* are fitting parameters found by the pore water pressure volumetric strain relationship. As shown in Figure 2.21, this relationship defined for fine sands has a slower rate of increase in R_u with volumetric strain compared to the gravelly soil in this study.

Banzibaganye et al. (2020) correlated excess pore water pressure from undrained CTX testing to cumulative volumetric strain from drained tests by the following equation:

$$r_u = \frac{\varepsilon_{v,cy}}{0.07m + \varepsilon_{v,cy}^{0.9}}$$

Eq. 2.8

where r_u is an average pore water pressure of max and minimum across cycle; and $\varepsilon_{v,cy}$ is volumetric strain. This equation proposed by Banzibaganye et al.(2020) is for sands of similar characteristics to their material with rubber chips up to 30 % and confining stress up to 100 kPa. The rubber chips used were 4mm to 12mm in size, which is similar to the gradation of gravel used in this study. As shown in Figure 2.21, the rate of pore pressure is greater compared to that of fine sands defined by Chen et al. (2019). In other words, for the same volumetric strain the sand with rubber chips had a higher R_u compared to the fine sand. This could be attributed to the inclusion of rubber chips. Considering the gravel content of this study is of similar gradation of the rubber chips, the general trend in the shift of R_u response with volumetric strain is similar. However, the gravelly soil in this study has an even greater increase in the rate of R_u as volumetric strain increases. A possible explanation of this could be the further increase in gravel size particle (49%).
It can be noticed that for the relationships defined by Banzibaganye et al. (2020) and Chen et al. (2019), the pore water pressure ratio continues to increase above 1.0 at volumetric strains of about 1.5% and 2.5% respectively. The correlations established for the gravelly soils tested in this study do not reach R_u of 1.0 for the volumetric strain of interest (0-3%). The R_u predictions at higher volumetric strains with the model proposed in this study become constant with large increases in volumetric strain and the trend does not sharply surpass R_u 1.0. It must be noted that the data produced in this study is not available for lower volumetric strains (less than ~ 0.1% for dense and 0.2% for medium dense) and higher volumetric strains (more than ~ 1.0% for dense and 1.7% for medium

dense). Nevertheless, findings in this study are deemed useful for improving understanding of cyclic behaviors of gravelly soils where lack of data is available.

CHAPTER 3

CENTRIFUGE MODELING

3.1 Introduction

Centrifuge modeling is a laboratory method that applies a gravitational acceleration greater than earth's gravity to a soil model to better simulate stress conditions in the field. The model spins in the centrifuge and is subjected to this higher gravitational field by the produced centrifugal force. This allows for geostatic stress conditions to be applied to the soil model, which are more representative of soil conditions in the field. Additionally, free drainage at the surface of the centrifuge model creates a partial drainage condition. This is more typical of the condition found in the field in comparison to fully undrained or drained conditions in triaxial element tests. In this study, the objective of centrifuge tests was to simulate more realistic conditions to provide a comparison to the ideal conditions simulated in the triaxial equipment. Specifically, the impact of partial drainage condition on the relationship of excess pore water pressure and volumetric strain was of interest.

3.2 Testing Program and Methodology

3.2.1 Testing program

A picture of the centrifuge equipment used for testing can be seen in Figure 3.2. The centrifuge model aims to simulate a level free draining surface soil profile of

approximately 6 m under a surcharge load. The effective stress at the middle of the model is approximately 140 kPa. A layer of lead shot placed on the soil surface is used as a surcharge load and assumed to uniformly distribute with depth. This method has been used in other centrifuge studies (Ni et al., 2020). The same gravelly soil material as described in Section 2.2 was used for the purpose of comparison with the triaxial tests. Two centrifuge models were constructed with relative densities representative of dense (70.2 %) and loose (30.7 %) conditions. The model representative of loose conditions was tested first and is referred to as Cent1_L. The dense model is referred to as Cent2_D. Both models were consolidated to 50g and subjected to two 1-Hz sinusoidal motions applied to the base shaker; Shake Event 1 and Shake Event 2. Shake Event 1 applied a low base amplitude 0.015g for 5 cycles for the purpose of observing the dynamic behavior for a non-destructive event. Next, a base motion of 0.4g was applied for 40 cycles, referred to as Shake Event 2. The models were arrayed with accelerometers, pore pressure transducers, and linear variable differential transformers (LVDT) to assess dynamic behavior. Arrangement of all sensor locations is detailed in Figure 3.1, placed in 4 layers. Each layer surface was scratched during construction to ensure interlocking and form a complete uniform soil model.

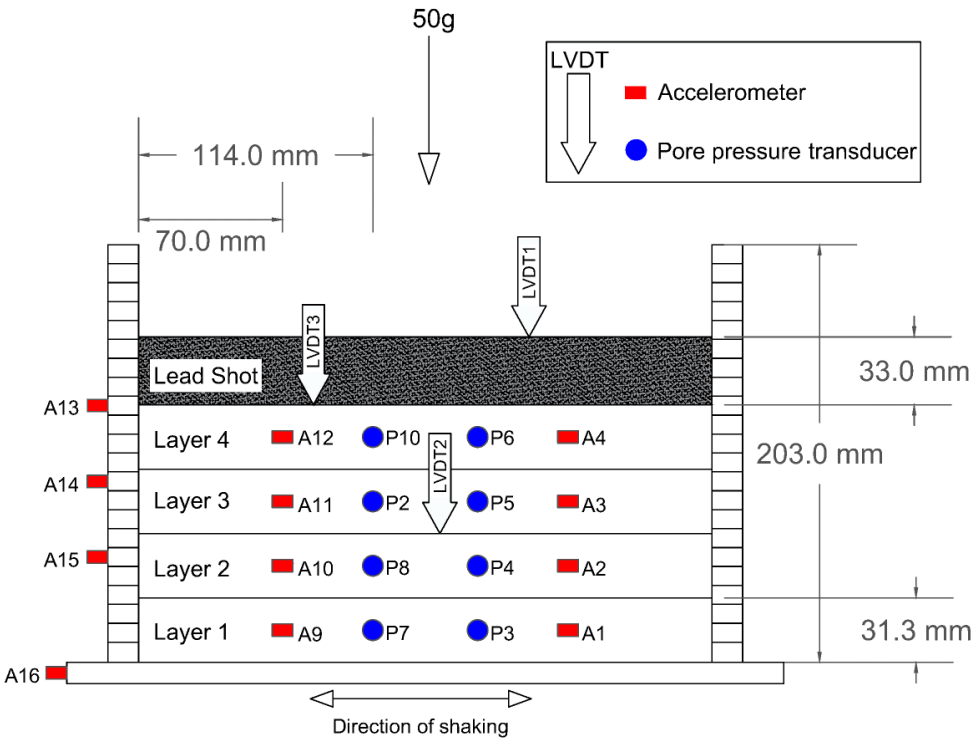

Figure 3.1 Sensor array.

Figure 3.2 Pictures of centrifuge equipment, arm, and laminar box.

3.2.2 Methodology

The models were prepared in a laminar box with mode scale dimensions of 203 mm (width) x 279 mm (length) x 203 mm (height). In preparation for the centrifuge test, a membrane was constructed with rubber membrane material and Barge All Purpose Cement glue. This process was done a week prior to test day to ensure all glue was dry. Due to the dynamic time scale, a viscous fluid of 50 mPa-s was prepared with the surface hydration method of methylcellulose (HPMC) with deaired water. This corresponds to a centrifugal acceleration of 50g. In preparation for model construction, soil was prepared in 8 pans and mixed with 7% (by weight) viscous fluid. The soil was left overnight to ensure uniformity of moisture content. Figure 3.3 displays the process of membrane construction and preparation for model construction. As shown, the membrane was placed in the laminar box, then surrounded by a saturation box for stabilization during construction and later saturation. A vacuum method was used to fully fit the membrane to the box prior to model construction. The model was constructed in 4 layers by the moist tamping method. Within each layer, pore water pressure sensors and accelerometers were placed strategically as seen in Figure 3.4. After the model construction was completed with target densities and sensor arrays, the model was flushed with CO_2 and saturated with the viscous fluid using the dual vacuum method shown in Figure 3.5. Once full saturation was complete, the leadshot layer was used as surcharge load to increase the effective confinement (Ni et al., 2020). A geotextile material was cut to cover the entire soil surface and walls of the box to ensure the leadshot would not mix with the model. Two holes were cut in the geotextile to allow LVDT 2 and 3 to move without restraint. These holes also needed to be small enough to ensure no lead shot went into the soil

model. Once the geotextile was put into place, the lead shot was added slowly to reduce the amount of pore water pressure buildup and not preload the soil. This process is shown in Figure 3.6. The leadshot surface was then leveled and LVDT 1 was placed. At this point model construction was complete and the soil model was placed in the centrifuge on the shaker. Sensors were connected, organized, and fastened securely on the centrifuge arm as shown in Figure 3.7. Lastly the centrifuge arms were balanced, and the floor of the centrifuge was cleaned.

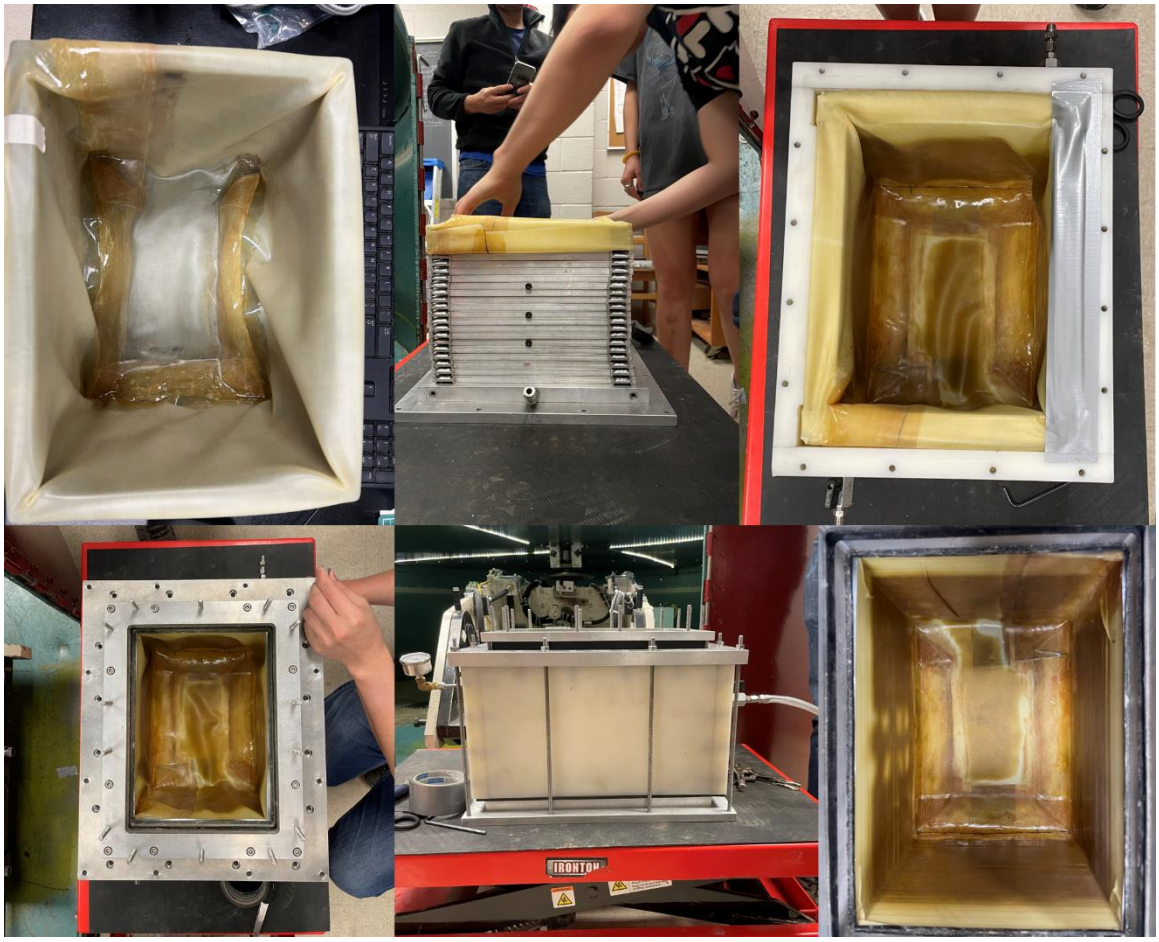

Figure 3.3 Membrane construction and fitting in preparation for model construction.

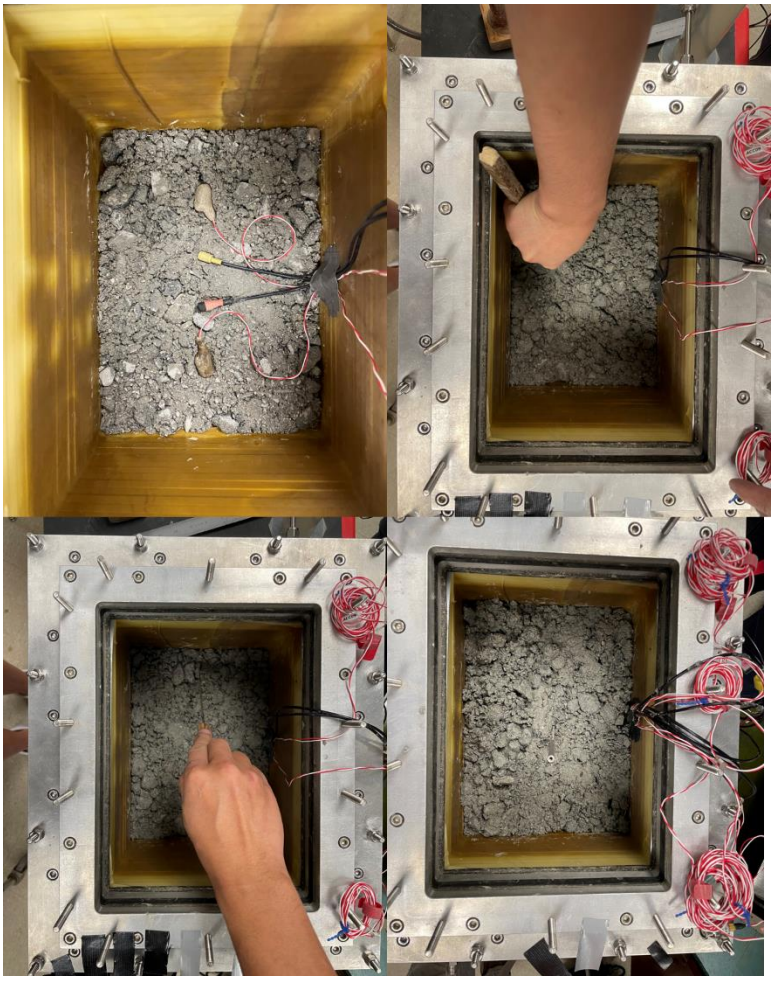

Figure 3.4 Model construction including sensor array within layer.

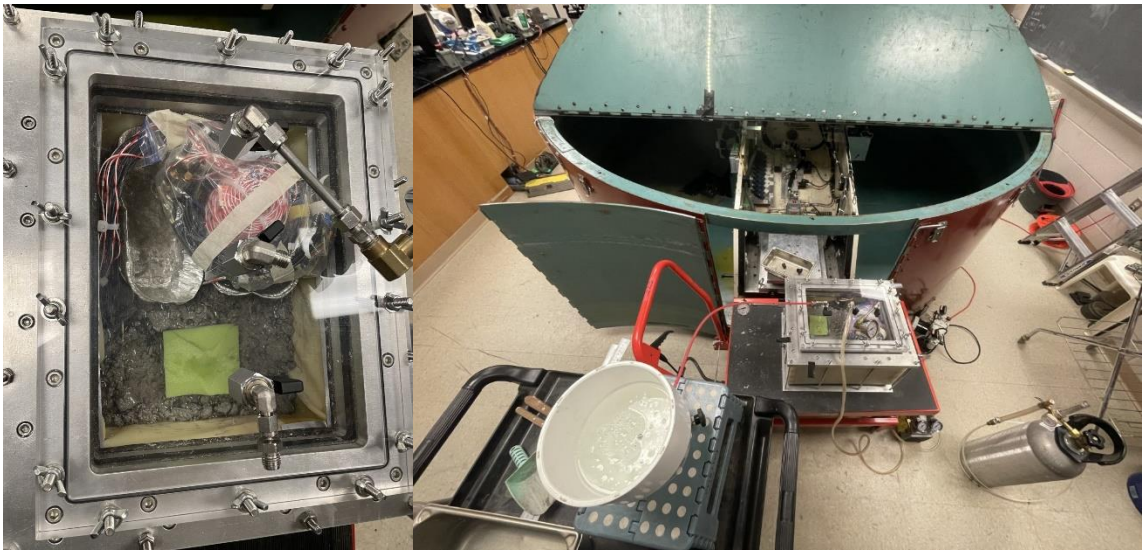

Figure 3.5 Saturation Process

Figure 3.6 Geotextile and leadshot placement.

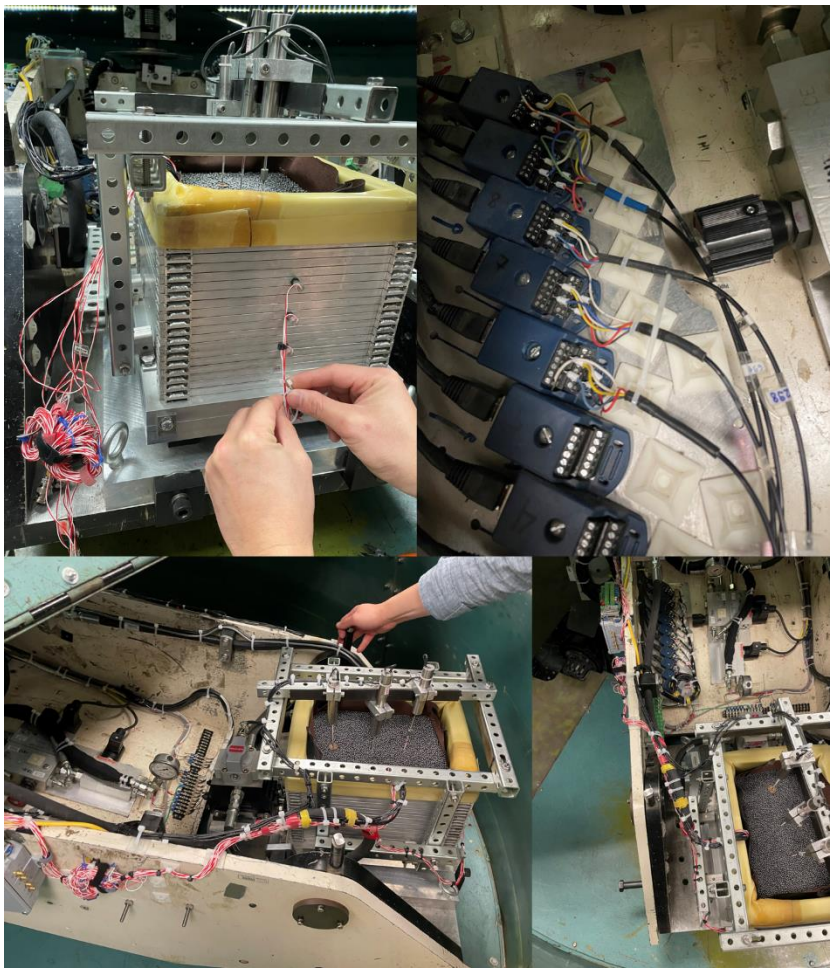

Figure 3.7 Fastening of sensors to centrifuge arm.

The models were spun up to 50 g for complete consolidation. The LVDT data provided the post-consolidation volume of the models. The shaker is powered by hydraulic pressure which was started in preparation for shaking. Prior to shaking the DAQ system was set to logging data of 2000 samples/sec. A 1-Hz uniform sinusoidal motion was applied to the base shaker for two different shaking amplitudes. First a low amplitude of 0.015g was applied for 5 shaking cycles. After allowing time for pore water dissipation, a second shaking motion of 0.4g was applied for 40 shaking cycles. The maximum and average base shaking amplitudes applied to each model for both events are detailed in the following section. After both shake events were applied to the model, time

for pore water dissipation was allowed before the centrifuge was spun down to 1g. After the spin down was complete, a visual investigation was performed including the measurement of the lateral displacement of each stack of the laminar box and the measurement of the soil surface for 9 locations across the surface. The new soil layer heights were approximated by averaging the post-test soil model. Each layer was then taken out slowly layer by layer and vertical and horizontal displacement of the sensors within each layer were recorded. The visual assessment of post-test sensor locations was compared to LVDT data which agreed well for both models. A wet sieve and dry sieve were completed (using #4, #40, and #200) to assess post-test grain size distributions.

3.3 General Results

3.3.1 Post-consolidation

The models were spun up at rate of 4g per minute until 50g was achieved. LVDT data was monitored to obtain consolidation information for both models. The preparation relative density and consolidation results are displayed in Table 3.1. Generally, consolidation at 50g for the loose model resulted in an increase in relative density of 4% for the entire soil model. Using LVDT data to split the models into two halves, the relative density of the top and bottom half of the loose soil model increased 10% and decreased 2%, respectively. For the dense model, there was a different trend. Spinning up to 50g caused a slight dilation of nearly 2% for the entire soil model. Analysis of the two halves of the model shows that the bottom half of the model experienced 7% decrease in D_R compared to about a 5% increase in the top half. It can be noted that in both models (loose and dense), the top half of the soil exhibited contractive behavior during consolidation and the bottom half of the soil exhibited dilative behavior. This dilative

behavior was much more pronounced in the dense model and caused the new D_R representative of the entire soil model to be overall minorly dilative (2%).

Table 3.1 Summary of preparation and post consolidation relative density.

Parameter	Cent1_L	Cent2_D
Max Density (kN/m3)	22.53	22.53
Min Density (kN/m3)	18.69	18.69
*Dry Unit Weight (kN/m3)	19.72	21.23
*Water content, (%)	7	7
Assumed Gs	2.7	2.7
*D_R, (%)	30.7 %	70.2 %
Entire Soil Model $D_{R,conso.}$, (%)	35 %	69 %
Bottom Half $D_{R,conso.}$, (%)	29 %	63 %
Top Half $D_{R,conso.}$, (%)	41 %	75 %

*refers to initial soil condition used in preparation

3.3.2 Shaking time histories

Two different shaking events were applied to the centrifuge models. This consisted of 0.015g and 0.4g low and high shaking amplitudes, respectively. The purpose of the low amplitude shaking event was to analyze the soil response to a non-destructive dynamic load. The peak and average amplitudes for both events observed at the base of the models can be found in Table 3.2. The loose and dense models have agreeable average amplitudes for both shaking events.

Table 3.2 Peak and average base amplitudes observed in Cent1_L and Cent2_D.

	Cent1_L		**Cent2_D**	
	Peak*	Average*	Peak*	Average*
Shake Event 1 (0.015g)	0.018	0.014	0.025	0.018
Shake Event 2 (0.4g)	0.40	0.38	0.41	0.38

*estimated by accelerometer located at the base (A16)

As mentioned, the two soil models were subjected to an initial low amplitude shaking event of 0.015g (referred to as Shake Event 1) for 5 cycles. Acceleration time histories for both models are shown in Figure 3.8 for each layer with depth reported in prototype scale. Both models followed the same general trends for this shaking amplitude and did not have pore water pressure buildup (see Figure 3.9) or settlement. At shallower depths, the amplitude increased slightly and had more uniform peaks of cyclic loading in both models. The dense model (Cent2_D) has slightly more amplification of the base amplitude compared to the loose model. This can be seen in Figure 3.8 as Cent2_D has a 0.01g amplification of the base amplitude in the shallowest layer compared to just 0.003g of Cent1_L. Following the low shaking amplitude, a high shaking amplitude of 0.40g (referred to as Shake Event 2) was applied to the base shaker for 40 cycles. The acceleration time histories of Shake Event 2 are shown in Figure 3.10 for both models. The base amplitude of Shake Event 2 remains fairly uniform throughout the first 20 cycles, followed by a slight decrease that becomes greater in the last 5 cycles (~ 0.35g) in both models. In general, de-amplification occurs as the wave propagates to the shallower soil depths. Detailed in Figure 3.10, this de-amplification is more prominent in Cent1_L (0.08g) compared to Cent2_D (0.05g).

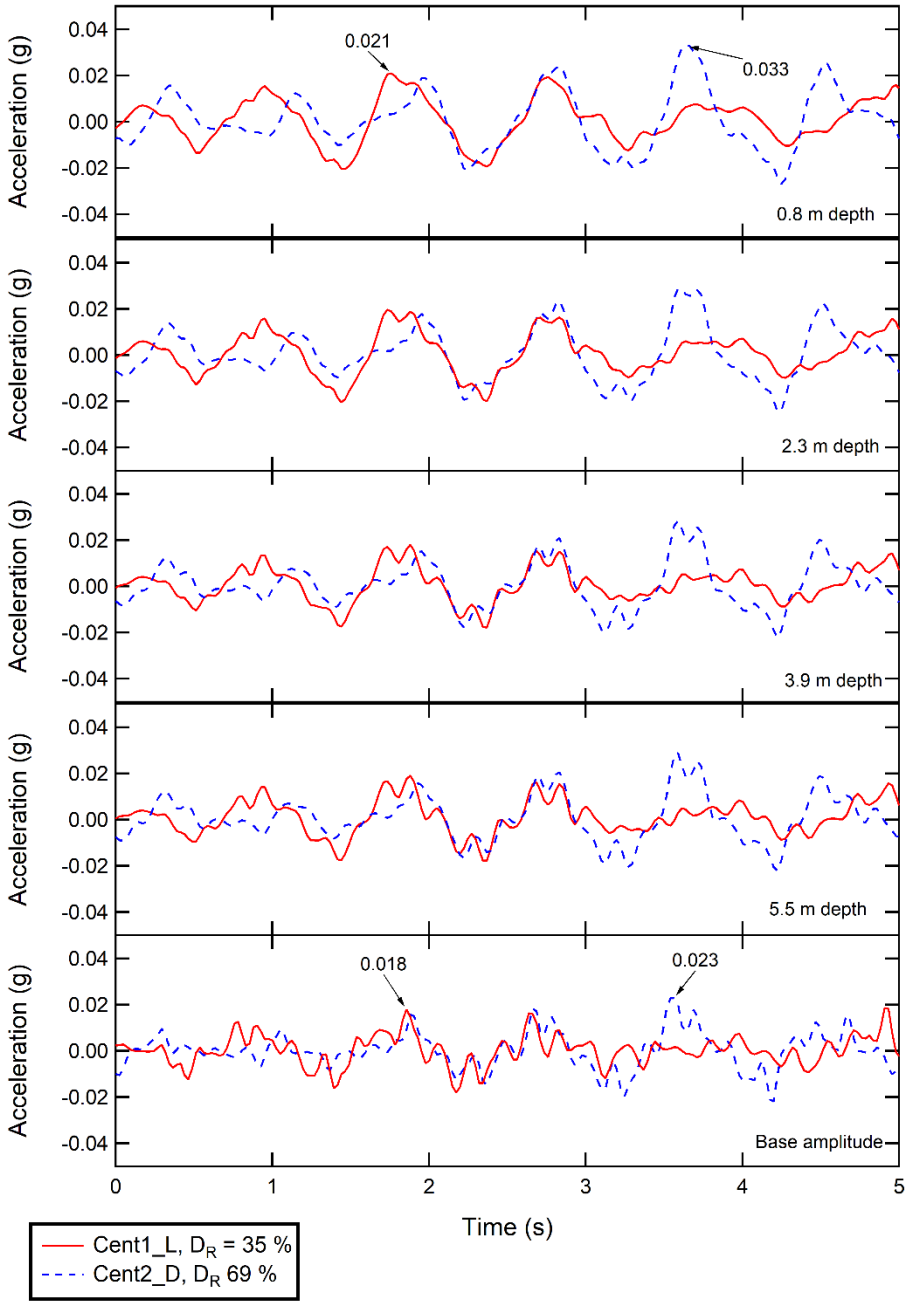

Figure 3.8 Acceleration time histories for Shake Event 1 (0.015g).

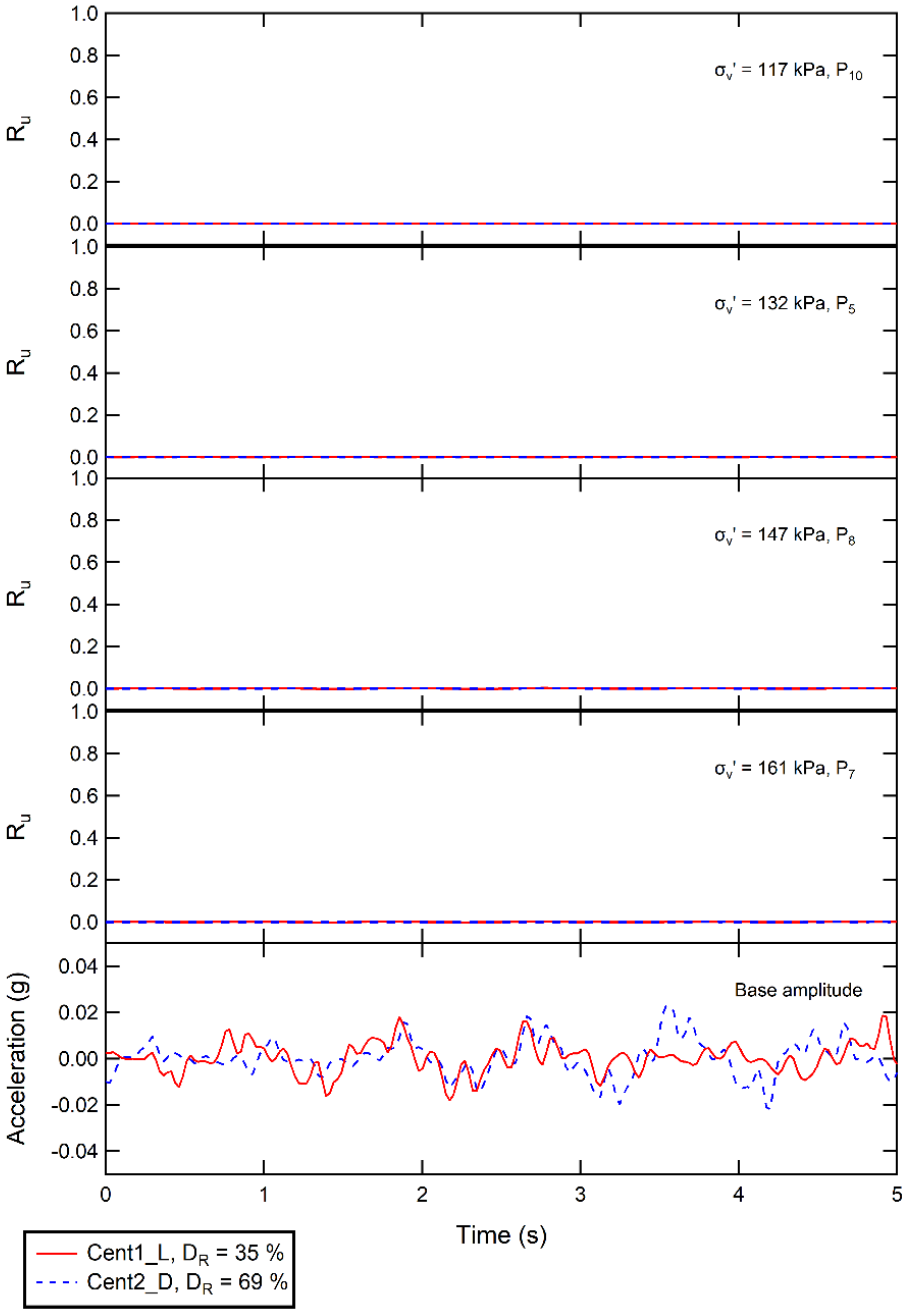

Figure 3.9 Pore water pressure time histories for Shake Event 1 (0.015g).

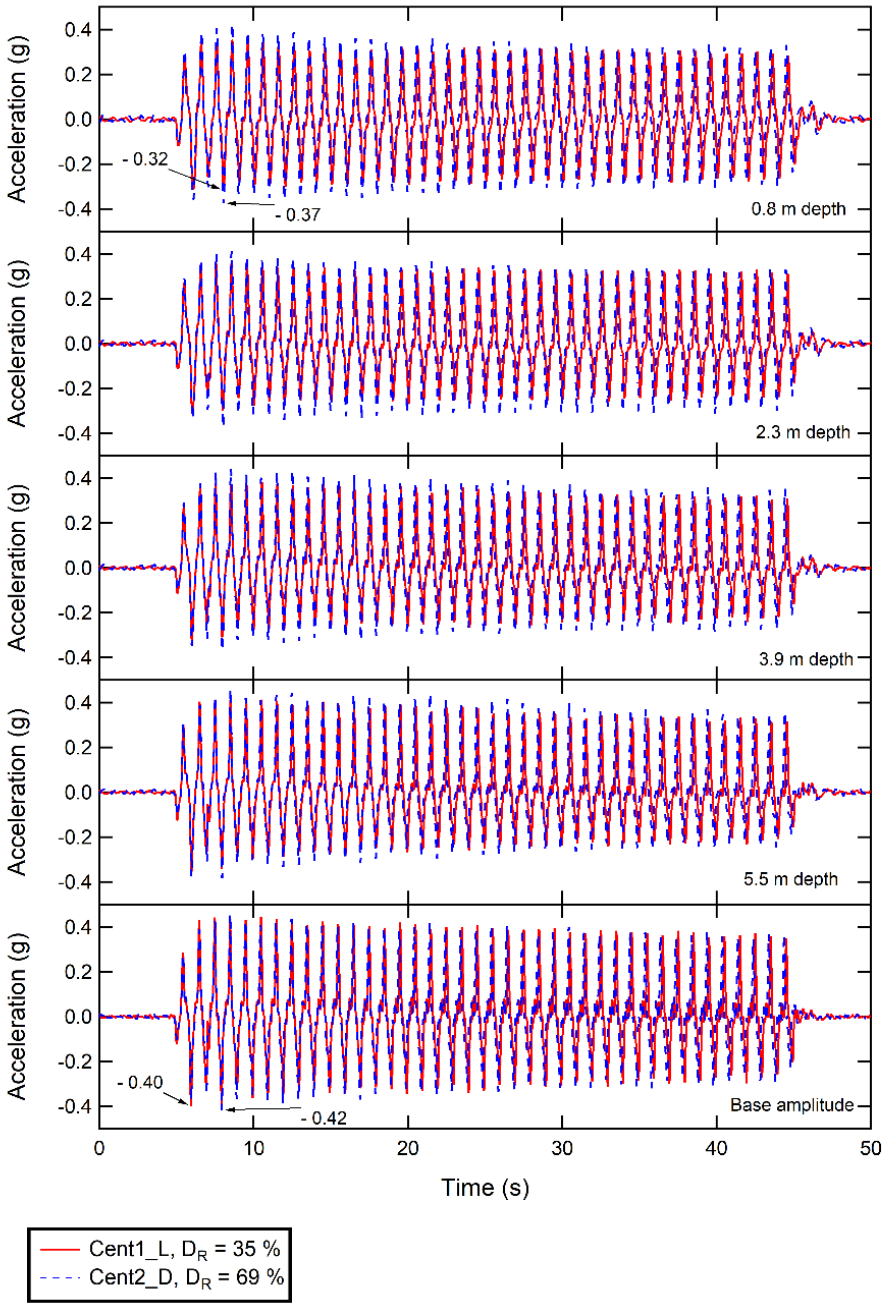

Figure 3.10 Acceleration time histories for Shake Event 2 (0.4g).

Figure 3.11 (a) and (b) show the excess pore water pressure at different increments of time during shaking with soil profile depths for Cent1_L and Cent2_D, respectively. Development of excess pore pressures is represented by solid lines and

dissipation of excess pore pressures is represented by dashed lines. The figure highlights that there was upward flow in the shallower depths of both soil models during both excess pore water development and dissipation. At deeper depths greater than 4m (prototype scale), there was very little flow during the development and dissipation of excess pore water pressures. However, there was an impact of relative density on flow at depths greater than 2m. During dissipation, Figure 3.11 (a) shows that Cent1_L had an upward flow throughout the entire soil model. Comparatively, Cent2_D had slight downward flow at the middle of the model during dissipation. This is displayed in Figure 3.11 (b) as Cent2_D had an increase of pore water at the bottom of the model from 39.5 seconds to 40 seconds due to the downward flow. At the end of shaking (40 seconds), both models had excess pore water pressures that did not fully dissipate. Due to the continuous upward flow of dissipation in Cent1_L, the loose model had less excess pore pressures at each depth compared to Cent2_D at the end of shaking. The greatest excess pore pressures at the end of shaking were at the bottom of both models with 20 kPa in Cent1_L compared to 40 kPa in Cent2_D.

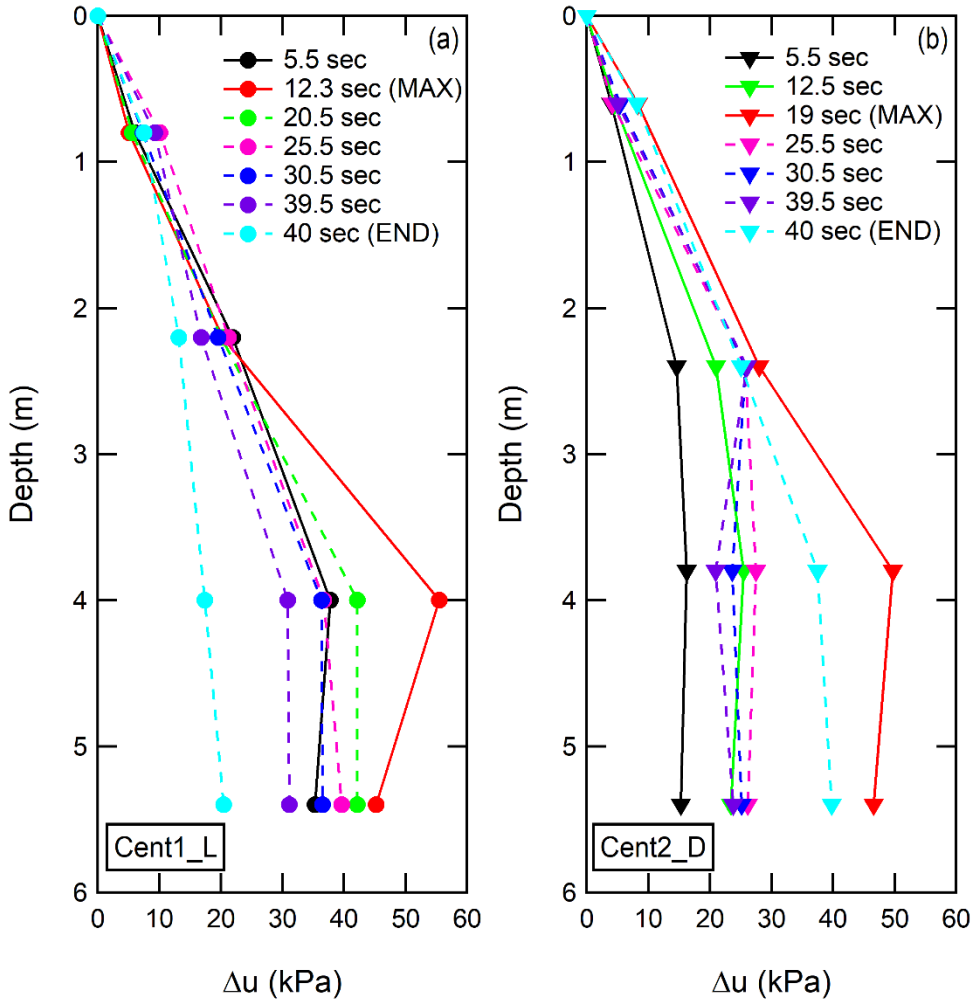

Figure 3.11 Excess pore water pressure during shaking for: (a) Cent1_L, and (b) Cent2_D.

3.4 Data Analysis & Results

The following sections describe the procedures in which the data was analyzed and displays results of pore water pressure, volumetric strain, shear strain, and CSR for Shake Event 2 of both models. Appendix A includes this data plot with the number of cycle for each layer in the model.

3.4.1 Volume change and volumetric strain

As detailed in the methodology, model instrumentation included 3 LVDT's placed at: the lead shot surface, soil surface, and halfway into the soil model (refer to Figure 3.1). The LVDT data provides settlement in real time throughout each stage of the test. It is reported as a positively increasing value as the soil contracts. Manual measurements of settlements were completed post-test near the LVDT sensor locations to validate the data. These values agreed within 1mm. This small deviation is most likely due to manual measurements taken most nearly to the LVDT sensor locations (not at the exact location). The discrepancy between these values can also be attributed to the spin down process. Settlement measurements were used to calculate the void ratio and changes in volumetric strain for each stage of the test (i.e., initial 1g, consolidation to 50g, Shake Event 1 - 0.015g, Shake Event 2 - 0.4g, post shake dissipation, and spin down). The volume post-consolidation was taken as the new initial volume for the calculation of volumetric strain due to cyclic loading. The void ratio was calculated by equation:

$$e = (G_s * \gamma_w/\gamma_d) - 1$$

Eq. 3.1

where e is void ratio; G_s is specific gravity, γ_w is the unit weight of water; and γ_d is the dry unit weight of soil.

LVDT2, located halfway into the soil model, allows for a separate analysis for both the bottom half and top half of the model. It is assumed that the initial conditions of each half are the same in height, density, and void ratio. This is reasonable because the target densities were achieved for each layer during model construction. To obtain

settlement of solely the top half of the soil, the settlement recorded at the middle of soil model was subtracted from the settlement recorded at the soil surface. The volumetric strains for the top and bottom halves represent the change in volume within that half of the model with respect to half of the soil model's height.

Void ratio and volumetric strain (ε_v) for the entire, top half, and bottom half of both soil models in each stage of the test are displayed in Table 3.3. The values of ε_v are representative of strain that occurred within that stage (dilation denoted by negative ε_v). In general, Cent1_L experienced greater settlement compared to Cent2_D. During consolidation, the top half of both models contracted. However, the bottom half of both models dilated. This dilative behavior was greater in Cent2_D, which resulted in an overall dilation of the entire soil model during consolidation. During Shake Event 1, there was negligible change in void ratio and volumetric strain. Even so, Cent2_D had slightly dilative behavior compared to slightly contractive behavior in Cent1_L. Shake Event 2 resulted in overall contraction in the top and bottom of both models. In Cent1_L, this event resulted in 1% more volumetric strain in the top half of soil compared to the bottom. The top half of Cent2_D had more than 2% volumetric strain compared to the bottom. For the "Entire Soil Model", Cent1_L had nearly 1% more volumetric strain due to the 0.4g shake event compared to Cent2_D.

Table 3.3 Void ratio and volumetric strain throughout test in the entire, top, and bottom of soil models.

Stage of Test	Entire Soil Model		Top Half Soil Model		Bottom Half Soil Model	
	Void Ratio	ε_v (%) **Within Stage**	**Void Ratio**	ε_v (%) **Within Stage**	**Void Ratio**	ε_v (%) **Within Stage**
			Cent1_L			
1g Initial Condition	0.368	-	0.368	-	0.368	-
50 g	0.358	0.726	0.342	1.84	0.373	- 0.391
Shake Event 1 (0.015g)	0.358	0.002	0.342	0.042	0.373	- 0.038
Shake Event 2 (0.4g)	0.314	3.21	0.290	3.88	0.338	2.56
Post 0.4g Shake Dissipation	0.314	0.005	0.292	- 0.18	0.336	0.19
			Cent2_D			
1g Initial Condition	0.270	-	0.270	-	0.270	-
50 g	0.273	- 0.23	0.258	0.93	0.288	- 1.39
Shake Event 1 (0.015g)	0.273	- 0.02	0.259	- 0.03	0.288	- 0.01
Shake Event 2 (0.4g)	0.244	2.30	0.217	3.34	0.271	1.29
Post 0.4g Shake Dissipation	0.244	0.008	0.216	0.048	0.272	- 0.03

*negative represents dilation

It is important to note that the majority of volumetric strain occurred during shaking, as there is little during post shake dissipation. This observed behavior in both models is displayed in Figure 3.12. Figure 3.12 (a) shows the settlement (prototype scale) of the soil surface (LVDT 3) and middle of the soil model (LVDT 2) with time for Shake Event 2. It is noted that there is a removal of data at the start of shaking for Cent1_L due to a large jump in settlement from LVDT noise. Following cyclic loading, the settlement of the model was monitored as excess pore pressures dissipated, shown in Figure 3.12

(b). As shown, practically no settlement occurred in either model following dynamic loading. This is contrary to what has been found in sand, which continues to undergo volumetric strain after undergoing cyclic loading. Darby et al. (2019) performed centrifuge tests under the partial drainage condition on saturated sands and found that the majority of volumetric strain occurred after shaking stopped.

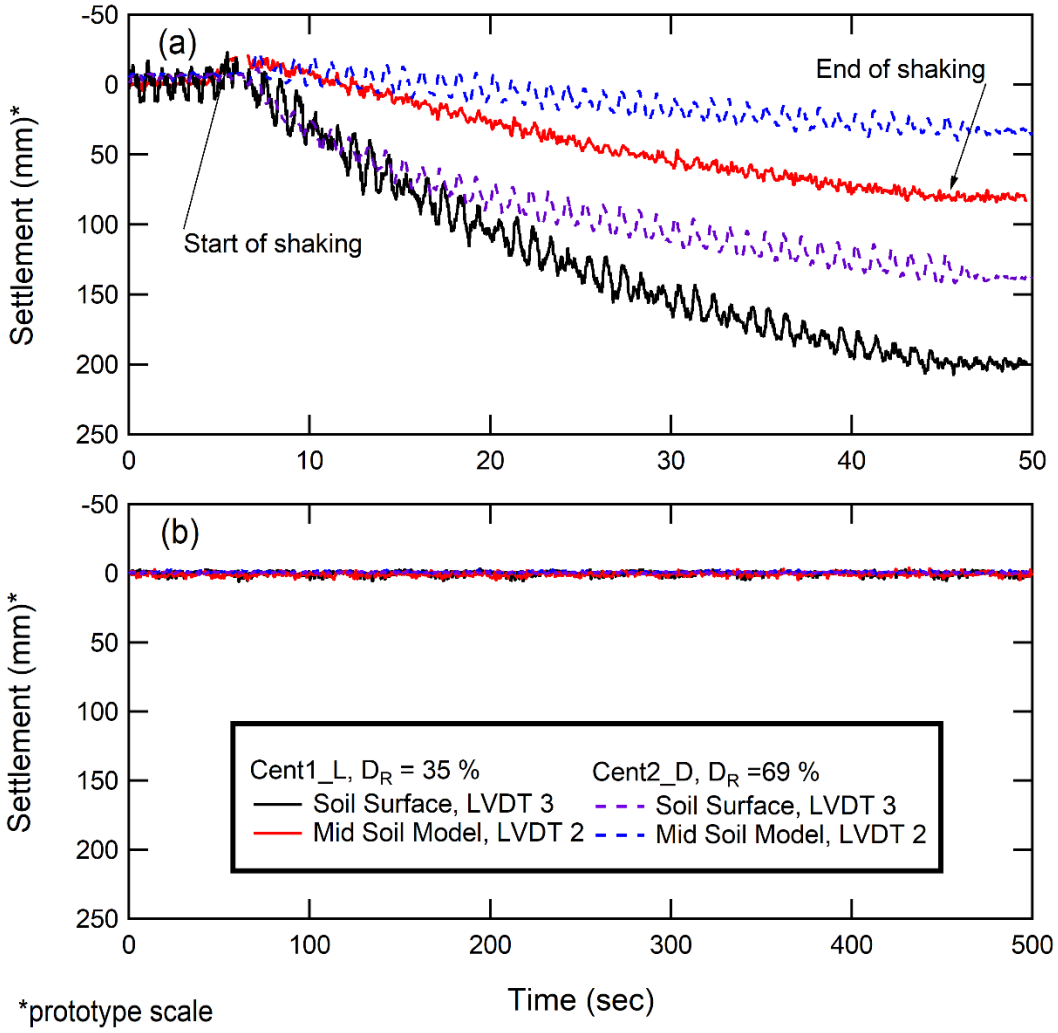

Figure 3.12 Settlement with time for Cent1_L and Cent2_D during: (a) Shake Event 2, and (b) Post Shake Event 2 Dissipation.

Shear stress

Shear stress was calculated by the Elgamal and Zeghal (1992) method. Due to the absence of accelerometers instrumented in the lead shot of the model, the acceleration was assumed to be equal to that of the first soil layer. The shear stress is calculated within each layer by using an average of the accelerometers within the respective layer and the layer above it:

$$\tau_{l=i} = \tau_{l=i+1} + \Delta\tau$$

Eq. 3.2

where $\tau_{l=i}$ is shear stress in layer *i;* $\tau_{l=i+1}$ is shear stress in the layer above layer *i* (aka. layer *i+1*); and $\Delta\tau$ is the change in shear stress between layer *i* and layer *i+1*. The equation for $\Delta\tau$ is:

$$\Delta\tau = \frac{1}{2}(\rho_{soil} * (z_{l=i+1} - z_{l=i})(a_{l=i+1} + a_{l=i})$$

Eq. 3.3

where ρ_{soil} is soil density; $z_{l=i+1}$ is the depth of accelerometer in layer *i+1*; $z_{l=i}$ is the depth of accelerometer in layer *i*; $a_{l=i+1}$ is the absolute horizontal acceleration in layer *i+1*; and $a_{l=i}$ is the absolute horizontal acceleration in layer *i*.

Since the top layer is the shallowest layer with sensor implementation and therefore has no $\Delta\tau$, it can be calculated as:

$$\tau_{l=4} = \frac{1}{2}(\rho_{leadshot} * z_{leadshot} + \rho_{soil} * z_{l=4})(a_g + a_{l=4})$$

Eq. 3.4

where $\tau_{l=4}$ is the shear stress in layer 4; $\rho_{leadshot}$ is lead shot material density; ρ_{soil} is soil density; $z_{leadshot}$ is the depth of lead shot; $z_{l=4}$ is the depth of accelerometer in layer

4; a_g is the absolute horizontal acceleration at ground surface (assumed equal to layer 4); and $a_{l=4}$ is the absolute horizontal acceleration in layer 4.

Shear strain

The shear strain is determined by double integration of the acceleration histories to obtain displacement. The program Seismosignal was used to perform this double integration. The shear strain for each layer in the model is calculated by the accelerometers located on the outside of the laminar container (positioned within the depth of each respective soil layer) and the accelerometer at the base of the shaker. It can be noted that Layer 1 does not have an accelerometer outside the box and therefore an accelerometer within the soil model was used. The equation is:

$$\gamma_{l=i} = \frac{d_{l=i} - d_b}{h}$$

Eq. 3.5

where $\gamma_{l=i}$ is shear strain in layer *i*; $d_{l=i}$ is the displacement in layer *i*; d_b is the displacement at the base; and *h* is the difference between depth at base and depth of sensor in layer *i*.

3.4.2 Cyclic shear stress – strain relationship

This section displays the results of CSR and shear strain for Shake Event 2 of both models. The stress-strain relationship for both models is shown in Figure 3.13. In both models, CSR is generally the same in the first 3 deeper layers and decreases slightly by the shallowest layer. This is to be expected due to geostatic stress and wave propagation. Wave propagation is affected by the shear modulus, or stiffness, of the soil. As confinement increases, the shear modulus of the soil increases as it experiences greater effective stresses. Therefore, the shallower layers with lower confinement have a

reduction in the propagation velocity. The varying shear modulus throughout the soil model causes the acceleration to de-amplify and the CSR to slightly differ within each layer. In Cent1_L, the CSR decreases from 0.39 to 0.35. In Cent2_D, the CSR decreases from 0.44 to 0.39. The same trend also applies to the shear strain. In general, as confinement decreased, both CSR and shear strain decreased. Figure 3.13 (d) displays large shear strain for both models compared to Figure 3.13 (a). The shear strain amplitude of the two models were very similar, however the dense model experienced less shear strain. The positive shear strain during shaking ranged from 1.7% to 2.7% for Cent1_L compared to 1.4% to 2.3% for Cent2_D. During shear reversal, negative shear strains ranged from -1.6% to -2.5% for Cent1_L and -1.3% to -1.9% for Cent2_D.

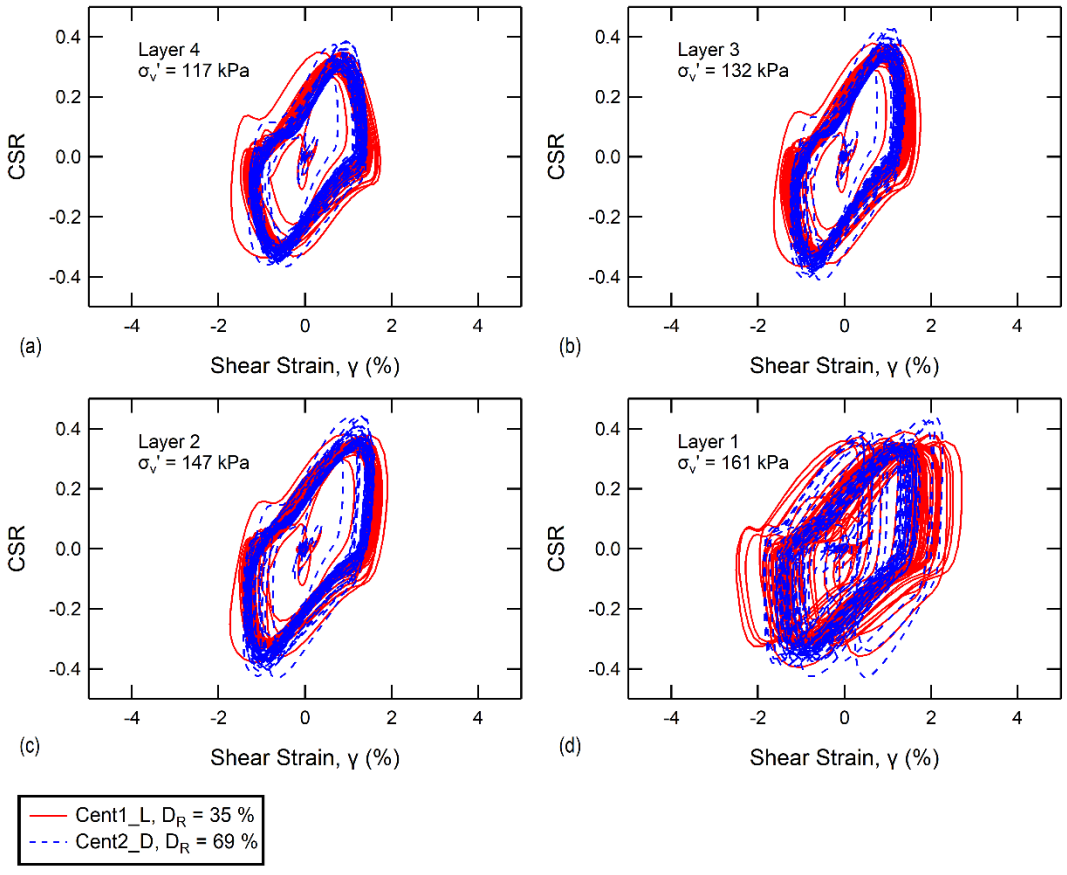

Figure 3.13 Comparison of shear stress response to Shake Event 2 (0.4g) for effective stresses: (a) 117 kPa, (b) 132 kPa, (c) 147 kPa, and (d) 161 kPa.

3.4.3 Pore pressure and cyclic shear strain

Pore water pressure generation and cyclic shear strain with loading cycle for both soil models are displayed in Figure 3.14. This R_u was taken as the maximum R_u over the respective cycle. The cyclic shear strain is an average of the positive and negative shear strain experienced over the respective cycle. As previously noted, R_u is the greatest in the second layer which peaks and gradually decreases in both models. R_u is lowest in the shallower layers that do not exhibit a peak in the relationship with cycle number. As shown in Figure 3.14 (a), Cent1_L has a faster buildup of pore water pressure and a higher peak of R_u 0.38 at cycle 12 in Layer 2. Pore water dissipation after this peak is evident, as R_u reduces to 0.23 by cycle number 40. Cent2_D has a later maximum of R_u in each layer and a slower rate of pore water dissipation. Detailed in Figure 3.14 (b), the maximum R_u occurs in Layer 2 at cycle 19, R_u 0.34. At cycle 40, the R_u reduced to 0.26. Cent2_D had overall less pore water pressure buildup, however the R_u is higher at the end of cyclic loading compared to Cent1_L. Therefore, the dense model did not dissipate as much as the loose model. The permeability of the dense model is less than the loose model as there is less void space in the soil to allow water to flow. This is likely the reason for the slower buildup (later peak in R_u) and dissipation rate of pore water pressure in the dense model. Also shown in Figure 3.14, the highest cyclic shear strain occurred in deeper layers. Figure 3.14 (a) shows a clearer trend in effect of confinement on cyclic shear strain for Cent1_L. In general, as confinement decreases, as does cyclic shear strain. This trend is not true for Cent2_D, shown in Figure 3.14 (b). The lowest cyclic shear strain occurred in layer 3, and the highest in layer 2 until after cycle 20. The difference in cyclic shear strains for varying confinement is never greater than ~ 0.6%.

The largest difference in cyclic shear strain between layers in Cent1_L was 0.58% compared to 0.36% in Cent2_D. This implies that confinement has a greater effect on cyclic shear strain for lower relative densities. Both models have a similar trend in the relationship of cyclic shear strain with loading cycle. The cyclic shear strain varies with each loading cycle but follows a general increasing trend initially. After cycles 11 (Cent1_L) and 18 (Cent2_D), which correlates closely to the maximum R_u, the cyclic shear strain begins to follow a decreasing trend with increasing loading cycles. This, however, is not true for the deepest layer, which continues to increase in cyclic shear strain for the remainder of loading. Both trends are more prominent in Cent1_L than Cent2_D.

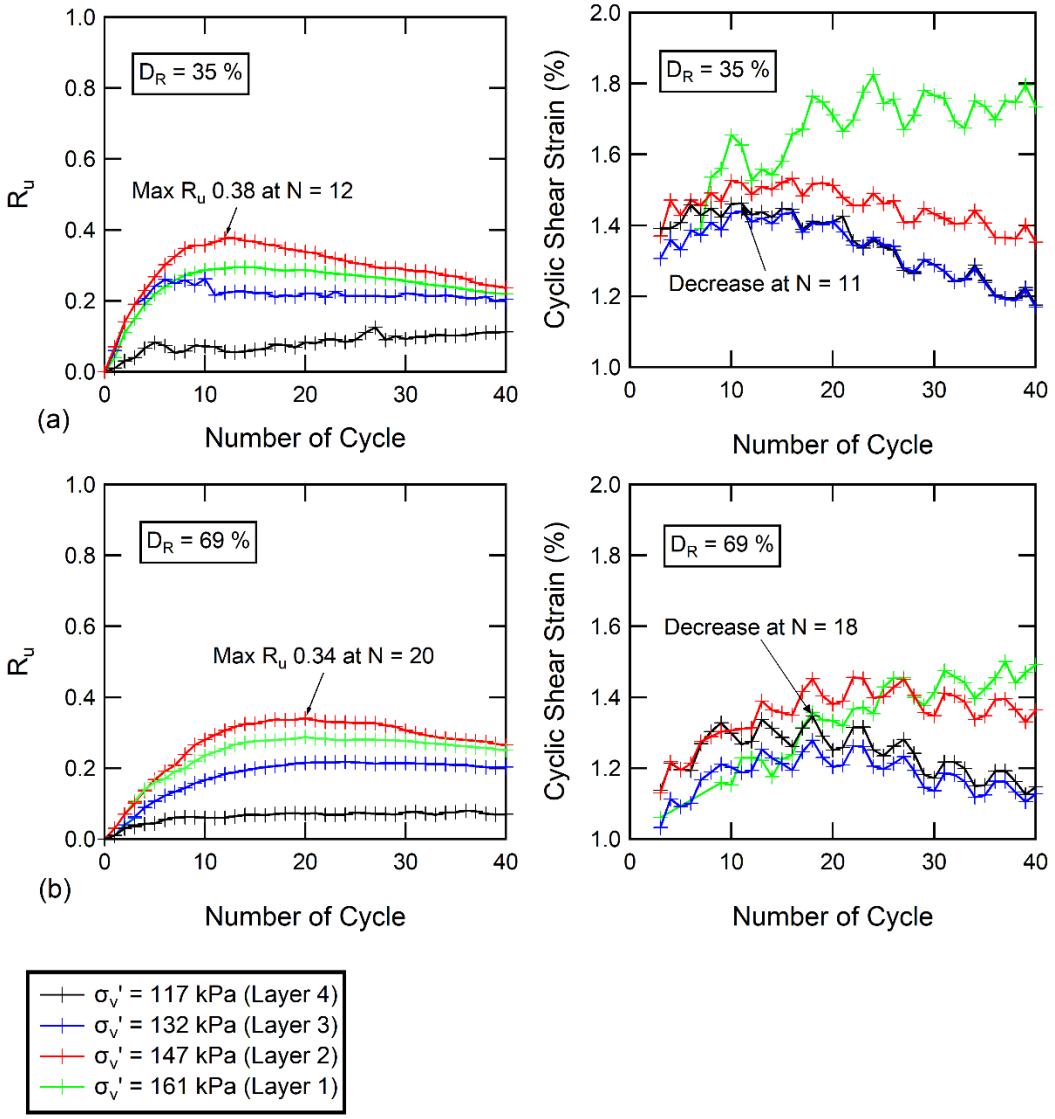

Figure 3.14 Excess pore pressure and cyclic shear strain development with increasing cycle number for Shake Event 2 (0.4g): (a) Cent1_L, and (b) Cent2_D.

The relationship of pore water pressure development with cyclic shear strain is displayed in Figure 3.15. Cyclic shear strain from Shake Event 1 is included to provide a greater understanding of the relationship since there was no development of R_u in this shake event. The cyclic shear strains corresponding to no excess pore pressure ranged 0.048 – 0.114 % and 0.043 – 0.122 % for Cent1_L and Cent2_D, respectively. This implies that the threshold cyclic shear strain for the gravelly soil in this study is possibly

0.1% or more. In Cent1_L the cyclic shear strain ranged from 1.2 – 1.5 %, 1.2 – 1.4 %, 1.4 – 1.5 %, and 1.4 – 1.8 % for Layers 4, 3, 2, and 1, respectively. Cent2_D had cyclic shear strains ranging from 1.1 – 1.3 %, 1.0 – 1.3 %, 1.1 – 1.5 %, and 1.1 – 1.5% for Layers 4, 3, 2, and 1, respectively. This implies that it is expected to have lower cyclic shear strains for high relative density compared to low relative density, but that the range at different confinements remain about the same. Also, as confinement increases, there is a greater range in the cyclic shear strains. Overall, the relationship between R_u and cyclic shear strain is similar for the two relative densities. In general, the pore water pressure was higher in the layers with greater cyclic shear strain. This corresponds to the layers of greater confinement as well.

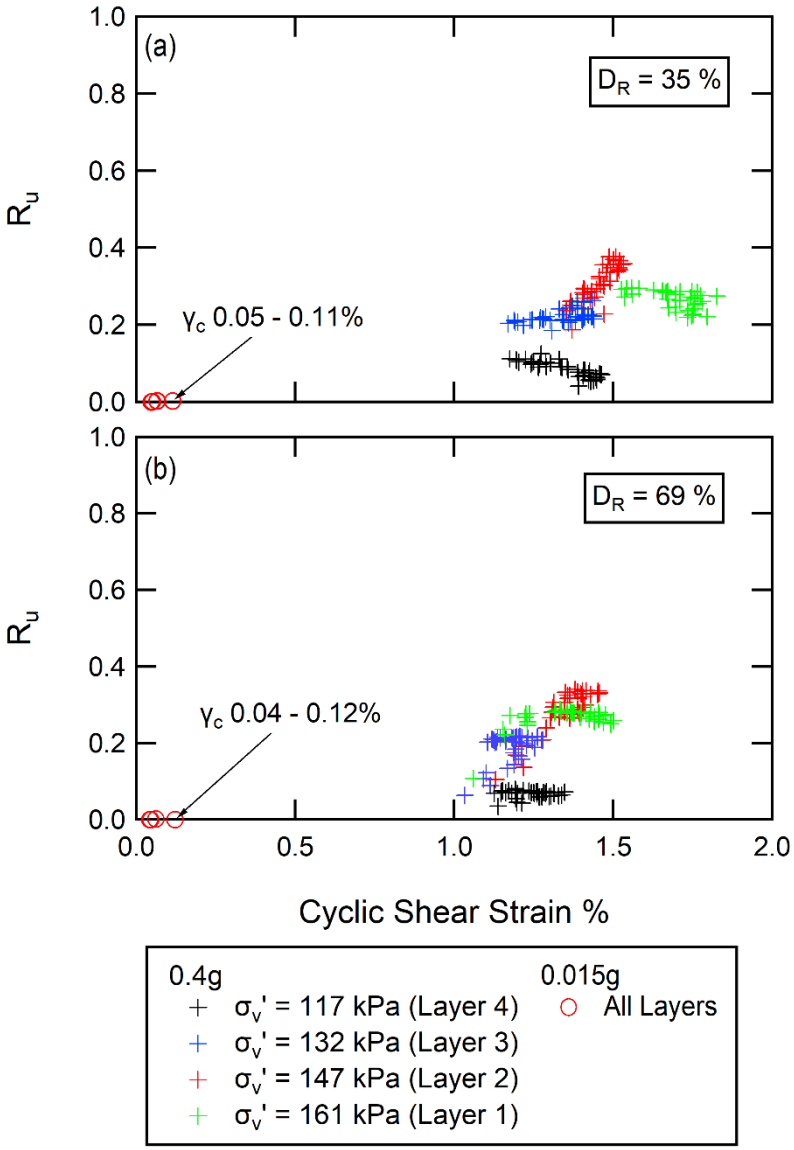

Figure 3.15 Excess pore water pressure development with increasing cyclic shear strain for: (a) Cent1_L, and (b) Cent2_D.

3.4.4 Relationship of pore pressure generation and volumetric strain

This section introduces the analysis of the model in two halves and presents the relationship between R_u and volumetric strain.

Analysis of confinement on soil model (top and bottom halves)

In this section, the model is analyzed in two parts: the bottom and top halves. The importance of analyzing the two halves separately is due to the difference in drainage conditions. The top half experiences free drainage at the surface. The bottom half of the soil has a boundary condition at the bottom of the model container restricting all drainage and an upper boundary condition restrained by hydraulic properties of the soil. The top half therefore experiences greater partial drainage compared to the bottom half. The bottom half of the soil model has greater confinement and therefore greater effective stress.

Since the sensor array has sensors located within each soil layer (4 layers in model), a method is developed to evaluate sensor data representing the analysis of the top half and bottom half of the soil model. The following describes the methodology in which sensor locations shown in Figure 3.16 were chosen.

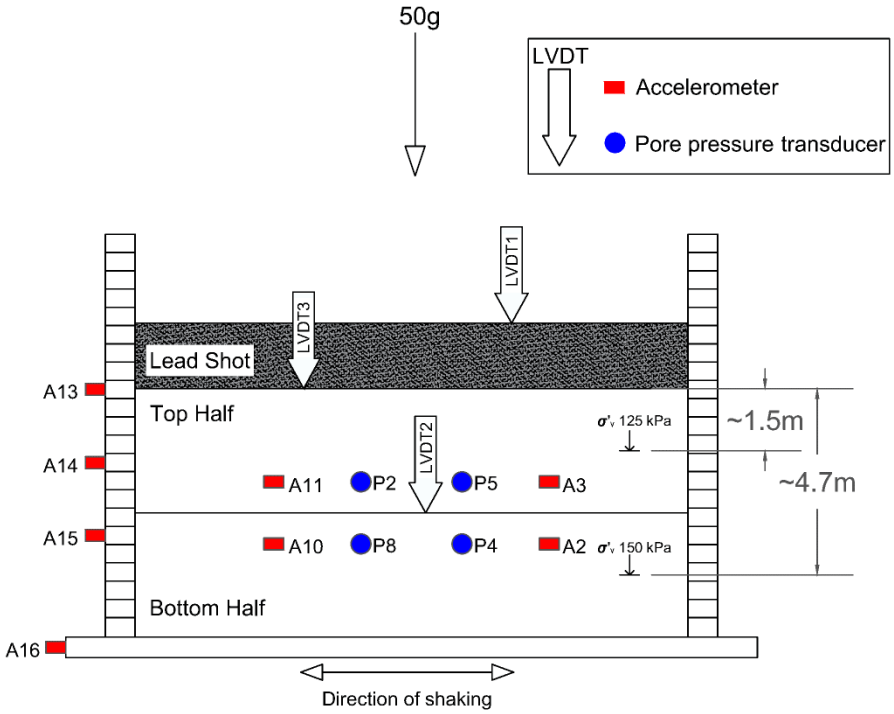

Figure 3.16 Sensor locations representative of top and bottom halves shown in the prototype scale.

As displayed in Figure 3.16, the effective stress representative of the bottom half of the soil model is an average of the known depth locations of the PWP sensor mid layers 1 and 2. This is about 150 kPa at depth 4.7 m (prototype scale). The same method was used to obtain an effective stress representative of the top half of the soil model, 125 kPa at depth 1.5 m. The sensors representative of the top half and bottom half of the soil model were chosen to minimize the effects of the drainage boundary conditions previously mentioned. Therefore, the effective stress time histories were calculated by PWP sensors in layers 3 (i.e., P2 and P5) and 2 (i.e., P8 and P4) for the top and bottom halves, respectively. Shear stress and shear strain are also represented in this way. With the methods previously outlined, the shear stress of the top half of the model is calculated

therefore by accelerometers within layers 3 and 4 and the bottom half by accelerometers within layers 2 and 3.

Figure 3.17 (a) and (b) displays the R_u and volumetric strain data for the bottom and top haves of the loose and dense models, respectively. The figure corresponds to Shake Event 2 in which the models were subjected to base amplitude 0.4g for 40 cycles. Reported relative density is post-consolidation. It is important to note that there is a gap in the data of Cent1_L due to the removal of a spike in the LVDT settlements. It is likely this spike occurred due to the hydraulic pump and is therefore unrepresentative of soil behavior. This results in a lack of data between cycle numbers ~ 0.6 to 1.5 for Cent1_L shown in Figure 3.17 (a). It should also be noted that the LVDT sensors report a small magnitude of noise displayed by the "cyclic" component in the volumetric strain shown in Figure 3.17. Additionally, close observation to before and after the start of shaking shows that the settlement response may not start from zero volumetric strain simultaneously as shaking begins. This noise is accounted for later in the analysis for the relationship of excess pore water pressure with increasing volumetric strain. For the purpose of recognizing trends between the models, this noise is negligible and is ignored for the remainder of the paragraph. At the start of loading, there is an initial transient pore water pressure response most prominent in the bottom half for both models. This is more evident in Cent1_L displayed in Figure 3.17 (a). Following the first cycle, excess pore water pressure begins to develop. Figure 3.17 shows that volumetric strain appears to occur immediately as cyclic loading is applied. Shown clearly in the figure, there is more volumetric strain in the top half compared to the bottom half. This is believed to be primarily due to the greater confinement in the bottom half. Also, there is initial dilative

behavior in the bottom half. For both models, there is greater pore water pressure buildup in the bottom half of the soil model. The pore water pressure has a greater rate of increase in the bottom half and peaks earlier compared to the top half. This earlier peak is evident as there is more time for the pore water to dissipate. It is very likely that there was an upward flow from the bottom to the top half of the model. Comparison of the pore water dissipation for Cent2_D and Cent1_L after shaking shows that the loose model has greater dissipation ability. The top half of the soil model has twice the volumetric strain and less pore pressure.

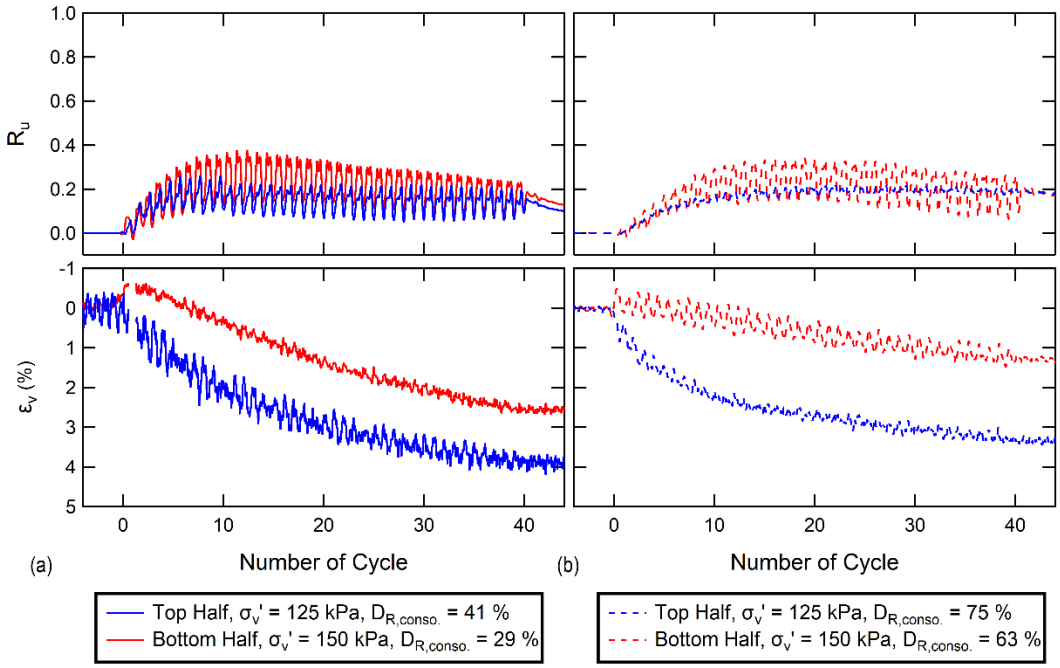

Figure 3.17 Pore water pressure and volumetric strain results for the top and bottom halves of: (a) Cent1_L, and (b) Cent2_D.

Figure 3.18 shows the relationship of volumetric strain and pore pressure generation for the entire soil model during Shake Event 2 for Cent1_L and Cent2_D. The graph was generated by correlating the average R_u and average volumetric strain from each cycle number. As discussed in the previous paragraph, due to noise just prior to shaking, there was some reported volume change at time zero. This was accounted for by an offset to ensure to assess volumetric strain solely due to shaking. Additionally, an average volumetric strain accounts for the slight noise reported by LVDT sensors during shaking. This was calculated by taking the average of the minimum and maximum volumetric strain over each cycle. An average R_u was chosen rather than a maximum R_u to better represent the transient response in initial cycles previously discussed in Figure 3.17. Therefore, data points on Figure 3.18 correspond to the average volumetric strain paired with the average R_u for each cycle during shaking. The R_u to represent the Entire Soil Model was taken as an average of pore pressure sensors located in Layer 2 and Layer 3. The volumetric strain to represent Entire Soil Model was calculated by settlement provided by LVDT3 placed on the soil surface. Previously shown in shaking results, as the high shaking amplitude is applied to the models, volumetric strain occurs immediately, and pore pressure builds gradually. This is seen in Figure 3.18 as volumetric strain of almost 1% is produced with very low pore water pressure generation.

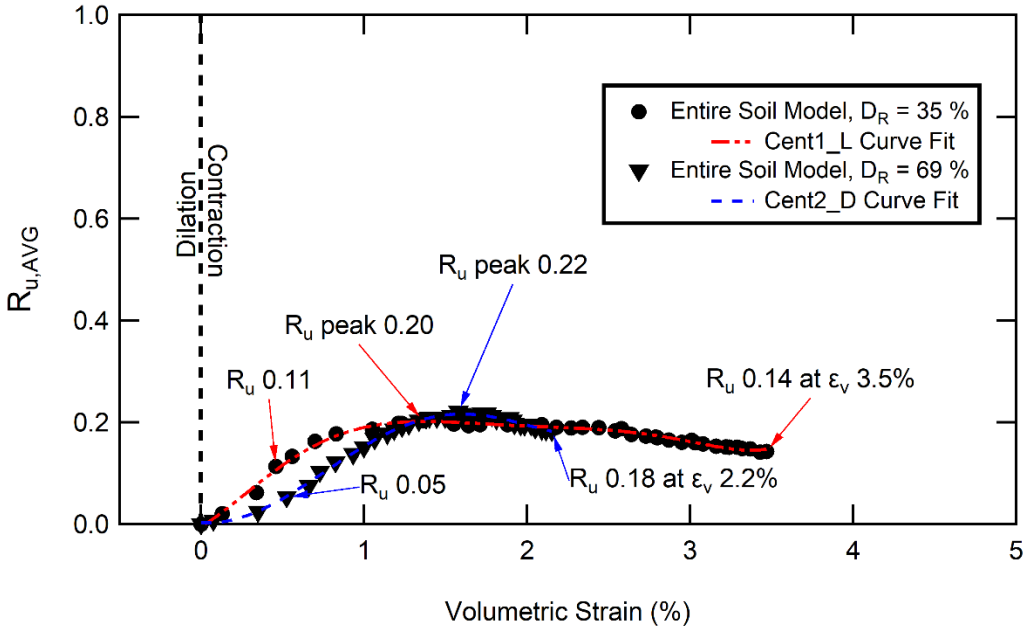

Figure 3.18 Impact of relative density on the relationship of pore water pressure with increasing volumetric strain.

It is useful to use the Entire Soil Model relationships to first assess the impact of relative density on the relationship of excess pore water pressure and volumetric strain. The impact of drainage condition assessed by relationships for the top and bottom halves will be discussed in the paragraph to follow. Shown in Figure 3.18, Cent1_L had a faster rate of increasing R_u with volumetric strain compared to Cent2_D. Cent2_D reached R_u 0.05 at corresponding volumetric strain of about 0.5%. In comparison, at this same value of volumetric strain, Cent1_L had a R_u of 0.11. In addition, excess pore water peaked at a slightly lower volumetric strain of 1.4% in Cent1_L compared to 1.6% in Cent2_D. The excess pore water response for the two models was very similar for volumetric strains ranging 1.2% - 2.2%. At the end of shaking, R_u was lower in the loose model compared to the dense. This is likely due to the higher permeability of the loose model which allowed the flow of water more easily. However, as excess pore water pressure

dissipated, there was a much larger increase in volumetric strain for Cent1_L. At the end of shaking, 3.5% volumetric strain was observed in Cent1_L compared to 2.2% in Cent2_D. Therefore, there was a faster rate of excess pore water pressure dissipation with volumetric strain in Cent2_D. This is contrary to discussed previously the relationship of excess pore water with number of cycle, in which Cent1_L had a faster rate of R_u dissipation with increasing cycle number. This implies that there are greater increases in volumetric strain as excess pore water dissipates in loose gravelly soil compared to dense. This is likely due to the simultaneous upward flow of pore water dissipation with shaking, densifying the soil. Overall, the volumetric strain produced in Cent2_D was less than that of Cent1_L.

The impact of drainage condition and confinement can be assessed by splitting the model into two halves, top and bottom. The top half of the model is in close proximity to the free draining surface and is therefore under partial drainage condition. In comparison, the bottom half of the model simulates a drainage condition that is closer to an undrained condition than a partially drained condition. This is because for the bottom half, the upper boundary condition is controlled by the permeability of the soil above it, and the lower boundary prohibits drainage. Figure 3.19 (a) and (b) shows the relationship of volumetric strain and pore pressure generation for the entire, bottom half, and top half of each model during Shake Event 2. Data points correspond to average R_u and average volumetric strain for each cycle of loading. The sensor locations and settlement calculations representative of the top and bottom halves are the same as was discussed previously in Section 3.4.4. Within each model, it is clear that confinement and drainage condition both have a great impact on the behavior of R_u and volumetric strain as the relationships for

the top half compared to the bottom half are very different. However, the confinement of the bottom half is only 25kPa greater than the top. Therefore, the behaviors observed in Figure 3.19 are probably mainly due to the drainage conditions since the difference in confinement is small. Additionally, the behavior of the top and bottom halves for Cent1_L are similar to that in Cent2_D. This furthermore highlights that the relationship of pore water pressure with increasing volumetric strain is primarily impacted by drainage condition rather than confinement and relative density.

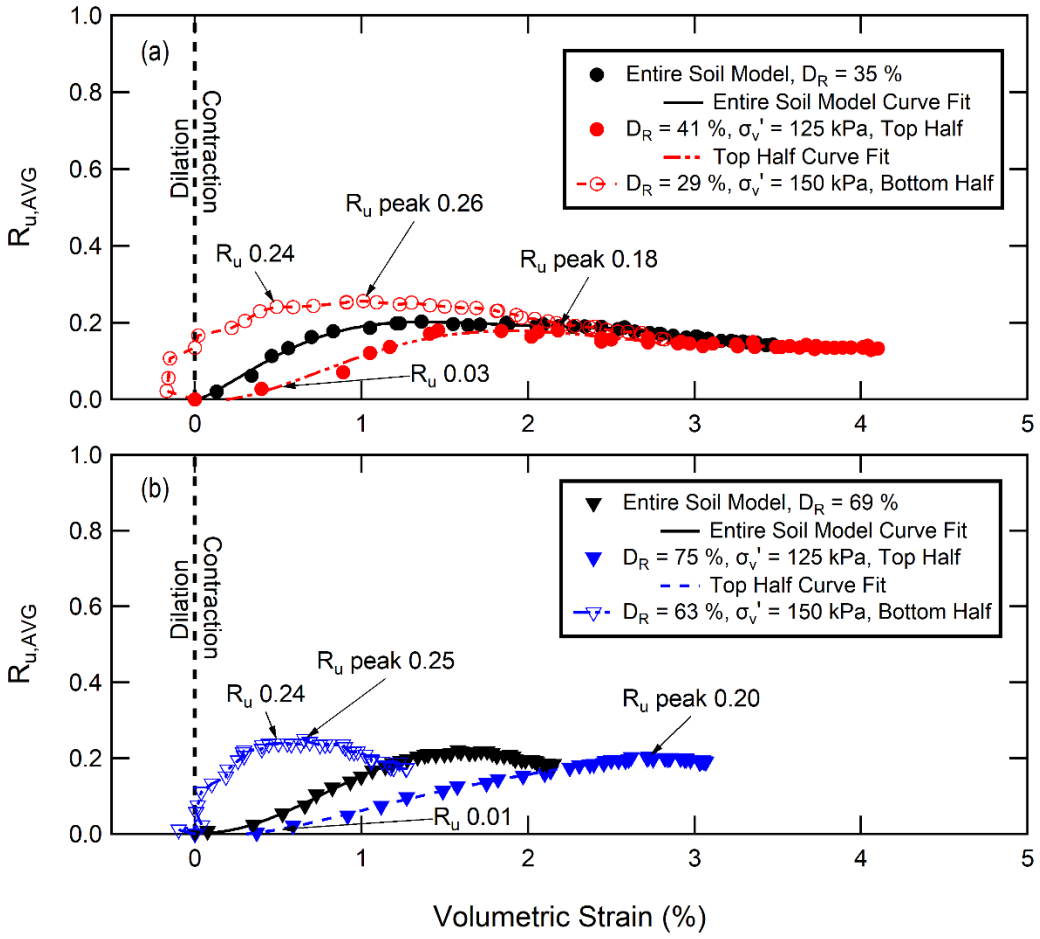

Figure 3.19 Pore pressure generation with volumetric strain for entire soil model, top and bottom half of: (a) Cent1_L, and (b) Cent2_D.

Denoted by post-consolidation relative densities in Figure 3.19, dilation was observed during consolidation in the bottom half of the model while the top half contracted. In the initial cycles of loading, this dilative response was observed again in the bottom half of both Cent1_L and Cent2_D. Dilation was most prominent in Cent1_L with volumetric strain -0.17% compared to -0.10% in Cent2_D. The bottom half of both models had a similar initial rate in excess pore water pressure with increasing volumetric strain. This rate of excess pore pressure with volumetric strain was much greater in the bottom half of the model compared to the top half. As shown in Figure 3.19, for volumetric strain of approximately 0.5%, the R_u observed in the bottom half of the model was 0.24 for both models. At this same volumetric strain, the top half of Cent1_L had R_u 0.03 compared to similar value 0.01 in Cent2_D. This emphasizes that the impact of drainage condition on the excess pore pressure response with increasing volumetric strain is greater than the impact of relative density. As mentioned, this faster rate of R_u in the bottom half represents a near-perfect undrained condition, meaning the drainage condition is closely related to the idealized undrained condition. This caused a larger peak in R_u at a lower value of volumetric strain in the bottom half of the model compared to the top. In contrast, partial drainage in the top half of the model caused a slower rate in increasing pore water pressure with increasing volumetric strain. Additionally, the top half had a maximum value of R_u at larger volumetric strains. This is because the top half of the soil model had larger increases in volumetric strain compared to the bottom as pore pressures simultaneously dissipated. The response in pore water pressure dissipation with increasing volumetric strain between the two halves was most different for the denser model, seen in Figure 3.19 (b). In this model, pore pressures dissipated at a much faster

rate with increasing volumetric in the top half of the model compared to the bottom. In comparison, the rate of R_u dissipation shown in Figure 3.19 (a) for the top and bottom halves of Cent1_L are similar, especially for volumetric strains greater than 2%. In general, for both models, volumetric strain at the end of shaking in the top half of the model was much greater than that of the bottom. In addition to drainage condition, another possible explanation for this is the surcharge stress that was assumed uniform with depth was greater experienced by the top half, and the stress reduced with depth.

From the figure, it can be concluded that soils with higher confinement and near-perfect undrained condition exhibit a faster rate of R_u with volumetric strain and a lower total volume change. Soils with lower confinement under the partial drainage condition have a slower rate of R_u with volumetric strain and a larger volume change. Therefore, this highlights that drainage condition has a major impact on the development of excess pore water pressure as partial drainage decreases the rate of R_u with volumetric strain. These results show that the general trends found when splitting up the model into upper and lower halves are primarily influenced by drainage condition and not by relative density.

3.5 Shear Modulus and Damping

This section describes two methods to obtain shear modulus and damping and presents results and analysis from the preferred method. Figure 3.20 displays an example of stress-strain loop for both methods detailed below.

3.5.1 Discussion of calculation methods

Method 1 - Calculations from maximum and minimum shear strain

The area inside of the loop of each cycle is calculated by the sum of numerical integration of the shear-strain shear-stress relationship over that cycle:

$$\Delta W = \sum_{i=0}^{n} \frac{1}{2} (\gamma_{i+1} - \gamma_i) * (\tau_{i+1} + \tau_i)$$

Eq. 3.6

where ΔW is the area of the loop; γ_i is shear strain of cycle *i*; γ_{i+1} is shear strain of cycle *i+1*; τ_i is shear stress of cycle *i*; and τ_{i+1} is shear stress of cycle *i+1*.

Forward and reverse shear strain for each cycle is found by calculating the maximum and minimum shear strain over the entire cycle. Forward loading results in positive measurements of shear strain compared to negative results for reversal. These values are used to calculate the adjusted shear strain for forward and reversal of each cycle by:

$$\gamma_{pos._{N=i}} = \gamma_{max_{N=i}} - (\frac{\gamma_{max_{N=i}} + \gamma_{min_{N=i}}}{2})$$

Eq. 3.7

$$\gamma_{neg._{N=i}} = \gamma_{min_{N=i}} - (\frac{\gamma_{max_{N=i}} + \gamma_{min_{N=i}}}{2})$$

Eq. 3.8

where $\gamma_{pos._{N=i}}$ and $\gamma_{neg._{N=i}}$ are the forward and reverse shear strain for cycle *i*, respectively; and $\gamma_{max_{N=i}}$ and $\gamma_{min_{N=i}}$ are the maximum and minimum shear strain over cycle *i*, respectively. These adjusted shear strain values are used to calculate the shear modulus from forward and reverse shear stress-strain curve:

$$G_{pos.} = \frac{\tau_{pos.}}{\gamma_{pos.}/100}$$

Eq. 3.9

$$G_{neg.} = \frac{\tau_{neg.}}{\gamma_{neg.}/100}$$

Eq. 3.10

where $G_{pos.}$ and $G_{neg.}$, are forward and reverse shear modulus, respectively; $\tau_{pos.}$ and $\tau_{neg.}$ are forward and reverse shear stress, respectively; and $\gamma_{pos.}$ and $\gamma_{neg.}$ are forward and reverse shear strain, respectively.

The shear modulus of that cycle is then taken as an average of $G_{pos.}$ and $G_{neg.}$:

$$G = \frac{G_{pos.} + G_{neg.}}{2}$$

Eq. 3.11

Damping is calculated by:

$$D = \frac{1}{4\pi}\frac{\Delta W}{W} * 100$$

Eq. 3.12

where ΔW is the area inside the loop (previously defined); and W is the average of $W_{pos.}$ and $W_{neg.}$:

$$W_{pos.} = \frac{1}{2}\left(G_{pos.} * \frac{\gamma_{pos.}}{100}\right) * \gamma_{pos.}$$

Eq. 3.13

$$W_{neg.} = \frac{1}{2}\left(G_{neg.} * \frac{\gamma_{neg.}}{100}\right) * \gamma_{neg.}$$

Eq. 3.14

Method 2 - Calculations from slope of linear equation

An alternative way of calculating shear modulus and damping is using the slope of a linear equation developed from the relationship of shear stress and shear strain. The slope of the best fit of shear stress-strain data is calculated (refer to Figure 3.20 (b)). This slope is then used to calculate the shear modulus G by multiplying it by 100.

A cyclic shear strain is calculated to obtain shear strain that is uniform in forward and reversal direction. The cyclic shear strain is plot with shear stress to obtain the loop for each cycle:

$$\gamma_{c_{N=i}} = \left(\frac{\gamma_{pos.N=i} - \gamma_{neg.N=i}}{2}\right)$$

Eq. 3.15

where $\gamma_{c_{N=i}}$ is the cyclic shear strain for cycle *i*; $\gamma_{pos.N=i}$ is the forward shear strain for cycle *i* (previously defined); and $\gamma_{neg.N=i}$ is the reverse cyclic shear strain for cycle *i* (previously defined). W is calculated using the G calculated by the slope and the cyclic shear strain (γ_c):

$$W = \frac{1}{2}\left(G * \frac{\gamma_c}{100}\right) * \gamma_c$$

Eq. 3.16

where G is the shear modulus; and γ_c is the cyclic shear strain. Damping is calculated with the equation previously defined using this W above.

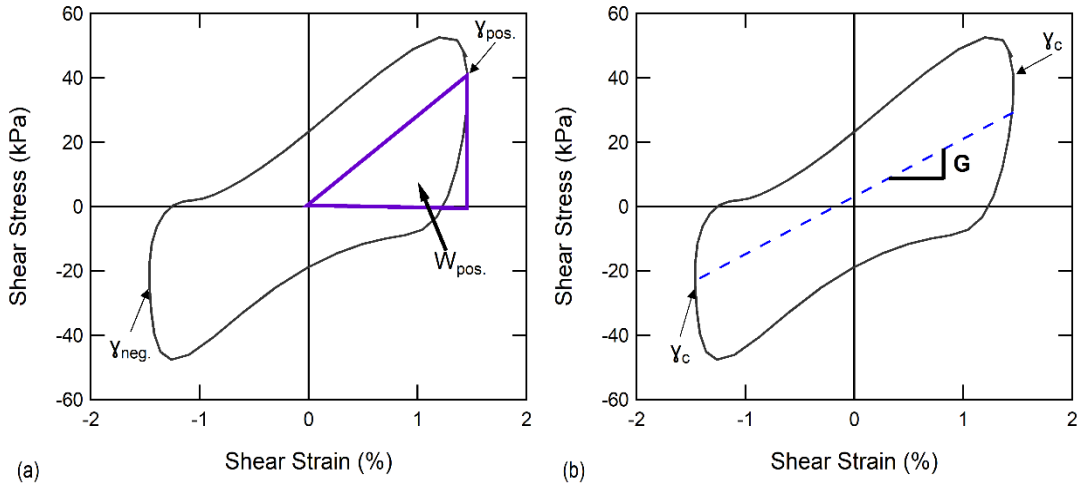

Figure 3.20 Example of shear stress-strain loop for: (a) Method 1, and (b) Method 2.

3.5.2 Shear modulus and damping results

During data analysis, it was observed that some cycles produced incomplete stress-strain loops or loops that crossed over one another. For this reason, shear stress-strain loops were carefully viewed and handpicked to ensure ΔW represented the area of a full complete loop. Figure 3.21 shows the shear modulus and damping for the dense model calculated by the two different methods previously outlined. By observation, it can be concluded that that the two methods have the same trends for both shear modulus and damping. The two methods both use numerical integration to calculate the area within the loop (ΔW). The cyclic shear strain calculated by each method results in the same value. The difference in the methods is in the approximation of the shear modulus. The shear modulus obtained by using the slope of the linear equation method considers the entire loop as it is a best fit of all the data points. Whereas the shear modulus calculated using the shear stress and shear strain has some limitation as the maximum and minimum shear stress is used to define shear moduli from both the forward and the reverse loading of the shear stress – strain curve. Therefore, in the case of a non-uniform loop, the full loop may

not be represented but rather just the slopes of the peak of forward and reverse shear. Also, the average of the forward and reverse shear modulus may be dominated by one or the other.

Displayed in Figure 3.21, as the cyclic loading increases, the shear modulus decreases slightly with the highest G in the deepest layer (Layer 1). The damping decreases gradually as cyclic loading increases. Layer 4, which has the lowest confinement, has the highest damping response. It can be noticed that for both methods Layer 4 has the most deviation of shear modulus and damping from the other three layers. The first method, using maximum and minimum shear strain, has a larger dispersion and higher irregularity between layers for the shear modulus and damping. Additionally, the values of shear modulus are much higher compared to those calculated by Method 2. This is most likely because Method 2 considers the entirety of the loop by using a best fit. The slope of this best fit would be expected to be lower than the slopes calculated from maximum and minimum shear stresses as in Method 1. Therefore, moving forward, shear modulus and damping results shown are calculated by Method 2 (using slope linear equation). This method was chosen because it has the most uniformity for both damping and shear modulus.

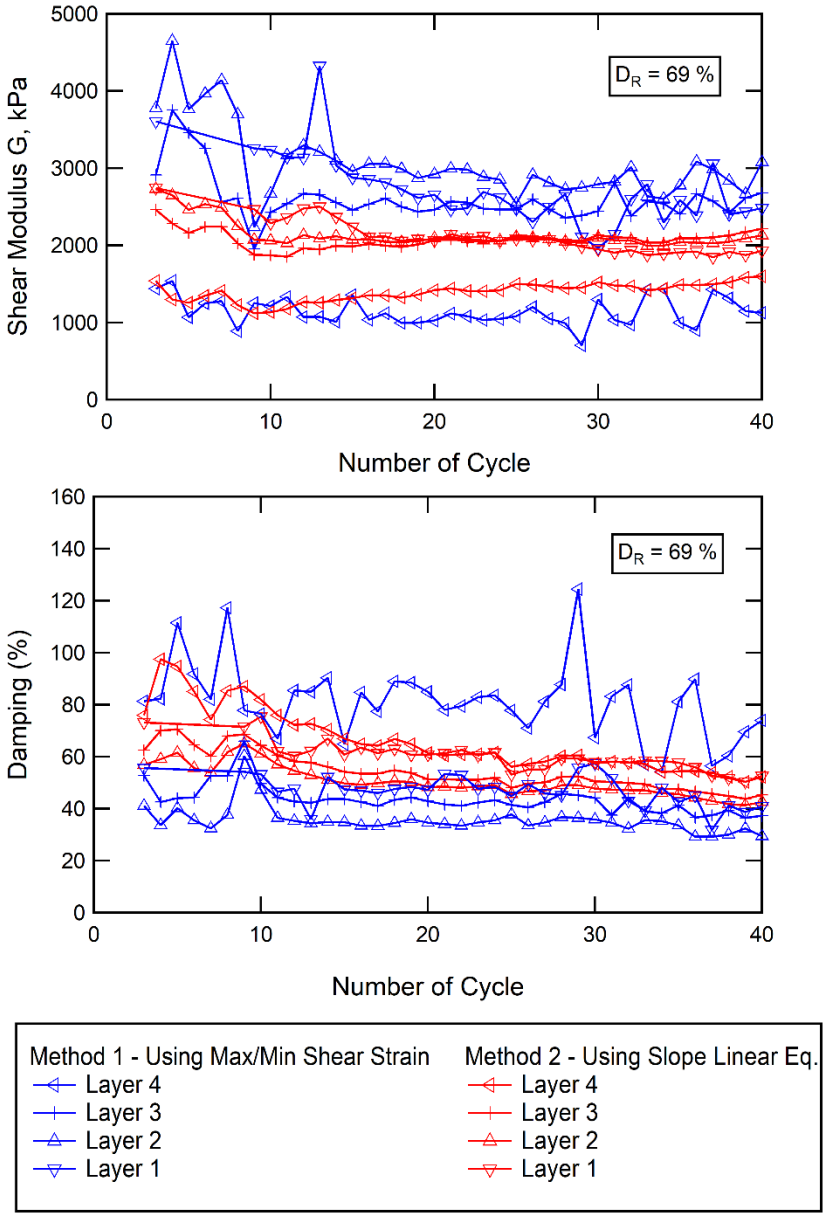

Figure 3.21 Comparison of shear modulus and damping calculated by Method 1 and Method 2 for Cent2_D (Shake Event 2 0.4g).

Figure 3.22 (a) and (b) displays shear modulus and damping results for Cent1_L and Cent2_D, respectively. In general, damping reduces with increasing loading cycle while shear modulus has an initial decrease followed by a slight increase. The impact of relative density is clear for both shear modulus and damping. Higher shear modulus and lower damping was observed in Cent2_D in comparison with Cen1_L. The average G in the first 4 cycles of those chosen for analysis ranged 752 – 1696 kPa in Cent1_L compared to 1361 – 2594 kPa in Cent2_D considering all soil layers. This is to be expected as density affects shear modulus. In contrast, the average damping values in the first 4 cycles chosen for analysis ranged 70 – 134 % in Cent1_L while just 58 – 88 % in Cent2_D. As mentioned, both models have an initial decrease in shear modulus followed by a slight increase. The rate of decrease in the earlier cycles is much greater for Cent2_D. The following increase begins earlier in Cent1_L compared to Cent2_D (~ cycles 8 and 11, respectively). This implies that Cent1_L begins to regain stiffness earlier in cyclic loading compared to Cent2_D. Also, over the duration of cyclic loading, Cent1_L has a gross increase in G in soil layers 4, 3, and 2 while Cent2_D has a gross decrease in soil layers 3, 2, and 1. As mentioned, shear modulus for Cent1_L in earlier cycles decreases which is therefore contrary to the overall response. This decrease is most dramatic for Layer 1 and Layer 2, located in the bottom half of the soil model. A possible explanation for this is the initial dilative behavior noticed in Figure 3.19 (a) for the bottom half of the model (layers 1 and 2). In Figure 3.19 (a), the first data point corresponding to contractive volumetric strain in Cent1_L is data point 6, corresponding to the 6^{th} cycle of loading. In comparison, in Figure 3.22 (a), Cent1_L begins to increase in stiffness around the same cycle (i.e., ~ cycle 8). Cent1_L has greater damping

compared to Cent2_D for each layer which is expected for the sample with lower density. The rate of decrease in damping with loading cycles is greater for Cent1_L, especially for the shallowest layer. Over the duration of cyclic loading, there is more reduction in damping for Cent1_L. In earlier cycles, damping response in Cent2_D varies but begins a steady decline at approximately Cycle 9, just before G begins to increase at ~ Cycle 11 mentioned previously.

Results shown in Figure 3.22 can also be correlated with the development of pore water pressure. As previously discussed, the peak pore pressure buildup occurred in Layer 2 for both models. This layer also has the lowest damping throughout cyclic loading. As the R_u reaches its maximum point at cycle 20 in Cent2_D, the G in the deeper layers tends to become more uniform. This behavior is not clearly observed in the loose model.

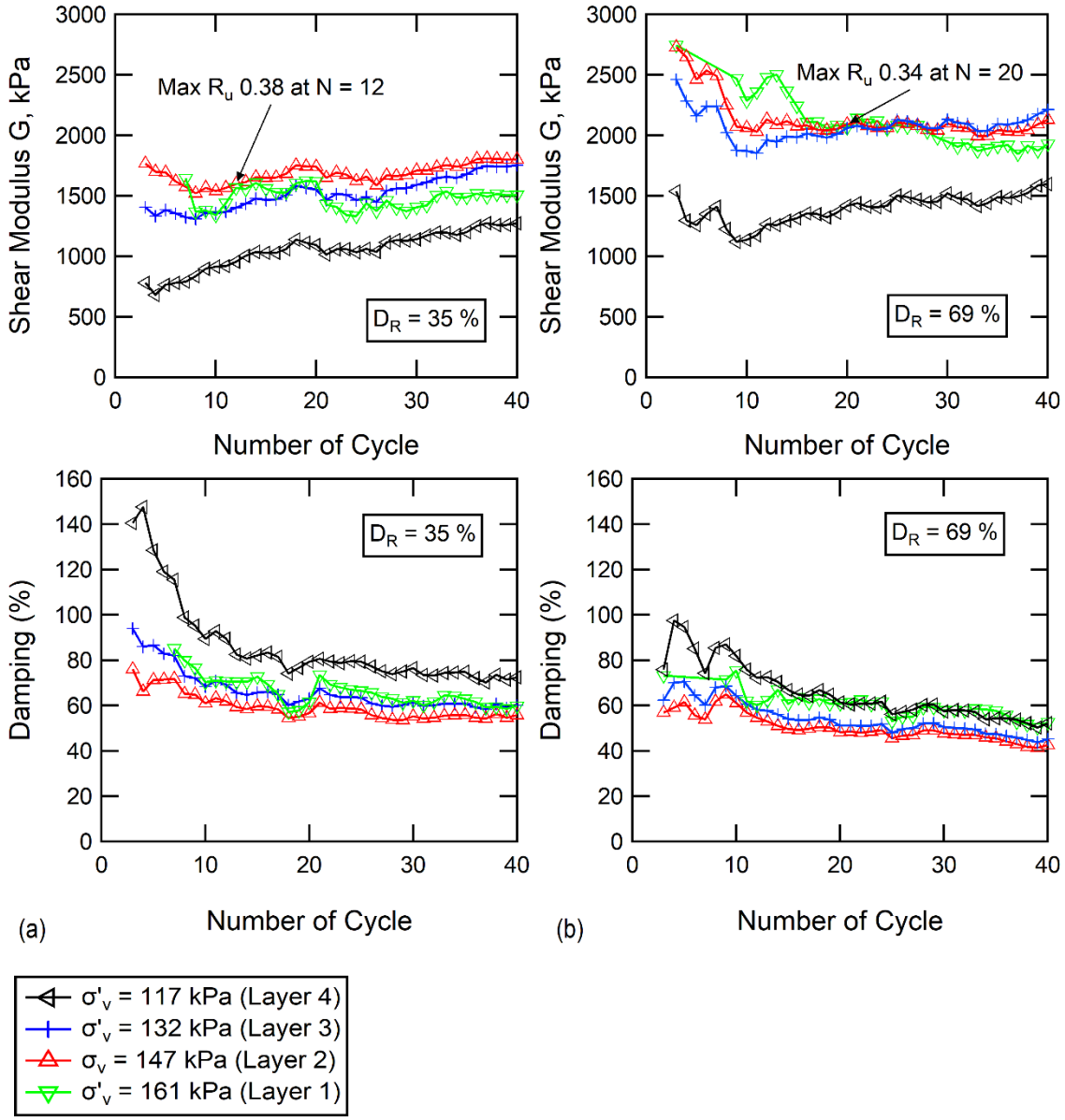

Figure 3.22 Shear modulus and damping for Shake Event 2 0.4g: (a) Cent1_L, and (b) Cent2_D.

There is a clear impact of confinement on both shear modulus and damping response. Even though the response of shear modulus with increasing loading cycle is different for the two relative densities, both models follow the same general trend as confinement increases. The bottom 3 layers (effective stress ranging ~ 130 to 160 kPa) have similar values of shear modulus while Layer 4 (effective stress 117 kPa) outlies with

lower values. This trend is most prominent in Cent2_D displayed in Figure 3.22 (b). This implies that low effective confinement has a major effect on the shear modulus of gravelly soil. This observation is further supported when analyzing the total change in shear modulus during cyclic loading (shear modulus of last cycle subtracted by the shear modulus of the first chosen loop). This is displayed for both models in Table 3.4 and Figure 3.23 (a) in which a positive ΔG represents a net increase in stiffness during shaking. As mentioned, the three deeper soil layers in Cent2_D suffered a total decrease in G, however Layer 4 had a net increase. Regardless, the general decreasing trend in shear modulus with increasing cyclic loading in this model becomes more prominent for increasing confinement. That is, the greatest loss in stiffness due to the dynamic load in Cent2_D occurred in the layer subjected to the highest confinement. This is shown at Cycle 40 in Figure 3.22 (b) where the highest G was observed for the lower confinement (excluding outlier Layer 4). In comparison, values of ΔG in Table 3.4 for Cent1_L show that the model has a general increasing trend in shear modulus with cyclic loading. However, despite soil layers 4, 3, and 2 increasing in G, the deepest soil layer (Layer 1) decreased in G. Comparison of the two models in Figure 3.23 reveals that, as confinement increased, there was a greater magnitude of decrease in G in Cent2_D and lesser magnitude of increase in G in Cent1_L. For both loose and dense conditions, Figure 3.23 shows a decreasing linear relationship for the impact of confinement on the change in shear modulus during cyclic loading. In the dense model, despite the general trend of negative ΔG, the layer with lowest confinement had positive ΔG. In the loose model, ΔG was negative in Layer 1 with highest confinement despite the general trend of positive ΔG in all other layers. In other words, greater confinement led to a greater loss in

stiffness with number of cycle of dense soil while a lesser gain in stiffness with number of cycle of loose soil. Additionally presented Table 3.4 and Figure 3.23 is the estimated change in damping during cyclic loading (ΔD) with confinement for both models. In general, damping reduces with increase in loading cycle (negative ΔD) despite relative density and confinement. The impact of confinement on ΔD is displayed as a parabolic relationship in Figure 3.23 (b). In both models, the magnitude of -ΔD is greatest for the shallowest layer (Layer 4). As confinement increases in layers 3 and 2, the value of overall decrease in damping due to cyclic loading reduces. However, the highest confinement (Layer 1), has a greater decrease in damping than Layer 2, forming the parabolic relationship of ΔD with confinement. The greater decrease in damping due to cyclic loading likely due to the high cyclic shear strain in this layer (refer to Figure 3.14).

In conclusion, Figure 3.23 shows clearly the impact of confinement on the changes in shear modulus and damping due to shaking. Overall, higher relative density caused a loss in stiffness after cyclic loading and higher confinement exacerbated this effect. In contrast, loose relative density resulted in a gain in stiffness after shaking and this trend increased as confinement decreased. This finding is logical as low confinement and loose material leads to greater densification. Damping decreased with increasing loading cycles shown in Figure 3.22. For both relative densities, damping response was lowest in the layer that had maximum excess pore water pressure. Figure 3.23 (b) shows that at the end of shaking, damping was reduced, and this reduction was most prominent in the shallow layers. The shallowest layer had the highest damping and the lowest shear modulus for the duration of cyclic loading. The change in damping does not follow the same trend as shear modulus with respect to confinement.

Table 3.4 Impact of confinement on the changes in shear modulus and damping over the duration of cyclic loading.

Change during cyclic loading	Effective confinement (kPa)	Cent1_L	Cent2_D
ΔG (kPa)	117	+ 491	+ 60
	132	+ 345	- 249
	147	+ 32	- 600
	161	- 138	- 815
ΔD (%)	117	- 68	- 24
	132	- 34	- 17
	147	- 20	- 14
	161	- 25	- 21

*negative represents decrease, positive represents increase

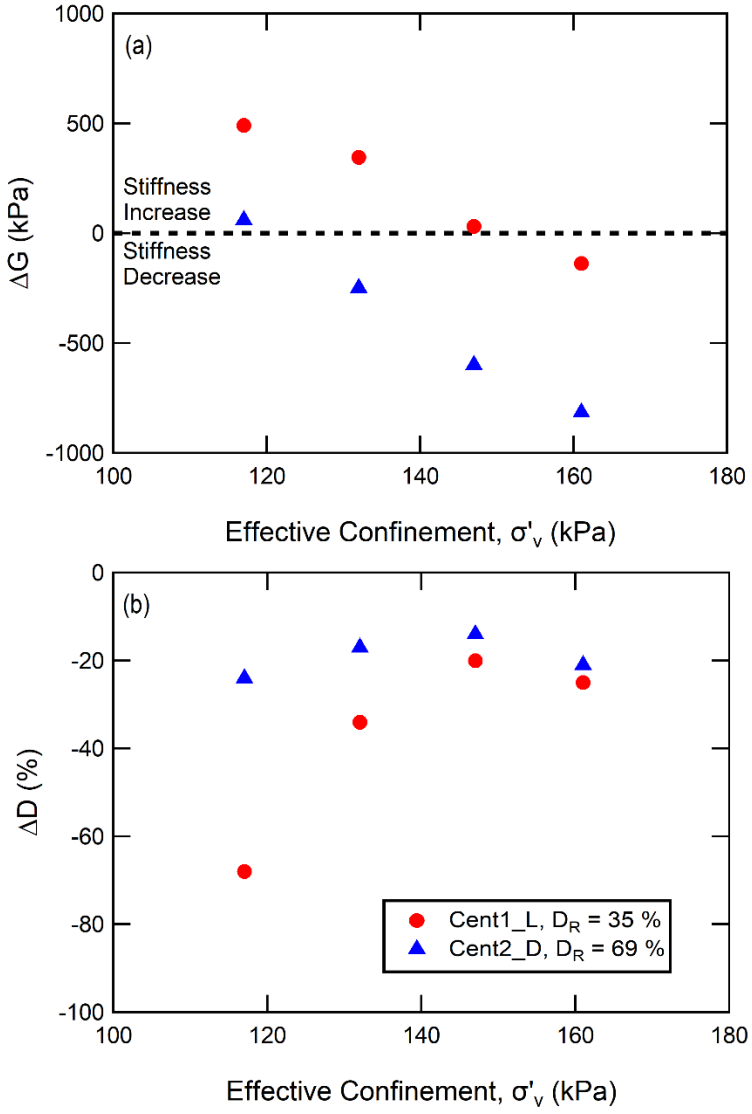

Figure 3.23 Impact of effective confinement on change in: (a) Shear modulus, and (b) damping, during shaking.

Figure 3.24 (a) and (b) display the relationship of shear modulus and damping response with increasing cyclic shear strain for Cent1_L and Cent2_D, respectively. Results for Layers 2 and 3 from Shake Event 2 (0.4g) and all layers from Shake Event 1 (0.015g) are included. Results from only two layers from Shake Event 2 are plotted to aid in readability, and those selected were chosen because these sensor locations represent the two halves of the models. It is also important to note that only one data point from

each layer from Shake Event 1 is included as it was the cycle that provided a clear loop for analysis due to a very low amplitude of shaking. For Shake Event 1, the shear modulus ranged 2102 – 3759 kPa in Cent1_L and 3816 – 7854 kPa in Cent2_D. The damping response to this same shaking amplitude ranged from 17 – 22 % for Cent1_L and 25 – 27 % for Cent2_D. There is a clear impact of relative density that is more prominent for shear modulus. As relative density increased about 35 %, the average shear modulus nearly doubled. This impact was also recognized for Shake Event 2, as the average of shear modulus amongst all layers in Cent2_D was about 1.6 times greater than that of Cent1_L. In both shaking events, there was a wider range in damping for Cent1_L. This was more prominent in Shake Event 2 easily seen in Figure 3.24. In general, the shear modulus was higher for the low shaking amplitude and damping was lower. This is likely due to the lower cyclic shear strain produced by Shake Event 1. The cyclic shear strain in response to 0.015g in both models were very similar and ranged from 0.048% – 0.114% in Cent1_L compared to 0.043% – 0.122% in Cent2_D. For Shake Event 2, the average cyclic shear strain for the duration of shaking ranged from 1.3% – 1.7% in Cent1_L and 1.2 – 1.4 % in Cent2_D considering all layers. This suggests that the impact of relative density on cyclic shear strain increases for higher shaking amplitudes.

In addition, confinement had the same impact on cyclic shear strain for both shaking events. For Shake Event 1, the lowest cyclic shear strain response was in the shallowest layer and increased as confinement increased. This trend was also noticed in Shake Event 2 and is likely due to the high damping in shallower layers. However, comparison of both shaking events reveals different trends for the effects of confinement

on shear modulus. For both models, the shear modulus response to Shake Event 1 in the deepest layer (Layer 1) was an outlier compared to the other layers. This is most noticeable in Cent2_D in Figure 3.24 (b), as the shear modulus for the highest confinement is much less than the layers above it. This is contrary to the previous discussion regarding Shake Event 2. Recalling Figure 3.22, the outlier in shear modulus response for both loose and dense models was the shallowest layer (Layer 4). This implies that the impact of confinement on shear modulus is affected by the magnitude of shaking amplitude applied to the soil. It was observed that at a given cycle, the impact of confinement caused greater variability in shear modulus for Shake Event 1 and greater variability in damping for Shake Event 2. For example, the damping values for different confinements in response to Shake Event 1 shown in Figure 3.24 vary 4% and 2% for Cent1_L and Cent2_D, respectively. To compare with Shake Event 2, the difference in damping response between confinements at any given cycle was calculated. The maximum difference in damping value between different confinement was 81% for Cent1_L and 38% Cent2_D. The same analysis was done for shear modulus to consider the impact of confinement for different shaking amplitudes. In response to Shake Event 1, Cent1_L varied 1657 kPa and Cent2_D varied 4038 kPa. In contrast, the maximum difference between confinement at a given cycle for Shake Event 2 was 1020 kPa for Cent1_l and 1351 kPa for Cent2_D. This implies that higher cyclic shear strains (> 1%), produced by high amplitude cyclic loading, has a greater impact on the variability of damping compared to that at lower cyclic shear strains (0.03% – 0.2%). In contrast, lower cyclic shear strains (0.03% - 0.2%), produced by low shaking amplitude, has a greater impact on the variability of shear modulus compared to higher cyclic shear strains (>

1%). It is possible that this observation in the data is due to the lack of clear loops for Shake Event 1 due to such low shaking amplitude.

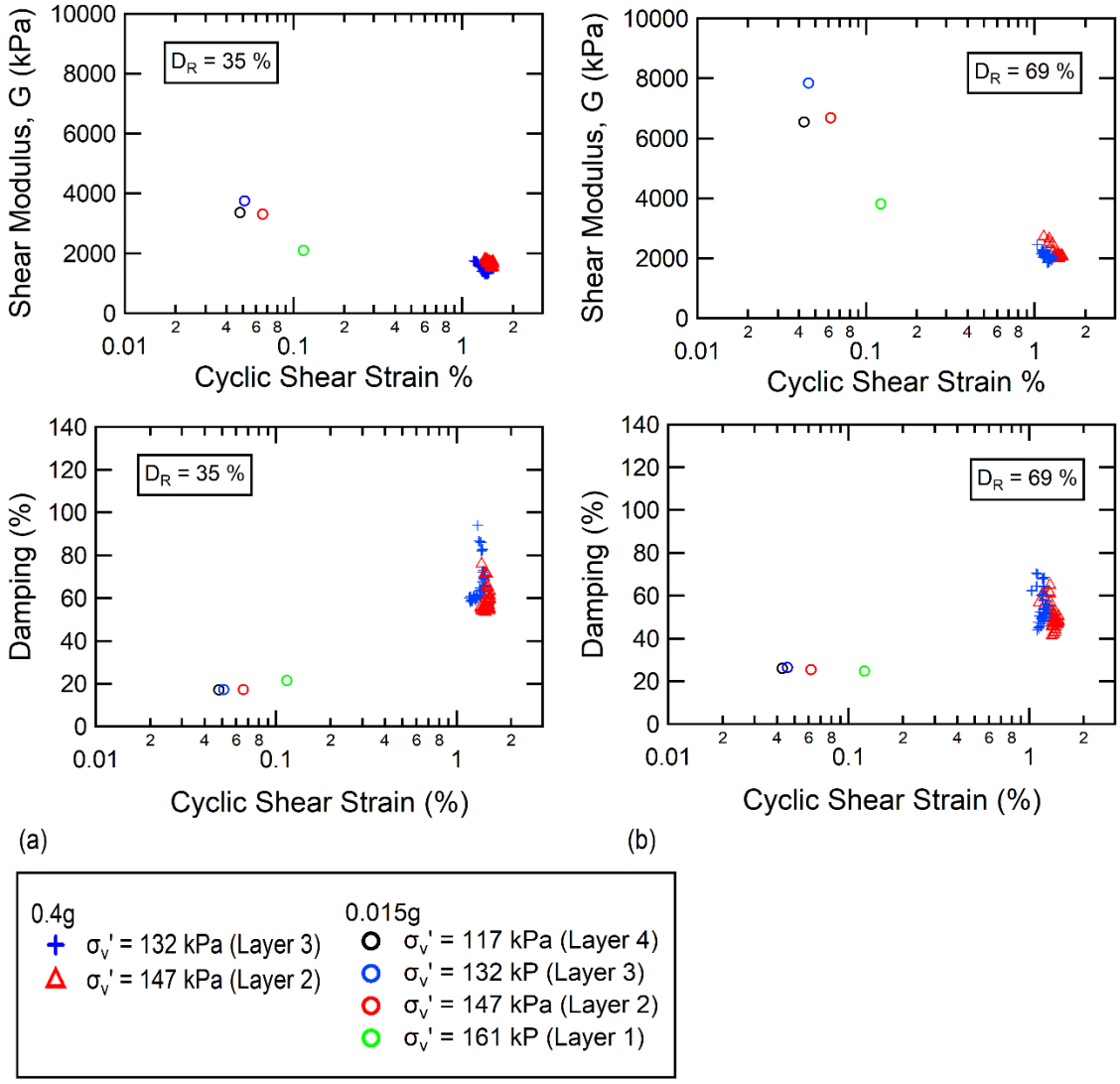

Figure 3.24 Relationship of shear modulus and damping with cyclic shear strain for acceleration 0.4g and 0.015g: (a) Cent1_L, and (b)Cent2_D.

3.6 Post test observation

Following spin down to 1g, a visual investigation was completed for both models. First, the model was inspected, displacement of every stack in the laminar box was recorded, and the lead shot and soil surface were measured at 9 locations. This process is

shown for Cent1_L and Cent2_D in Figure 3.25 (a) and (b), respectively. It can be seen clearly that the displacement in the laminar stacks of Cent1_L is greater in comparison to Cent2_D. Additionally, this permanent lateral deformation is shown in Figure 3.26 with depth beneath the soil surface. Interpolation between laminar stacks above and below the soil surface was used to define the lateral deformation at the surface and is represented by a dashed line in Figure 3.26. A new soil model height was defined by taking an average of 9 surface measurements. To obtain an estimated post-test layer thickness, this new soil height was divided into 4. This required the assumption that the model settled evenly amongst the 4 layers. With known target heights for each layer, the model was deconstructed by carefully scooping each layer into a pan. Measurement of the lateral and vertical displacements of the accelerometers and pore pressure transducers was completed as the soil was removed. This is shown in Figure 3.27. The visual assessment and measurement of post-test sensor locations was compared to LVDT data which agreed well for both models.

Figure 3.25 Post-test visual assessment of centrifuge models: (a) Cent1_L, and (b) Cent2_D.

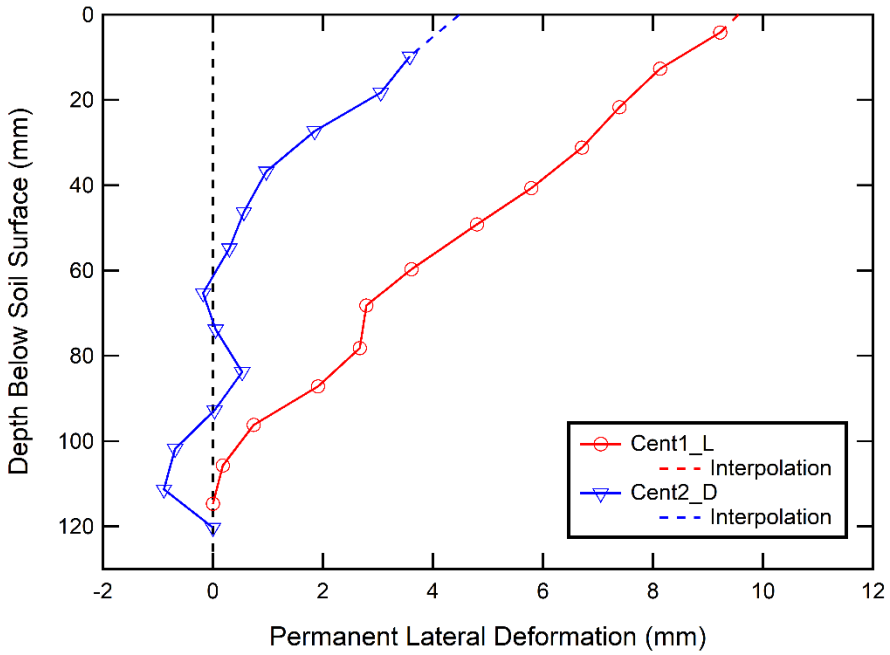

Figure 3.26 Permanent lateral deformation in models Cent1_L and Cent2_D.

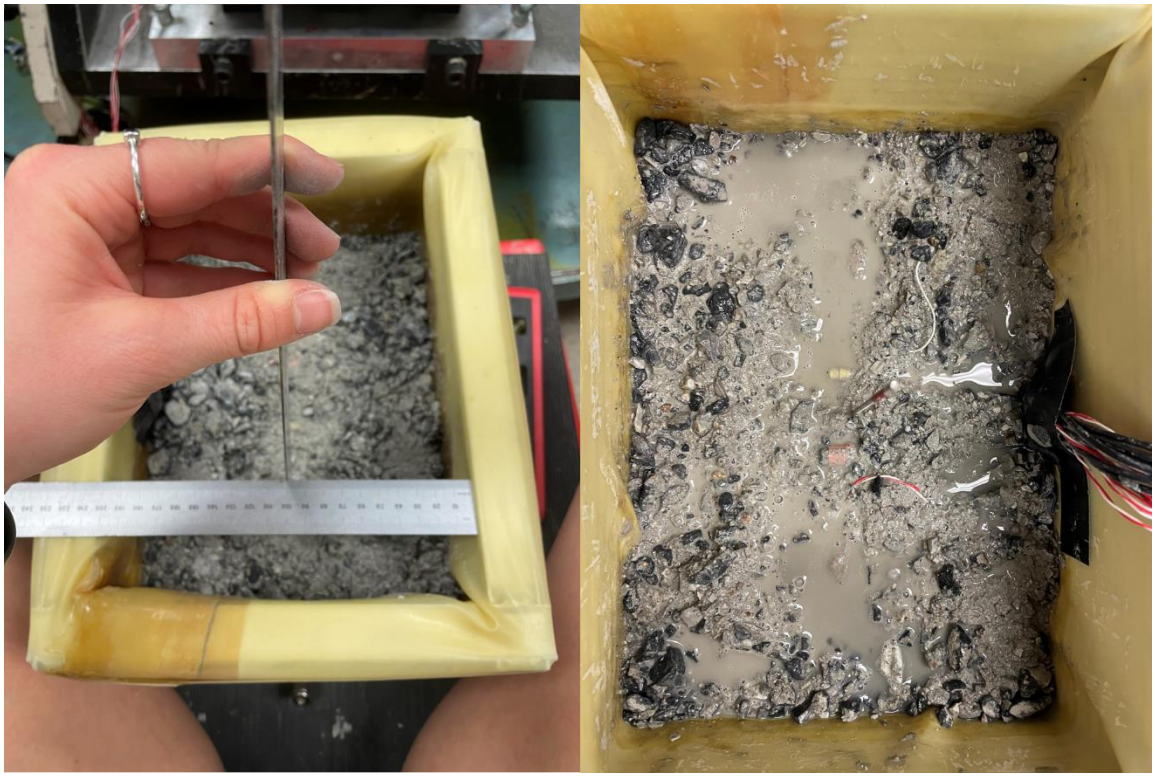

Figure 3.27 Measurement of horizontal and vertical displacement of accelerometers and pore pressure transducers post-cyclic loading.

A sieve analysis composed of both wet and dry sieve with No. 4, 40 and 200 was completed to assess the post-test grain size distributions within each layer. The purpose of this was to assess the migration of grain sizes in the model during cyclic loading. The initial and posttest percent finer grain size distributions for sieves No. 4, 40, and 200 is displayed in Figure 3.28. For both models, the two middle layers are most similar to the original grain size distribution. However, Layer 4 (top) has a percent finer trend above the initial compared to one that is below the initial for Layer 1 (bottom). This implies a migration of finer particles to the bottom layer, leaving larger particles to the surface. This migration of finer particles to the bottom of the model is logical as shaking caused densification in both models. The migration is greatest for particle size finer than 4.75mm, gravel, displayed by the greatest deviance from the initial GSD in Figure 3.28. There is not much migration of fine particles, as the post test result is very similar to the initial as seen in Figure 3.28. The migration of finer particles seems uniform in the loose model as the percentage finer increased for each layer closer to the bottom. However, the dense model seems to have particle migration in two halves. Shown on Figure 3.28, there is a decrease in finer particles at the surface, but an increase in the layer just below (Layer 3). Similarly in the bottom half of the model, there is a decrease in finer particles in Layer 2 and an increase in Layer 1 (bottom). In other words, the dense model has migration of finer particles to the lower layers of the top half and bottom halves. In general, larger particle sizes were left at the surface as smaller particle sizes migrated to the bottom. In contrast, Ruttithivapanich & Sasanakul (2023) performed centrifuge tests on gravelly soil and found migration of fine particles to the surface post liquefaction. The difference in

these results could possibly be due to liquefaction not occurring in either model Cent1_L and Cent2_D.

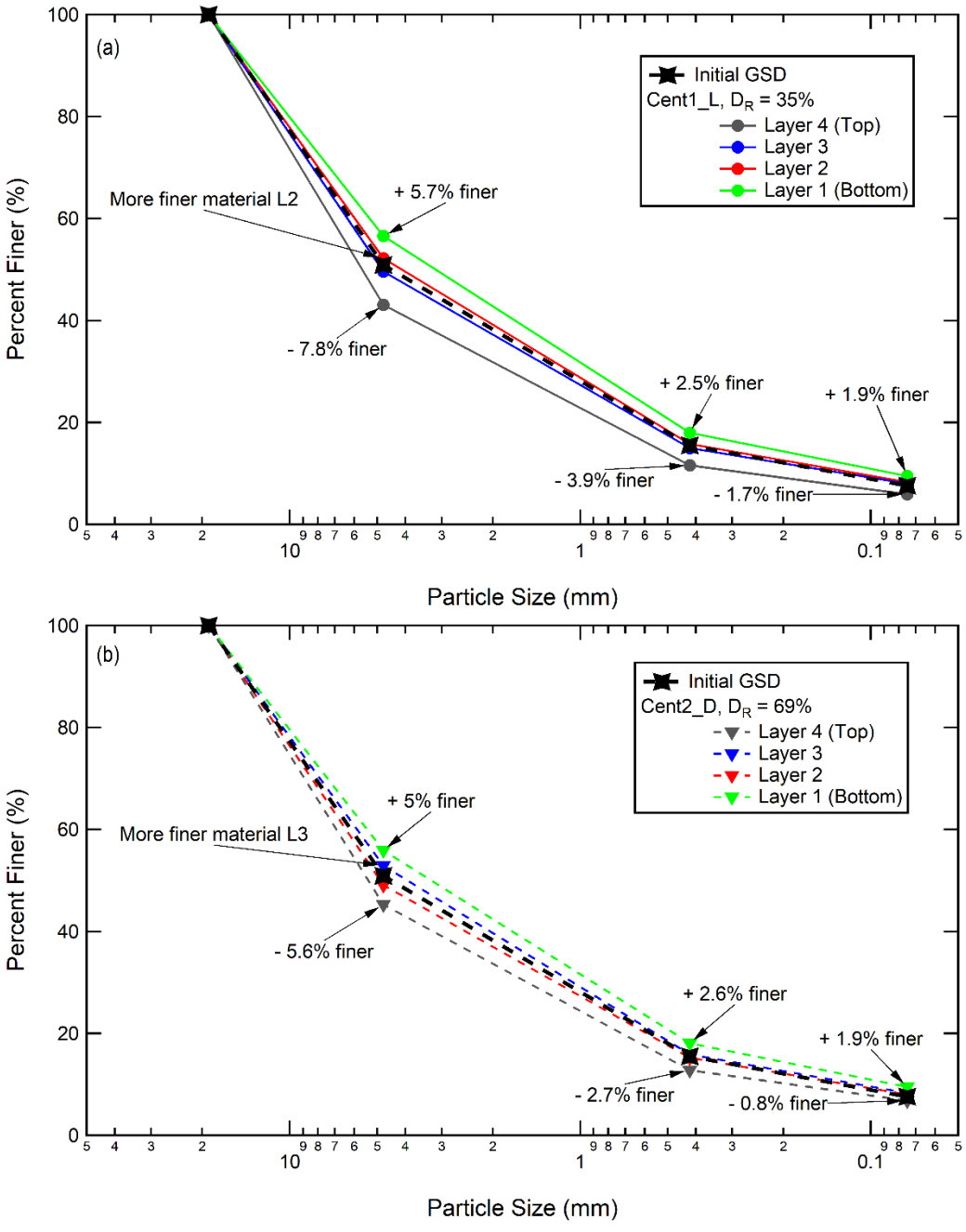

Figure 3.28 Initial and post-test percent finer for sieve No. 4, 40, and 200 in: (a) Cent1_L, and (b) Cent2_D.

3.7 Comparison of CTX and Centrifuge Model Results

There are many differences between element and physical model testing. Some such differences include stress condition, drainage condition, loading condition, and difficulty of performance. Firstly, in the triaxial equipment, the soil element is subjected to isotropic confinement. In other words, the soil experiences the same stress all around the sample. Comparatively, soil in a centrifuge model experiences geostatic stress, meaning stress that increases with depth. Therefore, with an array of instrumentation along the profile of the model, soil response at different vertical effective pressures can be assessed. Additionally, the centrifuge tests in this study included an assumed uniformly distributed surcharge load due to the lead shot used to increase confinement within the soil model. There is uncertainty in this assumption as the load most likely dissipated with depth and concentrated in the upper layers of the soil model. Even with this surcharge load, the confinement of triaxial tests (400 kPa) was greater than the centrifuge models (~ 140 kPa at the middle of the model). This difference in stress condition and confinement must be taken into consideration when comparing the triaxial and centrifuge data.

Secondly, cyclic triaxial element testing assumes ideal conditions as the test can only be performed completely drained or undrained. However, in centrifuge modeling, the soil is under a partial drainage condition due to the ability for pore pressures to dissipate at the surface of the model. Previous research has been done to provide adjustments to the Cyclic Resistance Ratio (CRR) due to these partial drainage effects in centrifuge tests of saturated sand (Darby et al., 2019). In general, they found that the adjustments made to the CRR values produced by centrifuge models decreased by 0 – 63

% for contractive volumetric strain and increased 0 – 36 % for dilative volumetric strain. These adjustments to centrifuge data resulted in better agreement with established correlations based on case histories. Therefore, it is clear that a CRR produced by partial drainage conditions in a contractive centrifuge model is less conservative in comparison to purely undrained conditions in element tests.

Lastly, in triaxial element testing, the sample undergoes vertical loading, compared to horizontal loading from a shake table in a centrifuge model. This is referred to as axial loading in the triaxial test and shear loading in the centrifuge model. Axial loading in the triaxial test does not apply a continuous or smooth rotation of the principal stresses. Additionally, the lateral displacement as the sample undergoes cyclic loading is neglected. Therefore, as vertical deformations are measured, calculations of axial strain can be made. In comparison, the lateral displacement in the centrifuge model results in measurements of shear strain. Shear strain is preferred because it is a direct result of shear stress applied to the soil. Earthquakes apply shear stress to soil in the field. In geotechnical engineering, shear stress is used to assess the shear strength of soil. Therefore, the axial strain produced in triaxial testing often correlates with the shear strain with uncertainty.

Although triaxial element testing does not fully represent field conditions, it is a simple method to assess the cyclic strength of soil. Centrifuge modeling requires a much larger volume of soil compared to the typical triaxial sample. This larger volume of soil is advantageous to the representation of field conditions but causes a more complicated test procedure. Sensor implementation during model construction takes time and requires detailed procedures for pre- and post-test measurements. The array of sensors enables a

more accurate and precise analysis however this requires more time and advanced data analysis skills. In comparison, triaxial test preparation and analysis is less labor intensive and can be completed more quickly. Therefore, in practice, triaxial testing is often the laboratory method of choice for dynamic evaluation. However, centrifuge modeling tests are valuable for research and critical geotechnical projects. It is of interest to then compare these results to those more representative of true field conditions. In the remainder of the section, the results of the cyclic triaxial element tests and the centrifuge models are compared.

In this study, a correlation between pore water pressure and volumetric strain was determined by undrained and drained cyclic triaxial tests. The methodology involved linking the two parameters through cyclic axial strain. Results of (ε_c, R_u) from undrained tests and (ε_c, ε_v) from drained tests were correlated to produce a relationship of (ε_v, R_u). Refer to Chapter 2 for further detail. Triaxial samples were subjected to an isotropic confinement of 400 kPa. A typical K_0 value of 0.5 was assumed to relate the effective stress simulated in the triaxial chamber to the field condition, increasing it by a magnitude of 1.5. This suggests that the field related effective stress applied to the triaxial samples is 600 kPa. This is important to note when comparing with the centrifuge models undergoing a vertical effective stress of ~ 140 kPa at the middle of the model. The relationships between excess pore water pressure and volumetric strain observed in cyclic triaxial tests are compared to the results from centrifuge tests in Figure 3.29. The data representative of centrifuge modeling corresponds to the average R_u and average volumetric strain from each cycle number for the Entire Soil Model. Therefore, the volumetric strain represents the volume change of the entire soil model, and the R_u was

obtained from an average of layers 2 and 3. It is clear that results between the two types of tests do not match which is anticipated because there are major differences between the two test methods. In general, the triaxial test resulted in a much greater pore pressure response compared to the centrifuge model. This is to be expected due to the partial drainage condition in the centrifuge model. Due to the ideal undrained condition in the cyclic triaxial equipment, there is a high buildup of pore water pressure at low volumetric strain. The triaxial correlation in Figure 3.29 at low strains is outside of the dataset produced by the element tests and is therefore an estimation. Consequently, the actual behavior at low volumetric strains is unknown. It is important to note that the volumetric strain occurred almost immediately (or at a very low magnitude of R_u) in the centrifuge model. Cent2_D reaches about 0.2 % volumetric strain before R_u reaches 0.01. Therefore, the centrifuge model resulted in larger volumetric strains for a lower R_u compared to the CTX element tests. This response is logical due to the partial drainage condition. It is possible that the partial drainage condition allows more volumetric strain during shaking due to the buildup and dissipation of excess pore water pressures. Excess pore water pressures in soil causes a redistribution of soil particles. Therefore, this redistribution in the partial drainage condition possibly aids in the ability of the soil to compact. This implies that in the field condition, it is possible to expect more volumetric strain or settlement at lower values of R_u than predicted by CTX testing.

As displayed, the medium dense and dense triaxial tests exhibit a similar behavior in the relationship of excess pore water pressure with increasing volumetric strain until about 0.0005% volumetric strain. Past this point, greater R_u is observed for the dense soil compared to the medium dense at a given volumetric strain. This general trend occurred

in the centrifuge model as well, but at a much greater value in volumetric strain. Until a volumetric strain of 1.3%, the loose centrifuge model had higher R_u for a given volumetric strain compared to the dense. However, past volumetric strain 1.3%, the dense centrifuge model had a greater excess pore pressure response compared to the loose. This behavior is similar to that observed in the triaxial and suggests that at larger volumetric strains, it is possible to observe more pore water pressure for soil in the dense condition. It is important to note that the relative density of the dense triaxial test is very dense (D_R ~100%) compared to just dense (D_R ~ 69%) in the centrifuge model. Additionally, triaxial tests had medium dense samples (D_R ~53%) while Cent1_L was in a loose condition (D_R ~35%).

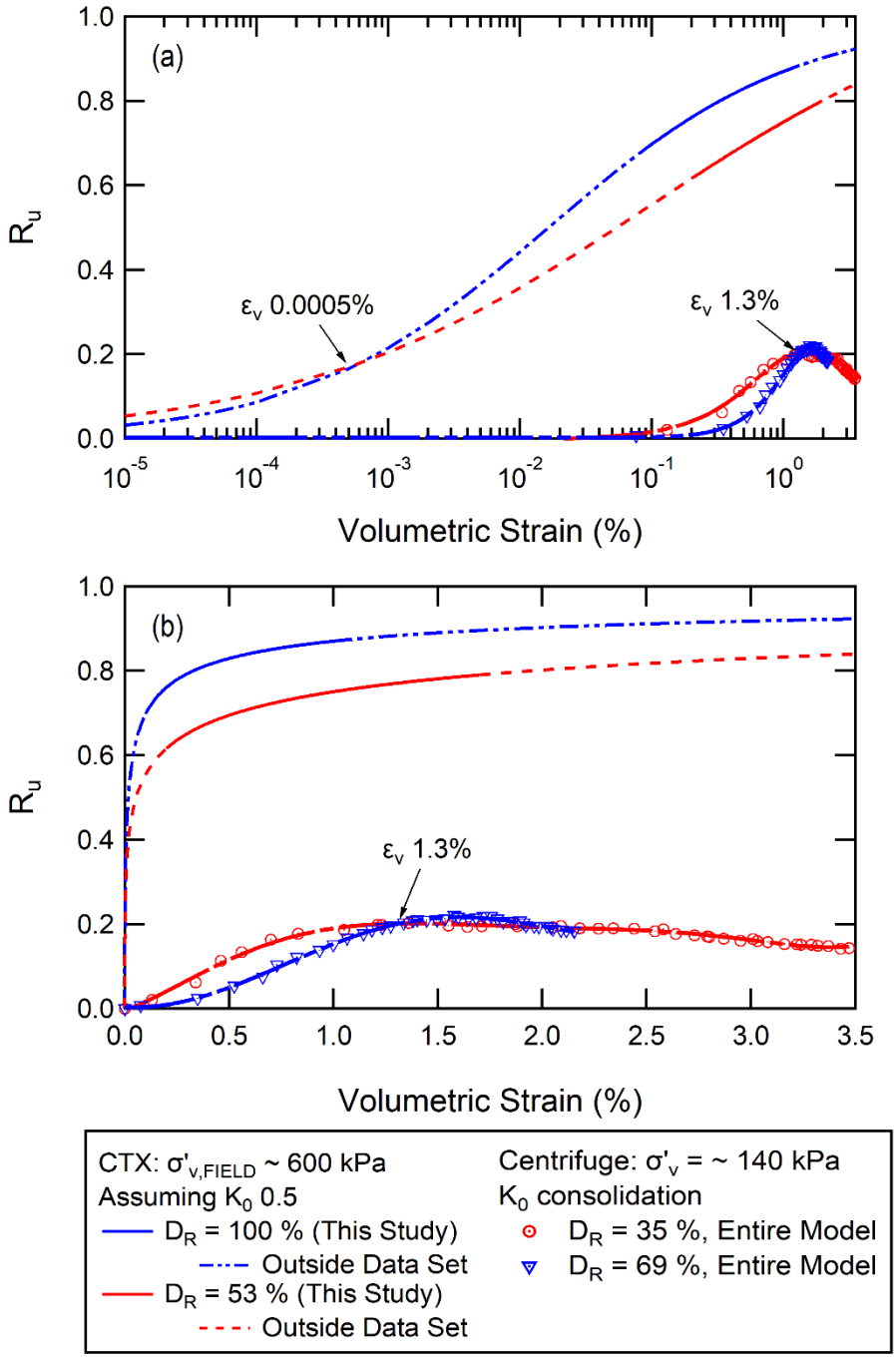

Figure 3.29 Comparison of volumetric strain and pore pressure relationship of CTX and centrifuge testing in: (a) semi-log scale, and (b) linear scale.

Figure 3.30 displays the buildup of R_u with increasing cyclic loading for CTX tests and centrifuge models. The centrifuge average CSR considering all soil layers is 0.41 and 0.37 in Cent2_D and Cent1_L, respectively. Figure 3.30 (a) displays a contour of CSR values for medium dense triaxial samples and both loose and dense centrifuge models. The very dense triaxial samples and dense centrifuge model are displayed in Figure 3.30 (b). In general, although the R_u developed in the CTX is a higher value, the R_u buildup with number of cycle follows the same trend in the centrifuge test. The loose models have a higher rate of excess pore pressure buildup that has an earlier peak. The two centrifuge models have similar R_u responses as shown in Figure 3.30 (a). In comparison, the triaxial tests have very different responses for DU and MDU samples subjected to the same CSR. This implies that relative density had a greater impact on the relationship of R_u with number of cycle in the triaxial tests compared to the centrifuge models. In addition, the excess pore water pressure results in the triaxial tests are conservative in comparison to the centrifuge models. This is displayed clearly as the triaxial tests subjected to less CSR compared to the centrifuge models still resulted in greater R_u at a given number of cycle.

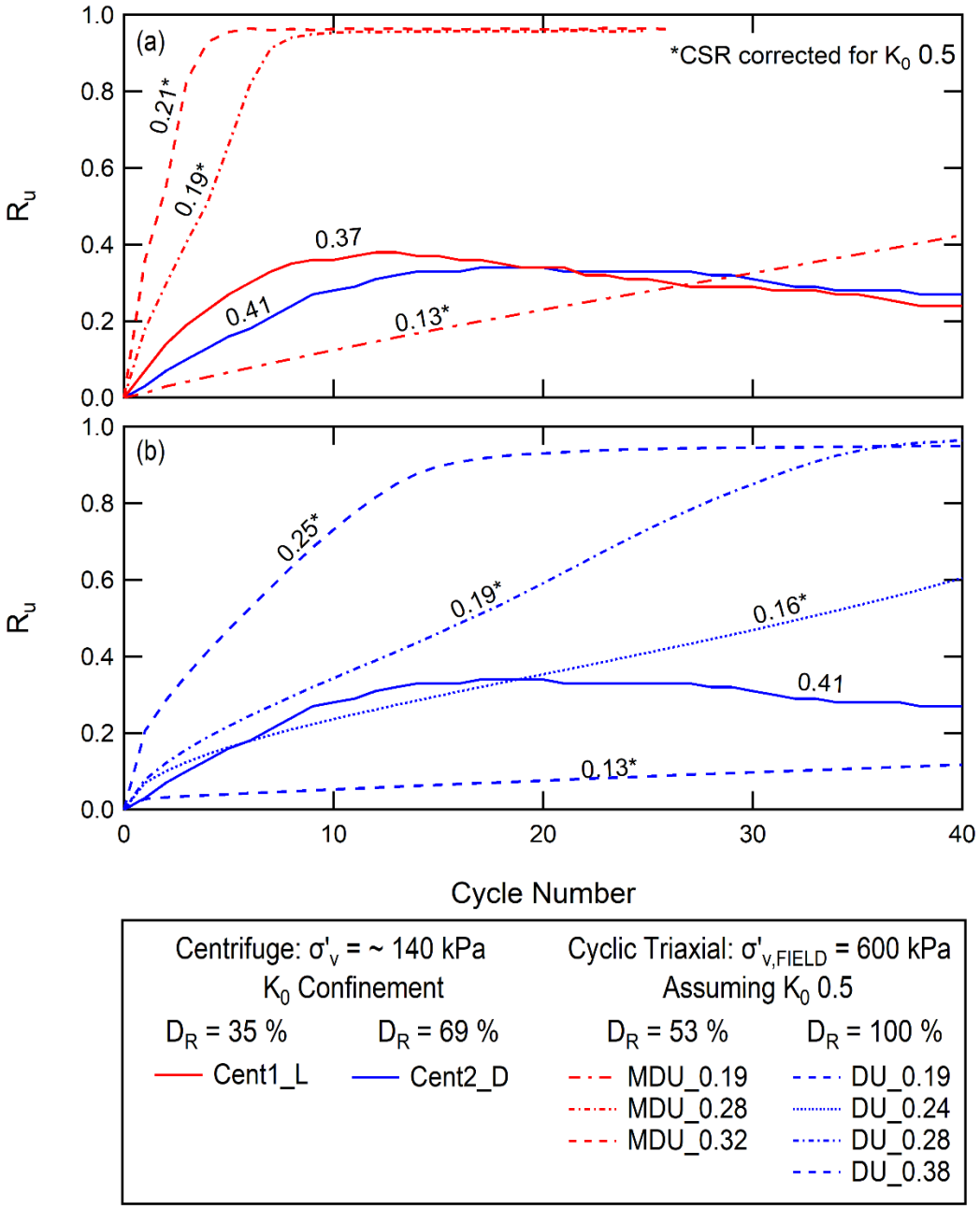

Figure 3.30 Comparison of pore water pressure buildup with cyclic loading of centrifuge and CTX tests with relative densities of: (a) loose to dense, and (b) dense to very dense.

CHAPTER 4

SUMMARY AND CONCLUSIONS

4.1 Introduction

This chapter includes the summary and conclusions of the triaxial element tests and centrifuge models. The results of this study aim to provide a better understanding of the dynamic behavior of gravelly soil for different drainage conditions. Findings of the study are described and thoughts of future work to further the understanding of gravelly soil are provided.

4.2 Cyclic Behaviors in Cyclic Triaxial Tests

The cyclic triaxial testing program in this study included undrained and drained stress-controlled tests for both dense (i.e., D_R = 100 %) and medium dense (i.e., D_R 53 %) conditions. Samples were subjected to isotropic confinement ranging from 350 to 400 kPa and CSR values from 0.19 to 0.38. Undrained tests were used to assess liquefaction characteristics (i.e. pore pressure generation model, CRR) while drained tests were used to estimate cyclic induced volumetric strain. A relationship between volumetric strain and pore water pressure was defined by using axial strain to correlate the two idealized drainage conditions.

For the undrained condition, liquefaction was achieved for both dense and medium dense samples. Dense samples of undrained triaxial element tests were able to sustain load for up to 471 more cycles compared to medium dense samples as R_u

increased. Once R_u increased greater than 0.8, the dense samples exhibited a greater dilation response within each cycle as the R_u was able to decrease nearly twice as much as the medium dense samples during stress reversal. Medium dense samples reached liquefaction at fewer cycles of loading compared to dense samples. However, the rate in the normalized excess pore pressure generation response of dense soils at early cycles of loading ($N/N_L \leq 0.4$) was greater (by no more than 0.1) compared to medium dense samples. This trend was found to decrease for increasing CSR. Axial strain accumulated in extension for all samples of undrained triaxial tests. This is likely due to a combination of high confinement and density.

For the drained condition, an increase in CSR resulted in higher volumetric strain at the end of cyclic loading for both density conditions. The effect of CSR on volume change was greater for medium dense samples compared to dense samples. An increase in CSR from 0.19 to 0.28 resulted in a subsequent increase of volumetric strain of 1.2% for medium dense samples compared to just 0.12% in dense samples. The medium dense samples demonstrated a greater exponential increase in volumetric strain for the CSR larger than 0.25 in comparison to the dense samples. In other words, when the applied CSR was higher than about 0.25, a much greater volume change for the medium dense samples was observed than the dense samples. Axial strain was observed to accumulate in compression with increasing cycles of loading. A correlation represented by an exponential relationship was defined for induced volumetric strain and cyclic axial strain. The impact of density on the relationship of volumetric strain with increasing cyclic axial strain was greater for cyclic axial strain at or above approximately 0.25 %. For axial strains smaller than this, the volumetric strain - cyclic axial strain response for dense and

medium dense samples were very similar. It was found that specimen size did not have a significant impact as drained triaxial tests of 6-inch and 4-inch sample diameter resulted in similar volumetric strain. This implies that the influence of larger particle size (i.e. > 1 inch) of about 6% by weight is minimal, therefore the 4-inch sample can be used. Due to the rarity of large triaxial equipment, this finding could aid in the efforts to expand the experimental study of the dynamic behavior of gravelly soil.

Results of excess pore water pressure and volumetric strain from the undrained and drained conditions were correlated using a strain-based method. The defined correlation suggests that at volumetric strains greater than ~ 0.0005 %, the rate of pore water pressure with increasing volumetric strain develops faster for dense soil compared to the medium dense soil. Pore pressure increases more in the dense sample to obtain the same volumetric strain as the medium dense sample. In other words, at a known pore water pressure, more volumetric strain % can be expected from a medium dense soil condition than a dense soil condition.

4.3 Cyclic Behaviors in Centrifuge Models

Two centrifuge models aimed to simulate an approximate 6m soil profile subjected to ~140 kPa vertical effective stress (at the middle of the model) under the partial drainage condition. A surcharge load was applied to reach desired higher confinement. Each model was constructed in 4 layers, each layer included two pore pressure transducers and two accelerometers. The surfaces of each layer were scratched during model construction to ensure interlocking and a uniform soil profile. The sensors arrays within the 4 layers enabled assessment of dynamic response for vertical effective stresses 117 kPa, 132 kPa, 147 kPa, and 161 kPa. Models had post-consolidation relative

density conditions of loose (i.e., 35%, Cent1_L) and dense (i.e., 69%, Cent2_D) and were subjected to two events of low (i.e., 0.015g) and high (i.e., 0.4g) shaking amplitude. The low amplitude shaking event was applied first for the purpose of assessing the dynamic response to a non-destructive dynamic load. During the 0.015g event, no volume change or excess pore water pressure occurred in either model. Whereas, for the 0.4g dynamic load, the volume change was immediate and occurred simultaneously with shaking. As pore pressures dissipated following cyclic loading, no further volume change was observed. Additionally, liquefaction did not occur for either density condition during shaking, as the maximum R_u observed was 0.38 and 0.34 in the loose and dense models, respectively. Observations of shear modulus and damping response suggest that gravelly soil has the ability to gain strength during cyclic loading.

The impact of relative density on the dynamic response of the material to the 0.4g event was assessed and is summarized as follows. In general, greater volumetric strain and pore water pressure occurred in the loose model. However, at the end of shaking, the dense model had higher excess pore pressure and therefore slower dissipation ability compared to the loose. The CSR – shear strain response of both models was similar, but slightly greater shear strain occurred in the loose model. Values of CSR ranged from 0.39 to 0.35 in Cent1_L and 0.44 to 0.39 in Cent2_D. Cyclic shear strains ranged 1.2% - 1.8% and 1.0% - 1.5% in the loose and dense model, respectively. Damping decreased with increasing cycles of loading for both models. The highest damping response was observed in the loose model, ranging 54% to 148% compared to 41% to 98% in the dense model. Additionally, Cent1_L had a greater reduction in damping from the start to the end of shaking. The dense model had a higher shear modulus response ranging from 1121

kPa to 2746 kPa compared to 681 kPa to 1811 kPa in the loose. For both models, an initial decrease in shear modulus was observed followed by an increasing trend for the remainder of shaking. However, at the end of shaking, stiffness ultimately decreased in Cent2_D. In comparison, at the end of shaking in Cent1_L, there was an ultimate gain in stiffness. This is likely due to the greater settlement observed in the loose model during shaking.

The effect of confinement on the cyclic response for the material was evaluated. The bottom half of Cent1_L and Cent2_D decreased in relative density post-consolidation. This dilative response in the lower half was also observed during the initial loading cycles of the 0.4g shaking amplitude event. In general, as confinement decreased, as did the observed cyclic shear strain. This impact of confinement on cyclic shear strain was greater for the loose model compared to the dense. For both relative densities, the highest cyclic shear strain occurred in the layer subjected to the highest confinement. Within this layer, the cyclic shear strain had an increasing trend with the number of cycles for the duration of shaking. For all other layers, the cyclic shear strain generally increased with the number of cycles as excess pore pressure developed and decreased as it dissipated. The damping response was highest in the layer subjected to the lowest confinement. In comparison, the shear modulus response was highest in the layer subjected to the greatest confinement. Low confinement was observed to greatly impact the shear modulus of gravelly soil as both models had a much lower shear modulus response in the shallowest layer. For a 15 kPa change in vertical effective stress from 132 kPa to 117 kPa, Cent1_L had a decrease in shear modulus that was nearly twice as much compared to the differences at greater confinements. Comparatively, Cent2_D had a

decrease in shear modulus three times as great for the shallowest confinement. As previously discussed, a loss in stiffness was observed in Cent2_D at the end of shaking while Cent1_L had a gain in stiffness. As confinement increased, there was a greater magnitude of loss in stiffness in Cent2_D and a lesser magnitude of stiffness gain in Cent1_L.

The drainage condition in the upper and lower halves of the centrifuge models were observed to be different and had influenced the excess pore pressure – volumetric strain response. Due to boundary conditions, the upper half of the model behaved more similarly to the partial drainage condition while the lower half behaved closely to a near-perfect undrained condition. Dilation and a transient pore water pressure response was observed in the bottom half in the initial cycles of loading. Following dilation, the bottom half contracted and a greater rate in excess pore water pressure with increasing volumetric strain was observed. Additionally, the excess pore water peaked at a volumetric strain about 1% less in the lower half of the model compared to the upper half which suggests upward flow. No dilation was observed in the top half of the model. In addition, a slower rate in increasing excess pore pressures with volumetric strain was observed in the top half. This is likely due to the partial drainage condition in which large increases in volumetric strain occurred simultaneously with shaking as pore pressure freely dissipated at the surface. The maximum excess pore water pressure was observed in the lower half of both models. In contrast, the upper half of the model had greater settlement. Results suggest that the relationship of excess pore water pressure with increasing volumetric strain is primarily impacted by drainage condition opposed to confinement and relative density.

The two shaking events of low (i.e., Shake Event 1 – 0.015g) and high (i.e., Shake Event 2 – 0.4g) amplitude allowed analysis of the behavior of gravelly soil subjected to a non-destructive dynamic event. No excess pore water pressure was observed in either model during 0.015g shaking, as R_u values were no greater than 0.003. Additionally, no volume change occurred due to this low shaking amplitude. For Shake Event 1, both models had slight amplifications of the base amplitude observed at the shallowest layer (i.e., increase of 0.01g and 0.003g in dense and loose, respectively). In comparison, de-amplification occurred for Shake Event 2 (i.e., decrease of 0.05g and 0.08g in dense and loose, respectively). This suggests that the loose model had greater damping capability compared to the dense. This is supported by the higher damping response in Cent1_L as previously mentioned. Considering both models, cyclic shear strains ranged 0.04 - 0.12% and 1.0 – 1.8% for 0.015g and 0.4g shaking amplitudes, respectively. This suggests that the threshold cyclic shear strain for this material is at least 0.12% since no excess pore pressure or volume change occurred in response to Shake Event 1. The values of shear modulus in response to 0.015g shaking vary more with confinement compared to that of 0.4g shaking. In contrast, values of damping vary more with confinement when subjected to 0.4g compared to lower amplitude 0.015g. This suggests that the impact of confinement on shear modulus is greater for lower amplitudes of dynamic loading. In comparison, the impact of confinement on damping is possibly greater for higher shaking amplitudes. This finding could also be correspondent to the low cyclic shear strains produced at low amplitudes compared to higher cyclic shear strain for higher shaking amplitudes.

4.4 Summary of Comparisons

The effects of drainage condition and relative density were evaluated through cyclic triaxial testing and centrifuge modeling. The relationship of volumetric strain and excess pore pressure correlated by triaxial results did not match results from the centrifuge tests due to differences in drainage condition, confinement, and loading.

The triaxial condition is considered an idealized condition that may not realistically represent the field condition. This applies particularly to gravelly soils as they are characteristic of high permeability and are often used as a drainage material in the geotechnical engineering field. The centrifuge models simulated a partial drainage condition in the top half of the model and near-perfect undrained condition in the bottom half of the model. This resulted in two different observations in the relationship of R_u with increasing volumetric strain in the top and bottom halves. The excess pore water pressure result in the triaxial tests were conservative compared to the centrifuge due to the truly undrained condition. Additionally, dilative volumetric strain and positive pore water pressures were observed in the bottom half of the centrifuge models subjected to a near-perfect undrained condition. This dilative behavior was not observed in the perfectly drained triaxial samples.

Confinement applied to the triaxial element tests and physical models was different due to a capacity limitation of the shake table in the centrifuge. Triaxial samples were subjected to isotropic confinement of 400 kPa. Assuming a K_0 value of 0.5, this corresponds to roughly a vertical effective stress of 600 kPa in the field. Centrifuge models were subjected to 140 kPa effective vertical stress at the middle of the model. Additionally, centrifuge models were subjected to cyclic shear stress while triaxial

samples were subjected to cyclic axial stress. Samples in the triaxial experience a continuous reversal of principal stresses. Regardless of these differences, comparison of triaxial and centrifuge modeling results produced in this study provided a better understanding of the effects of drainage condition on gravelly soil and emphasized the importance of physical model tests.

Results from cyclic triaxial tests showed that more volumetric strain was required in medium dense samples to obtain the same amount of R_u in dense samples. In other words, for the same magnitude of volumetric strain, there was a greater positive excess pore water response in dense soil. Therefore, there was a faster rate of excess pore pressure development with increasing volumetric strain for dense samples. For the partial drainage condition in centrifuge models, there was faster rate in R_u with increasing volumetric strain for the loose model compared to the dense. However, at 1.3% volumetric strain, the R_u observed in the dense and loose model was the same. For volumetric strains past this point, the dense model resulted in higher R_u compared to the loose. Ultimately however, there was greater contractive volumetric strain observed in the loose model compared to the dense. This was also observed in the triaxial tests, as medium dense samples obtained greater volumetric strains compared to dense samples. However, the magnitude of these volumetric strains was not as large as those observed in centrifuge models. This is possibly due to the high lateral stress applied to the triaxial samples subjected to isotropic confinement.

Although the relationship of R_u with increasing volumetric strain for centrifuge models and triaxial tests in this study followed similar general trends, the magnitude of R_u produced in triaxial tests was much greater than that produced in centrifuge models.

This is primarily due to the partial drainage condition in the centrifuge model. This suggests that for porous material such as gravelly soil, greater volumetric strains could result at lower excess pore pressures in the field than estimated by triaxial tests. This observation emphasizes the importance of field observations and large-scale physical model tests.

4.5 Recommendations for Future Research

For future research, strain-controlled cyclic triaxial testing is recommended opposed to load-controlled to better approximate volumetric and pore water pressure at low strains. However, such is not a routine standardized test. There may be complications associated with drained strain-controlled cyclic triaxial tests which requires further research to develop the technique to perform the test. Further exploration on the effect of sample size is encouraged to broaden the capability of research for gravelly soils as it eliminates the need for large scale equipment that is not readily available. Comparison of laboratory element tests with centrifuge models at a wide range of stains for the same level of confinement would provide better comparison between both tests. This would better isolate the impact of partial drainage conditions which are more realistic to what is found in the field and therefore must be better understood when performing simplified element testing.

REFERENCES

ASTM D5311/ D5311M-13. (2013). Standard test method for load controlled cyclic triaxial strength of soil. ASTM, Standard.

Baize, S., Amoroso, S., Belić, N., Benedetti, L., Boncio, P., Budić, M., ... & Ricci, T. (2022). Environmental effects and seismogenic source characterization of the December 2020 earthquake sequence near Petrinja, Croatia. *Geophysical Journal International*, *230*(2), 1394-1418.

Banzibaganye, G., & Vrettos, C. (2022). Sand–tyre chips mixtures in undrained and drained cyclic triaxial tests. *Proceedings of the Institution of Civil Engineers-Ground Improvement*, *175*(1), 23-33.

Boulanger, R. W., & Idriss, I. M. (2004). *Evaluating the potential for liquefaction or cyclic failure of silts and clays* (p. 131). Davis, CA: Center for Geotechnical Modeling.

Cao, Z., Youd, T. L., & Yuan, X. (2011). Gravelly soils that liquefied during 2008 Wenchuan, China earthquake, Ms= 8.0. *Soil Dynamics and Earthquake Engineering*, *31*(8), 1132-1143.

Chen, G., Zhao, D., Chen, W., & Juang, C. H. (2019). Excess pore-water pressure generation in cyclic undrained testing. *Journal of Geotechnical and Geoenvironmental Engineering*, *145*(7), 04019022.

Darby, K. M., Boulanger, R. W., & DeJong, J. T. (2019). Effect of partial drainage on cyclic strengths of saturated sands in dynamic centrifuge tests. *Journal of Geotechnical and Geoenvironmental Engineering*, *145*(11), 04019089.

El Takch, A., Sadrekarimi, A., & El Naggar, H. (2016). Cyclic resistance and liquefaction behavior of silt and sandy silt soils. *Soil Dynamics and Earthquake Engineering*, *83*, 98-109.

Evans, M. D., & Rollins, K. M. (1999). Developments in gravelly soil liquefaction and dynamic behavior. *Physics and mechanics of soil liquefaction*, P. L. Lade and J. A. Yamamuro, eds., Balkema, Rotterdam, Netherlands, 91–102.

Ferdosi, B., James, M., & Aubertin, M. (2015). Effect of waste rock inclusions on the seismic stability of an upstream raised tailings impoundment: a numerical investigation. *Canadian Geotechnical Journal*, *52*(12), 1930-1944.

Flora, A., Lirer, S., & Silvestri, F. (2012). Undrained cyclic resistance of undisturbed gravelly soils. *Soil Dynamics and Earthquake Engineering*, *43*, 366-379.

Guoxing, C., Qi, W., Tian, S., Kai, Z., Enquan, Z., Lingyu, X., & Yanguo, Z. (2021). Cyclic behaviors of saturated sand-gravel mixtures under undrained cyclic triaxial loading. *Journal of Earthquake Engineering*, *25*(4), 756-789.

Hubler, J. F., Athanasopoulos-Zekkos, A., & Zekkos, D. (2023). Pore Pressure Generation of Gravelly Soils in Constant Volume Cyclic Simple Shear. *Journal of Geotechnical and Geoenvironmental Engineering*, 149(2), 04022130.

Ishihara, K., & Yoshimine, M. (1992). Evaluation of settlements in sand deposits following liquefaction during earthquakes. *Soils and Foundations*, 32(1), 173-188.

James, M., Aubertin, M., Bussière, B., Pednault, C., Pépin, N., & Limoges, M. (2017). A research project on the use of waste rock inclusions to improve the performance of tailings impoundments. *Proceedings of GeoOttawa*, 8.

Jiaer, W. U., Kammerer, A. M., Riemer, M. F., Seed, R. B., & Pestana, J. M. (2004, August). Laboratory study of liquefaction triggering criteria. In *13th World Conference on Earthquake Engineering, Vancouver, BC, Canada, Paper* (No. 2580).

Kaseng, F., Maldonado, E., & Rodriguez, C. (n.d.). Stability of a mine tailings dam considering dynamic liquefaction. *Journal of Critical Reviews*, *7*(15).

Kossoff, D., Dubbin, W. E., Alfredsson, M., Edwards, S. J., Macklin, M. G., & Hudson-Edwards, K. A. (2014). Mine tailings dams: characteristics, failure, environmental impacts, and remediation. *Applied Geochemistry*, 51, 229-245.

Naik, S. P., Kim, Y. S., Kim, T., & Su-Ho, J. (2019). Geological and structural control on localized ground effects within the Heunghae Basin during the Pohang Earthquake (MW 5.4, 15th November 2017), South Korea. *Geosciences*, *9*(4), 173.

Ni, M., Abdoun, T., Dobry, R., Zehtab, K., Marr, A., & El-Sekelly, W. (2020). Pore pressure and K σ evaluation at high overburden pressure under field drainage conditions. I: Centrifuge experiments. *Journal of Geotechnical and Geoenvironmental Engineering*, *146*(9), 04020088.

Pepin, N., Aubertin, M. and James, M. (2012). A seismic table investigation of the effect of inclusions on the cyclic behavior of tailings. *Canadian Geotechnical Journal 49* (4), pp. 416-426.

Polito, C. P., Green, R. A., & Lee, J. (2008). Pore pressure generation models for sands and silty soils subjected to cyclic loading. *Journal of Geotechnical and Geoenvironmental Engineering*, 134(10), 1490-1500.

Ruttithivaphanich, P. (2022). Cyclic Response and Liquidfaction Behavior of Gravelly Soils (Doctoral dissertation, University of South Carolina).

Ruttithivaphanich, P., & Sasanakul, I. (2022). Centrifuge modeling studies on effects of composition on liquefaction of mine waste rock. *Soil Dynamics and Earthquake Engineering*, *160*, 107378.

Ruttithivaphanich, P., & Sasanakul, I. (2023). Centrifuge Modeling of Fines Content Influence on Liquefaction Behaviors of Loose Gravelly Soils. *Journal of Geotechnical and Geoenvironmental Engineering*, *149*(3), 04023008.

Salvatore, N., Pizzi, A., Rollins, K. M., Pagliaroli, A., & Amoroso, S. (2022). Liquefaction assessment of gravelly soils: the role of in situ and laboratory geotechnical tests through the case study of the Sulmona basin (Central Italy). *Italian Journal of Geosciences*, *141*(2), 216-229.

Stamatopoulos, C. A., Balla, L. N., & Stamatopoulos, A. C. (2004, August). Earthquake-induced settlement as a result of densification, measured in laboratory tests. In Proc *13th World Conference on Earthquake Engineering*. Vancouver (pp. 1-15).

Tokimatsu, K., & Seed, H. B. (1987). Evaluation of settlements in sands due to earthquake shaking. *Journal of Geotechnical Engineering*, 113(8), 861-878.

Vucetic, M. (1994). Cyclic threshold shear strains in soils. *Journal of Geotechnical Engineering*, 120(12), 2208-2228.

Wichtmann, T., Niemunis, A. & Triantafyllidis, Th. (2005). Strain accumulation in sand due to cyclic loading: drained triaxial tests. *Soil Dynamics and Earthquake Engineering, 25, 967-979.*

Xu, D. S., Liu, H. B., Rui, R., & Gao, Y. (2019). Cyclic and postcyclic simple shear behavior of binary sand-gravel mixtures with various gravel contents. *Soil Dynamics and Earthquake Engineering*, *123*, 230-241.

Zeghal, M., & Elgamal, A. W. (1994). Analysis of site liquefaction using earthquake records. *Journal of Geotechnical Engineering*, *120*(6), 996-1017.

APPENDIX A

CENTRIFUGE LAB DATA

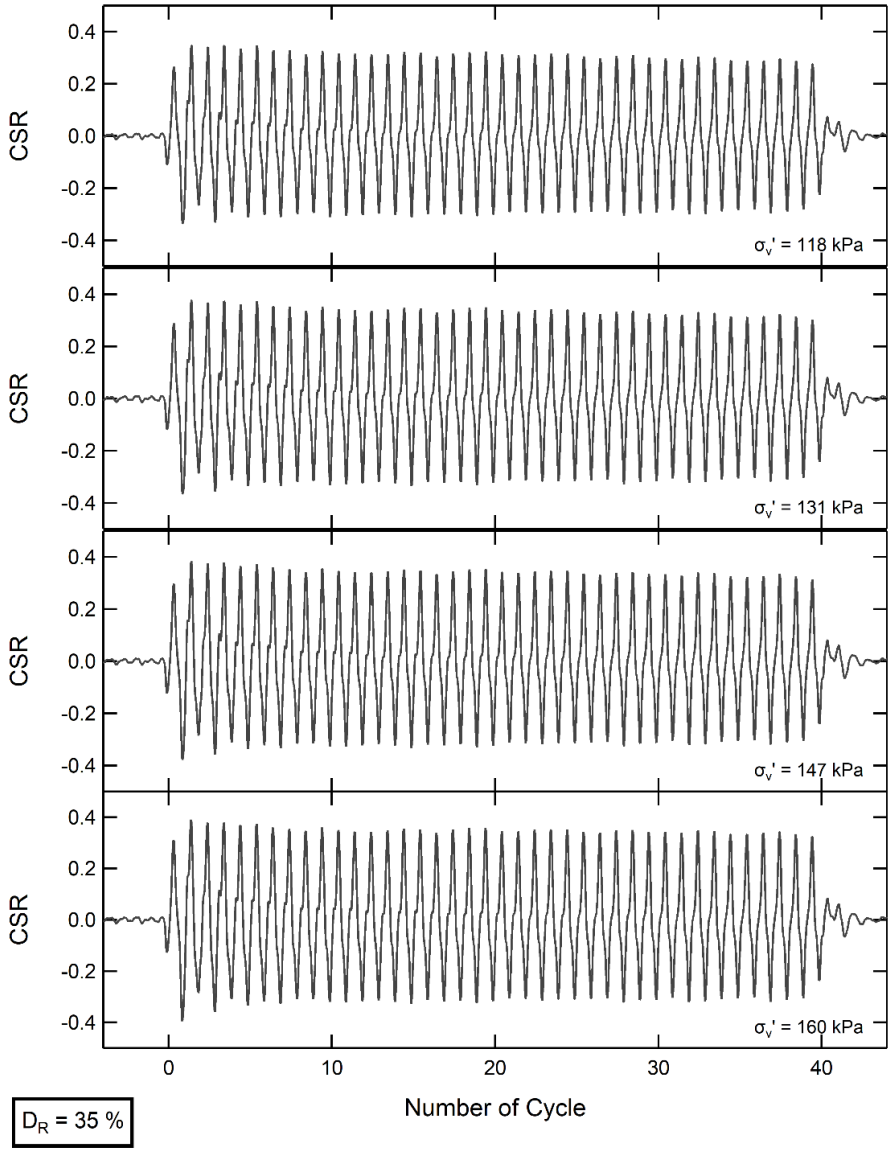

Figure A.1 Results of CSR with number of cycles for Cent1_L.

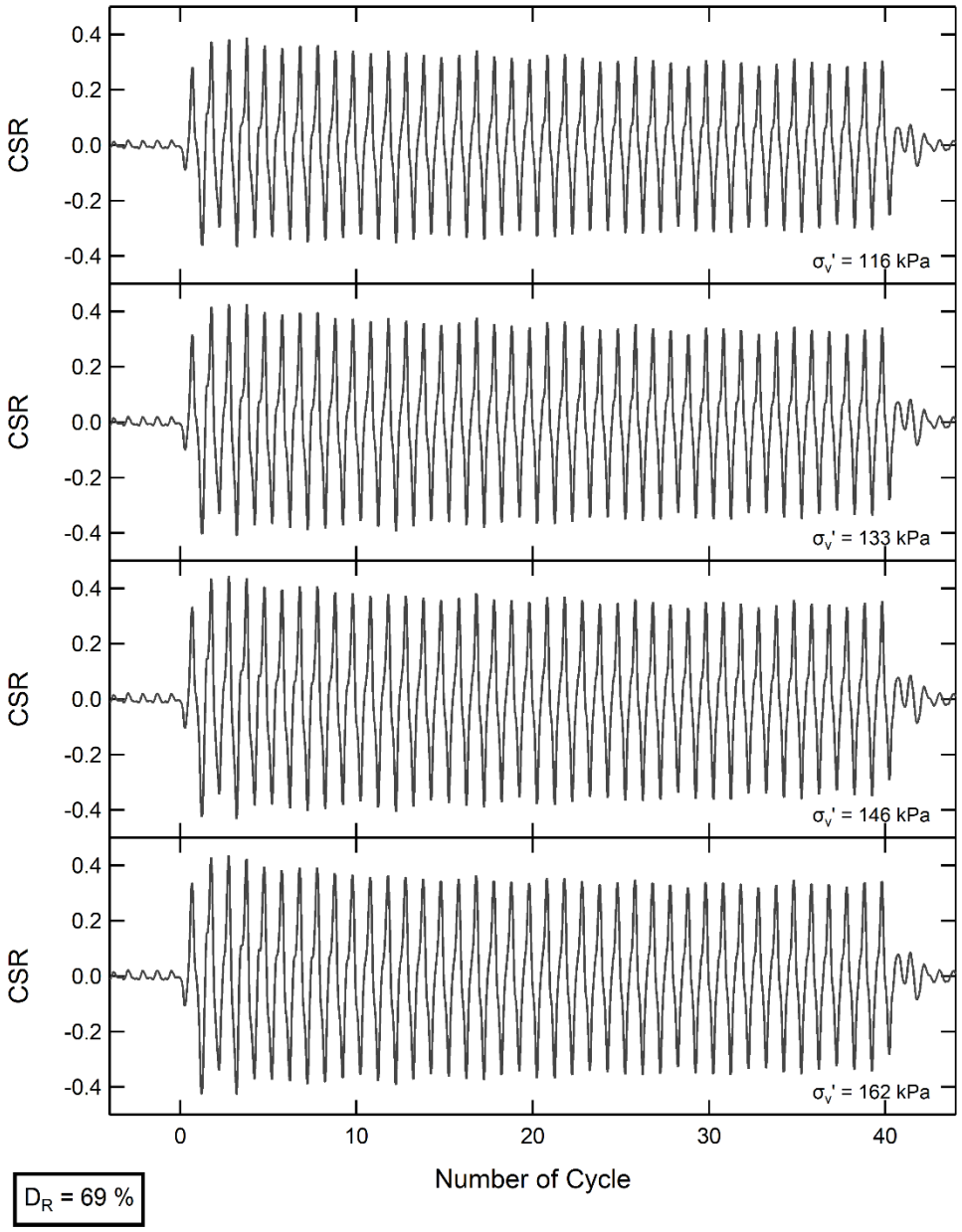

Figure A.2 Results of CSR with number of cycles for Cent2_D.

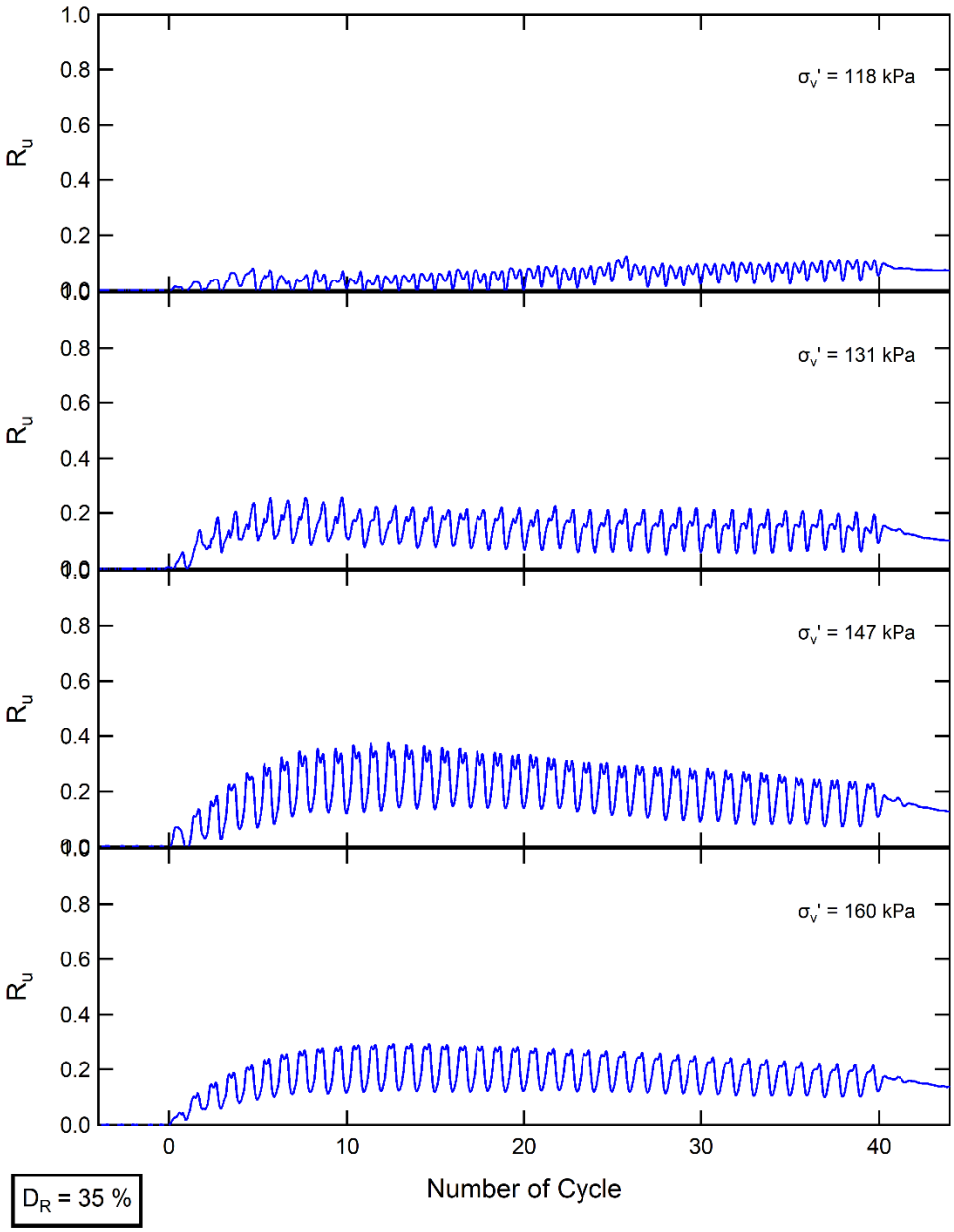

Figure A.3 Results of R_u with number of cycles for Cent1_L.

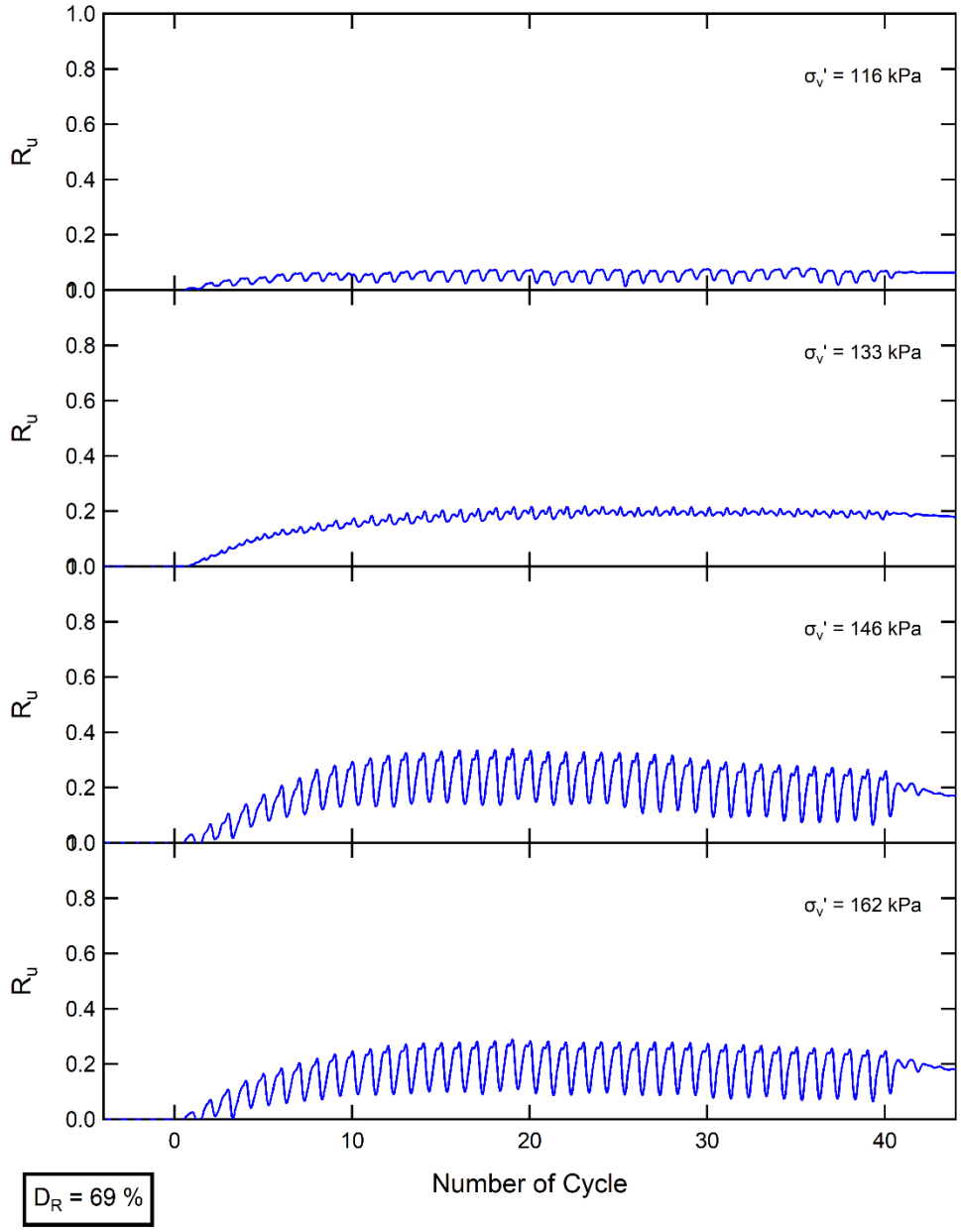

Figure A.4 Results of R_u with number of cycles for Cent2_D.

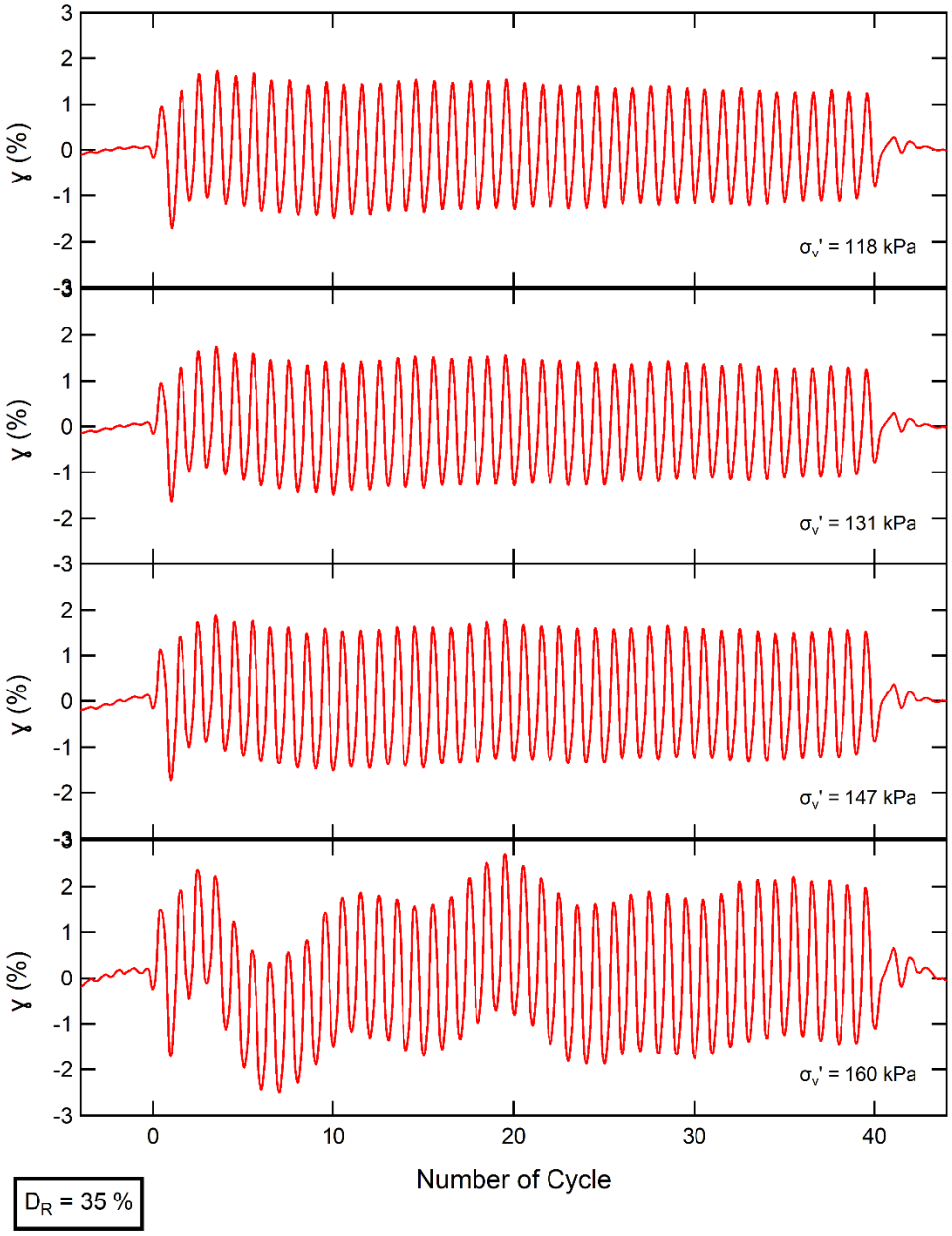

Figure A.5 Results of shear strain with number of cycles for Cent1_L.

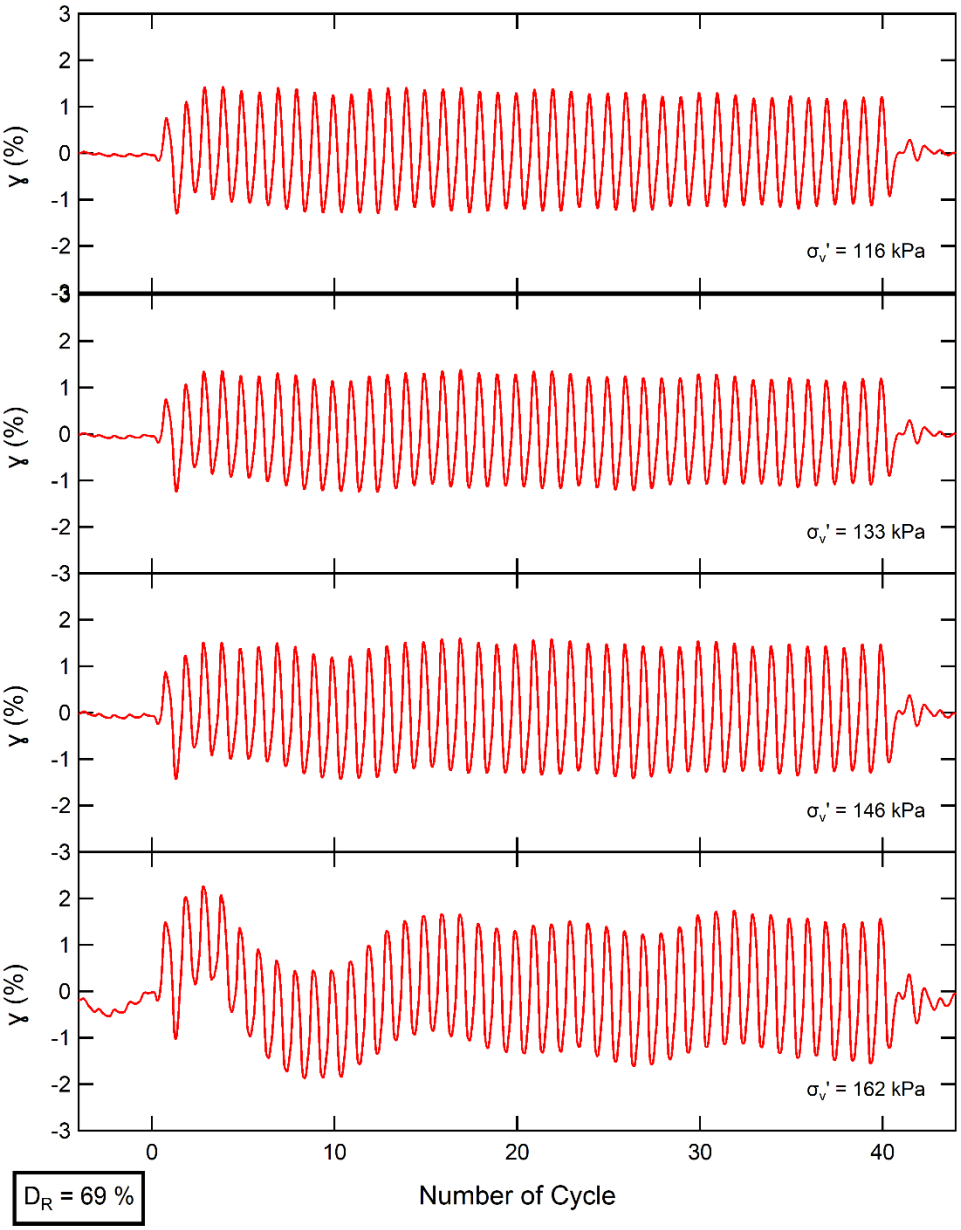

Figure A.6 Results of shear strain with number of cycles for Cent2_D.